The Optimized Mean-Trajectory Approximation of Vibrational Response Functions

A Dissertation

Presented to the Faculty of the Graduate School

of Cornell University

in Partial Fulfillment of the Requirements for the Degree of

Doctor of Philosophy

by

Mallory Renée Alemi

May 2015

The Optimized Mean-Trajectory Approximation of Vibrational Response Functions

Mallory Renée Alemi, Ph.D.

Cornell University 2015

Two-dimensional infrared (2D IR) spectroscopy probes complex vibrational couplings on a subpicosecond time scale. In the past two decades this method has been applied to a variety of benchmark and biologically relevant molecules, investigating structural dynamics, solvation, and population and coherence transfer. The fundamental quantity probed in such experiments is the third order vibrational response function. It is difficult to extract all of the structural and dynamical information encoded in the vibrational response function because many processes can contribute to the signal. In order to obtain maximal information from the experimental spectra, atomic level models of two-dimensional spectra are necessary. We have developed a semiclassical method for computing multidimensional vibrational spectra, the optimized mean-trajectory (OMT) approximation, that relies on the association of quantum mechanical eigenstates of the Hamiltonian with the action-angle variables of classical mechanics. This approximation is derived by developing a correspondence between double-sided Feynman diagrams, typically used to describe contributions to 2D IR spectra, with semiclassical OMT diagrams. The OMT is shown to well reproduce the vibrational response function for single[1] and multiple oscillator systems, without[2] and with[3] a dissipative bath, and also to describe energy transfer processes such as population and coherence transfer.[4]

Biographical Sketch

Mallory Alemi (formerly Mallory Gerace) attended University of Florida, where she attained a bachelor of science degree in Chemistry and a minor in Mathematics. In 2010 she enrolled as a Ph.D. student at Cornell University where she has done her thesis work under the advisement of Dr. Roger F. Loring.

to my loving husband Alex

and my parents for their unending support

Acknowledgements

Thank you to my adviser Roger F. Loring, for his help and advice.

This work was funded by the National Institutes of Health under Ruth L. Kirschstein National Research Service Award (2T32GM008267) from the National Institute of General Medical Sciences and by the National Science Foundation under CHE-1361484.

Portions of this thesis are reproduced in part with permission from:

M. Gerace and R. F. Loring. An Optimized Semiclassical Approximation for Vibrational Response Functions. *J. Chem. Phys.*, 138:124104, 2013. Copyright 2013 American Institute of Physics.

M. Gerace and R. F. Loring. Two-Dimensional Spectroscopy of Coupled Vibrations with the Optimized Mean-Trajectory Approximation. *J. Phys. Chem. B*, 117:15452-15461, 2013. Copyright 2013 American Chemical Society.

M. Alemi and R. F. Loring. Two-Dimensional Vibrational Spectroscopy of a Dissipative System with the Optimized Mean-Trajectory Approximation. *J. Phys. Chem. B*, Published online 2014. Copyright 2014 American Chemical Society.

M. Alemi and R. F. Loring. Vibrational Coherence and Energy Transfer in Two-Dimensional Spectra with the Optimized Mean-Trajectory Approximation. *J. Chem. Phys.*, 142:212417, 2015. Copyright 2015 American Institute of Physics.

Table of Contents

List of Figures

Chapter 1

Introduction

1.1 Two-dimensional Infrared Spectroscopy

Two-dimensional infrared spectroscopy[5–11] (2D IR) is a multidimensional generalization of Fourier transform infrared (FT IR) spectroscopy. 2D IR spectroscopy encompasses several experimental methods that probe molecular vibrations and their couplings through a series of infrared pulses. These methods attain greater resolution of spectral features than in FT IR by separating the spectra onto two frequency axes, making direct measurements of vibrational couplings, and therefore molecular structure, with femtosecond to picosecond time resolution. 2D IR spectroscopy therefore provides complementary information to other commonly used direct probes of molecular structure, such as 2D NMR spectroscopy,[12,13] which can be used to attain high spatial resolution structures but with a time resolution on the order of microseconds to milliseconds.

The first frequency-frequency 2D IR spectra were published in 1998 by Hamm, Lim and Hochstrasser.[14] In this work vibrational relaxation and dephasing of the amide I band of N-methylacetamide (NMA) and three well characterized small globular proteins were probed with pump-probe and hole burning experimental methods. Since these spectra were published 2D IR spectroscopy has been used to investigate many processes including: the dynamics of lipids,[15] proteins,[16–19] and liquid water,[20–22] and population relaxation[17] and coherence transfer.[23]

2D IR spectra can be congested and difficult to interpret as many distinct processes can contribute to the signal. To extract maximal information from these

spectra it is therefore necessary to have theoretical models to aid in the interpretation of experimental results. Furthermore, approximate methods are needed for all but the simplest systems because the vibrational Hamiltonians probed cannot be treated with exact quantum mechanics. Many approaches have been used to simulate 2D IR spectra.[23–31] A popular atomistic method involves separating the model into a 'system', treated with a high level of theory such as quantum mechanics, and a 'bath', treated with a lower level of theory such as classical mechanics. The state of the bath is then used to parametrize the state of the system.[29,32–34] This approach often relies on frequency mappings,[35–38] which relate a Hamiltonian of the system to the electrostatic potential or derivatives of this potential. Molecular dynamics (MD) simulations can then be used to generate parameters for a reduced quantum calculation.[39–41] One such approach is the numerical integration of the Schrödinger equation (NISE) method.[18,40,42] Another atomistic approach based on determining the reduced density matrix has been developed by solving the low-temperature corrected quantum Fokker Plank (LTC-QFP) equation. This method has been applied to small systems for zero waiting time.[43–45]

In contrast to these methods we develop a semiclassical approximation[46–54] with a uniform theoretical framework applied to all degrees of freedom. Our approach relies on the existence of action-angle variables[55] so that its application to multidimensional systems is limited to systems that are approximately quasiperiodic[56,57] on the timescales of interest. Other semiclassical approximations to the response function have been developed that rely on this formalism, including two semiclassical methods involving action-quantized classical trajectories developed by Cao et al.[58–61] The first of these methods removes divergences in the classical response function calculation by replacing the standard distribution function by a uniform probability distribution with a quantized 'uncertainty volume' of order

$\hbar^n$ for the n^{th} order response function.[58,59] The second method involves using a Weyl-Wigner-Moyal symbol calculus[62] approach to obtain higher order corrections to the classical response function.[60,61] While, our method relies on a similar theoretical framework it differs in both its derivation and its final form from these approximations to the response function. In Appendix C we use the Weyl-Wigner-Moyal symbol calculus approach as the starting point of an approximate response function calculation and compare the resulting expression to the optimized mean-trajectory (OMT) approximation, derived in Chapter 2, which is the central result of this thesis. A third semiclassical approach, the mean-trajectory (MT) method, was developed by Gruenbaum and Loring,[63–66] based on approximately evaluating the response function using the Herman-Kluk[52,67–70] time propagator in the coherent state basis. This method had success in computing the vibrational linear response function[63] and the vibrational echo signal[64–66] but had difficulties in reproducing quantum mechanical waiting time dynamics.[64] The MT approximation is similar to the OMT approximation, but differs in a few key respects that allows the OMT approximation to better describe the evolution of the response function for all time variables. The MT approximation is briefly reviewed and the OMT and MT methods are compared in Appendix B.

1.2 Vibrational Response Function

Two-dimensional infrared spectra are measured in the weak field limit, so that the fundamental observable can be treated as a perturbative correction to the macroscopic polarization, $P(t)$,[5,11] which is proportional to the expectation value of the transition dipole operator, $\hat{\mu}$. We can determine this quantity to a given perturbative order in the electric field by assuming the Hamiltonian can be written

as a part pertaining to the system, $\hat{H}_0$, and a part that describes the interaction of the system with the electric field, $\hat{W}$

$$\hat{H} = \hat{H}_0 + \hat{W}. \tag{1.1}$$

Within the interaction picture, the density operator's time evolution under the Hamiltonian in Eq. (1.1) is,

$$\frac{d\hat{\rho}_{\mathrm{I}}}{dt} = -\frac{i}{\hbar}\left[\hat{W}_{\mathrm{I}}, \hat{\rho}_{\mathrm{I}}\right] \tag{1.2}$$

In the interaction picture, $\hat{A}_{\mathrm{I}}(t) \equiv K_0^{\dagger}(t-t_0)\hat{A}K_0(t-t_0)$ with $K_0(t) \equiv e^{-i\hat{H}_0 t/\hbar}$. The solution can be obtained iteratively to a given order of interaction with the electric field,

$$\hat{\rho}_{\mathrm{I}}(t) = \hat{\rho}_{\mathrm{I}}^{(0)}(t_0) + \sum_{n=1}^{\infty}\left(-\frac{i}{\hbar}\right)^n \int_{t_0}^{t} \mathrm{d}\tau_n \int_{t_0}^{\tau_n} \mathrm{d}\tau_{n-1} \cdots \int_{t_0}^{\tau_2} \mathrm{d}\tau_1 \left[\hat{W}_{\mathrm{I}}(\tau_n), \left[\hat{W}_{\mathrm{I}}(\tau_{n-1}), \ldots \left[\hat{W}_{\mathrm{I}}(\tau_1), \hat{\rho}_{\mathrm{I}}(t_0)\right] \ldots\right]\right]. \tag{1.3}$$

We will treat the radiation-matter interaction classically within the dipole approximation as $\hat{W} = -\hat{\mu}E(t)$, with electric field, $E(t) = \mathcal{E}(t)\cos\left(-\mathbf{k}\cdot\mathbf{r} - \omega t + \phi\right)$, pulse envelope $\mathcal{E}(t)$, wavevector $\mathbf{k}$, frequency ω, and phase ϕ. Substituting this form for the interaction into Eq. (1.3) gives,

$$\hat{\rho}_{\mathrm{I}}(t) = \hat{\rho}_{\mathrm{I}}^{(0)}(t_0) + \sum_{n=1}^{\infty}\left(\frac{i}{\hbar}\right)^n \int_{t_0}^{t} \mathrm{d}\tau_n \int_{t_0}^{\tau_n} \mathrm{d}\tau_{n-1} \cdots \int_{t_0}^{\tau_2} \mathrm{d}\tau_1 E(\tau_n)E(\tau_{n-1})\cdots E(\tau_1) \left[\hat{\mu}_{\mathrm{I}}(\tau_n), \left[\hat{\mu}_{\mathrm{I}}(\tau_{n-1}), \ldots \left[\hat{\mu}_{\mathrm{I}}(\tau_1), \hat{\rho}_{\mathrm{I}}(t_0)\right] \ldots\right]\right]. \tag{1.4}$$

We can then change into the Schrödinger picture, assuming that $\hat{\rho}(t_0)$ is the equilibrium density operator and therefore does not evolve under the action of $\hat{H}_0$.

$$\hat{\rho}(t) = \hat{\rho}^{(0)}(t_0) + \sum_{n=1}^{\infty}\left(\frac{i}{\hbar}\right)^n \int_{t_0}^{t} \mathrm{d}\tau_n \int_{t_0}^{\tau_n} \mathrm{d}\tau_{n-1} \cdots \int_{t_0}^{\tau_2} \mathrm{d}\tau_1 E(\tau_n)E(\tau_{n-1})\cdots E(\tau_1) \hat{\mathcal{G}}(t-\tau_n)\left[\hat{\mu}, \hat{\mathcal{G}}(\tau_n - \tau_{n-1})\left[\hat{\mu}, \ldots \hat{\mathcal{G}}(\tau_2 - \tau_1)\left[\hat{\mu}, \hat{\rho}(t_0)\right] \ldots\right]\right], \tag{1.5}$$

with $\hat{\mathcal{G}}(t)A \equiv \hat{K}_0(t_n)\hat{A}\hat{K}_0^\dagger(t_n)$. The polarization is then given by the expectation value the dipole operator,

$$\begin{aligned}\hat{P}(t) =&\hat{P}^{(0)}(t_0) + \sum_{n=1}^{\infty}\left(\frac{i}{\hbar}\right)^n \int_{t_0}^{t} \mathrm{d}\tau_n \int_{t_0}^{\tau_n} \mathrm{d}\tau_{n-1} \cdots \int_{t_0}^{\tau_2} \mathrm{d}\tau_1 E(\tau_n)E(\tau_{n-1})\cdots E(\tau_1) \\ &\mathrm{Tr}\left(\hat{\mu}\hat{\mathcal{G}}(t-\tau_n)\left[\hat{\mu}, \hat{\mathcal{G}}(\tau_n - \tau_{n-1})\left[\hat{\mu}, \ldots \hat{\mathcal{G}}(\tau_2-\tau_1)\left[\hat{\mu}, \hat{\rho}(t_0)\right]\ldots\right]\right]\right). \quad (1.6)\end{aligned}$$

Finally, we send $t_0 \to -\infty$, justifying our assumption that $\hat{\rho}(t_0)$ is the equilibrium density operator $\hat{\rho}$, and change integration variables to time intervals t_1, t_2, …, t_n with $t_1 \equiv \tau_2 - \tau_1$, $t_2 \equiv \tau_3 - \tau_2$, …, $t_n \equiv t - \tau_n$.

$$\begin{aligned}\hat{P}(t) = \hat{P}^{(0)}(-\infty) + &\sum_{n=1}^{\infty}\left(\frac{i}{\hbar}\right)^n \int_0^{\infty} \mathrm{d}t_n \int_0^{\infty} \mathrm{d}t_{n-1} \cdots \int_0^{\infty} \mathrm{d}t_1 \\ &E(t-t_n)E(t-t_n-t_{n-1})\cdots E(t-t_n-t_{n-1}-\cdots-t_1) \\ &\mathrm{Tr}\left(\hat{\mu}\hat{\mathcal{G}}(t_n)\left[\hat{\mu}, \hat{\mathcal{G}}(t_{n-1})\left[\hat{\mu}, \ldots \hat{\mathcal{G}}(t_1)\left[\hat{\mu}, \hat{\rho}\right]\ldots\right]\right]\right). \quad (1.7)\end{aligned}$$

The n$^{\text{th}}$ order vibrational response function is defined as the n$^{\text{th}}$ order correction to the polarization in the delta-function pulse limit,

$$\hat{R}^{(n)}(t_n, \ldots, t_1) = \left(\frac{i}{\hbar}\right)^n \mathrm{Tr}\left(\hat{\mu}\hat{\mathcal{G}}(t_n)\left[\hat{\mu}, \hat{\mathcal{G}}(t_{n-1})\left[\hat{\mu}, \ldots \hat{\mathcal{G}}(t_1)\left[\hat{\mu}, \hat{\rho}\right]\ldots\right]\right]\right) \quad (1.8)$$

2D IR spectra are generated by a four-wave mixing signal, and therefore correspond to the third order ($n = 3$) contribution to Eq. (1.7). From the response function in Eq. (1.8) and the electric field for each pulse the polarization in Eq. (1.7) can be computed. We are interested in computing contributions to the third order vibrational response function that produce coherent signals propagated in specific phase-matched directions, which correspond to distinct experimental observables. The real electric field is taken to consist of two components with positive and negative frequency

$$E(t) = \mathcal{E}(t)e^{i(\mathbf{k}\cdot\mathbf{r}-\omega t+\phi)} + \mathcal{E}^*(t)e^{i(-\mathbf{k}\cdot\mathbf{r}+\omega t-\phi)}. \quad (1.9)$$

The signal in a given direction $\mathbf{k}_s$ is obtained by multiplying Eq. (1.7) by $e^{-\mathbf{k}_s\cdot\mathbf{r}}$ and integrating $\mathbf{r}$ over the interaction volume of the sample. This will result in nonzero signal in specific phase-matched directions, related to the wavevectors of the electric field pulses by, $\mathbf{k}_s = \pm\mathbf{k}_1 \pm \mathbf{k}_2 \pm \mathbf{k}_3$.[7] We will additionally apply the rotating wave approximation,[11] which assumes that rapid oscillations in the integrand in Eq. (1.7) will cause phase cancellation if the field and molecular frequencies do not nearly cancel. This results in only one of the two terms in Eq. (1.9) contributing to Eq. (1.8) for each sequence of interactions with the field. The contribution associated with wavevector $\mathbf{k}_s = \alpha\mathbf{k}_1 + \beta\mathbf{k}_2 + \gamma\mathbf{k}_3$ for $n = 3$ is,

$$R^{(3)}_{\gamma\beta\alpha}(t_3, t_2, t_1) = \left(\frac{i}{\hbar}\right)^3 \mathrm{Tr}\left(\hat{\mu}_c^{\delta}\hat{\mathcal{G}}(t_3)\left[\hat{\mu}_c^{\gamma}, \hat{\mathcal{G}}(t_2)\left[\hat{\mu}_c^{\beta}, \hat{\mathcal{G}}(t_1)\left[\hat{\mu}_c^{\alpha}, \hat{\rho}\right]\right]\right]\right). \tag{1.10}$$

In Eq. (1.10) α, β, γ, and δ are $\pm$, with two signs $+$ and two signs $-$. For specificity we take the chromophore, c to interact with the field through the dipole operator, $\hat{\mu}_c$. Throughout this work we take the dipole operator to be proportional to the coordinate $\hat{q}_c$ with the constant of proportionality suppressed. The operators, $\hat{\mu}_c^{\pm}$ can then be expressed in terms of the boson creation and annihilation operators, $\hat{b}_c^{\dagger}$ and $\hat{b}_c$ as, $\hat{\mu}_c^{+} = \hat{q}_c^{+} = \hat{b}_c^{\dagger}\left(\hbar/2m_c\omega_c\right)^{1/2}$ and $\hat{\mu}_c^{-} = \hat{q}_c^{-} = (\hat{\mu}_c^{+})^{\dagger}$.

Several distinct processes can contribute to the signal in Eq. (1.10). For example, for a single degree of freedom expanding the commutators in Eq. (1.10) yields contributions from eight distinct sequences of interactions with the electric field. Double-sided Feynman diagrams[5,6,11,71,72] (2FDs), which portray the perturbative time-evolution of the density operator, are conventionally used to represent these distinct contributions to quantum mechanical response function. Two example 2FDs contributing to the $\mathbf{k}_{\mathrm{I}} = -\mathbf{k}_1 + \mathbf{k}_2 + \mathbf{k}_3$, $\mathbf{k}_{\mathrm{II}} = \mathbf{k}_1 - \mathbf{k}_2 + \mathbf{k}_3$ and $\mathbf{k}_{\mathrm{III}} = \mathbf{k}_1 + \mathbf{k}_2 - \mathbf{k}_3$ responses in Eq. (1.10) are shown in Fig. 1.2(a)-(c). In these diagrams, time runs vertically with the left and right vertical lines representing the ket and bra aspects of the density operator, respectively. Each arrow repre-

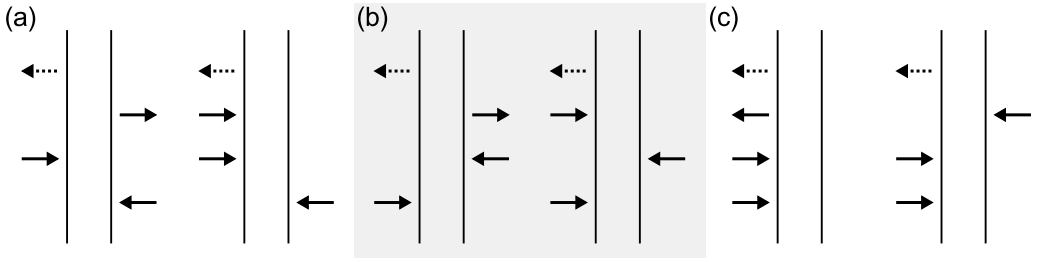

Figure 1.1: Two double-sided Feynman diagrams contributing to the $\mathbf{k}_{\mathrm{I}}$, $\mathbf{k}_{\mathrm{II}}$, and $\mathbf{k}_{\mathrm{III}}$ phase-matched directions are shown in panels (a)-(c), respectively. The left diagram in each panel corresponds to absorption at times 0 and t_1 and deexcitation at times $t_1 + t_2$ and $t_1 + t_2 + t_3$. The right diagram corresponds to absorption in the first three interactions with the field and deexcitation at time $t_1 + t_2 + t_3$.

sents an interaction with the electric field at time 0, t_1, $t_1 + t_2$ or $t_1 + t_2 + t_3$, from bottom to top. Within the rotating wave approximation, arrows pointing to the right correspond to interactions with the electric field through the first term in Eq. (1.9) with 'positive phase', and arrows pointing to the left correspond to interactions with the second term with 'negative phase'. Therefore, right pointing arrows correspond to instances of the creation operator in Eq. (1.10) and left pointing arrows to instances of the annihilation operator. In the limit of harmonic selection rules this leads to the intuitive picture that an arrow pointing toward the density operator causes absorption and an arrow pointing away from the density operator causes deexcitation.

1.3 Purely Absorptive Spectra

For multidimensional experiments, the response function contribution from Eq. (1.10) is typically Fourier transformed with respect to t_1 and t_3 so that a series of 2D spectra are generated as a function of t_2, often called the waiting time. Figure 1.2 shows the imaginary part of response function contributions cor-

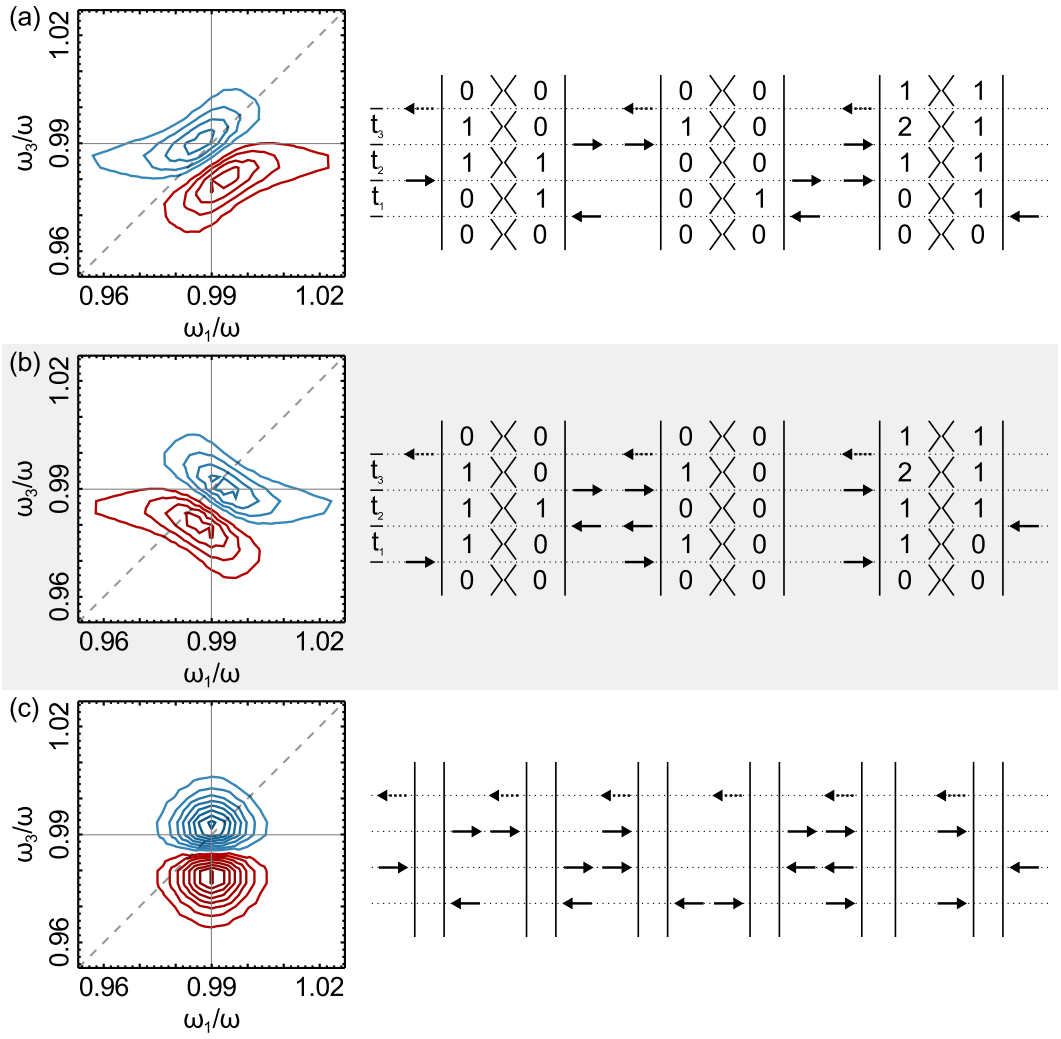

Figure 1.2: Im $\left[\tilde{R}^{(3)}_{\mathrm{I}}(\omega_3, -\omega_1; t_2)\right]$ and Im $\left[\tilde{R}^{(3)}_{\mathrm{II}}(\omega_3, \omega_1; t_2)\right]$ are shown in panels (a) and (b) respectively for a thermal ensemble of Morse oscillators coupled to a dissipative bath for a long waiting time. $R_{\mathrm{abs}}(\omega_3, \omega_1; t_2)$, obtained by combining the responses in (a) and (b) as in Eq. (1.11) is shown in (c). The 2FDs contributing to each signal are shown at right, assuming the oscillator can only access the ground state at thermal equilibrium.

responding to wavevectors $\mathbf{k}_{\mathrm{I}}$ and $\mathbf{k}_{\mathrm{II}}$ in panels (a) and (b), respectively. Due to an additional factor of i in the definition of the measured emitted signal, $S(t_3, t_2, t_1) \propto iR(t_3, t_2, t_1)$, the imaginary contributions to the spectra here correspond to the real contributions to the measured signal in Ref. 5. These spectra were generated for a single Morse oscillator coupled to a dissipative bath as described in Sec. 5.1. Assuming the chromophore begins in the ground state, three 2FDs contribute to the signal in each phase-matched direction, shown to the right in each panel. The 2FDs in (a) and (b) are drawn to emphasize the density operator time evolution in the limit of harmonic selection rules. In this limit, the time dependence in Eq. (1.10) of the density operator $|n_l\rangle \langle n_r|$ will correspond to frequency, $|E_l - E_r|/\hbar$. In practice, peaks are broadened due to interactions with the bath but, nonetheless this correspondence allows for 2FDs to be assigned to spectral peaks by relating the frequencies during the t_1 and t_3 time periods to ω_1 and ω_3. For example, all 2FDs in Fig. 1.2(b) correspond to frequency ω_{10} during the t_1 time period. This frequency corresponds to $\omega_1 = 0.99\omega$, roughly the center of both peaks in the spectrum in Fig. 1.2(b). In contrast, the 2FDs in row (a) each correspond to the frequency $-\omega_{10}$ during the t_1 time period. The frequency during the t_1 time period for the $\mathbf{k}_{\mathrm{I}}$ phase-matched direction is always negative so that it is typical to present this spectrum with the sign of the ω_1 frequency reversed. Therefore, the spectrum in (a) is $\mathrm{Im}\left[\tilde{R}^{(3)}_{\mathrm{I}}(\omega_3, -\omega_1; t_2)\right]$ with $\tilde{R}^{(3)}(\omega_3, \omega_1; t_2)$ the one-sided Fourier transform of $R^{(3)}(t_3, t_2, t_1)$ with respect to t_1 and t_3 . During the t_3 time period the left two 2FDs in panel (a) evolve with frequency ω_{10}. These 2FDs therefore contribute to the upper (blue) peak in panel (a) which has its center close to the diagonal. The phases accumulated during the t_1 and t_3 time period have opposite sign, so that the accumulated phases will exactly cancel for $t_1 = t_3$. For this reason, the $\mathbf{k}_{\mathrm{I}}$ phase-matched direction is called the 'rephasing'

signal. The right most 2FD in Fig. 1.2(a) corresponds to frequency ω_{21} during the t_3 time period. For an anharmonic oscillator ω_{21} will be offset from ω_{10} by the oscillators anharmonicity, Δ_{anh}. This diagram therefore contributes to the lower (red) peak in panel (a) and has opposite sign due to the expansion of the commutators in Eq. (1.10). The fundamental and anharmonic peaks in the signal in Fig. 1.2 have roughly equal contribution, because for a nearly harmonic system, $\hat{\mu}_{21} \approx 2\hat{\mu}_{10}$. For a harmonic system, this equality holds exactly and $\Delta_{\text{anh}} = 0$, so that the two peaks will overlap and cancel. Therefore, for a harmonic system, $R^{(3)}_{\alpha\beta\gamma}(t_3, t_2, t_1) = R^{(3)}(t_3, t_2, t_1) = 0$. A similar analysis of the relationship between the 2FDs and 2D IR spectra in panel (b) can be made. For these 2FDs the t_1 and t_3 frequencies occur with the same phase so that the contribution from the $\mathbf{k}_{\text{II}}$ signal is the 'nonrephasing' signal.

Because the spectra generated by Eq. (1.10) are complex valued, the contribution from each time interval will be composed of a real (absorptive) part and an imaginary (dispersive) part.[5] Therefore, taking the real or imaginary part of a phase-matched signal will not give a purely absorptive contribution to the signal; resulting in phase-twist in the spectrum from the dispersive contributions,[5,73] as can be seen in panels (a) and (b) of Fig. 1.2. The purely absorptive spectrum,[5,43,73] $R_{\text{abs}}(\omega_3, \omega_1; t_2)$, is obtained by combining the rephasing, $R_{\text{I}} = R_{++-}$, and nonrephasing, $R_{\text{II}} = R_{+-+}$ responses

$$R_{\text{abs}}(\omega_3, \omega_1; t_2) \equiv \text{Im}\left[\tilde{R}^{(3)}_{\text{I}}(\omega_3, -\omega_1; t_2) + \tilde{R}^{(3)}_{\text{II}}(\omega_3, \omega_1; t_2)\right]. \tag{1.11}$$

By taking this combination of spectra the wings cancel, as seen in Fig. 1.2(c), making the peaks better resolved and line shapes more easily interpreted without the distortions caused by dispersive contributions to the signal.

Chapter 2

The Optimized Mean-Trajectory Approximation

In Chapter 1 an expression for the n^{th} order vibrational response functions was derived and double-sided Feynman diagrams (2FDs) were introduced as a convenient tool for visualizing distinct contributions to the third order response function. These 2FDs are the starting point for the derivation of the optimized mean-trajectory (OMT) approximation which results from translating pairs of quantum mechanical 2FDs into semiclassical OMT diagrams. There are two key aspects to this derivation. First, the time-evolution of the density operator is approximated semiclassically by the evolution of a classical trajectory with quantized action values. Second, the response function is approximated as a sum of appropriately chosen four-point correlation functions evaluated along such classical trajectories. The identification of 2FDs with OMT diagrams relies on evaluating 2FDs in a harmonic approximation to the energy eigenstate basis and on the analogy between energy eigenstates in quantum mechanics and the invariant tori defined by the classical-mechanical action-angle variables,[55] in cases where the latter can be defined. In analogy to free propagation in the energy basis interrupted by radiation-induced transitions between eigenstates in 2FDs, in OMT diagrams classical trajectories are propagated at quantized action values connected by jumps in action at constant angle representing radiation-matter interactions. Derivations below will be focused on the third order response function. It is a straight forward exercise to apply the approach to other orders.

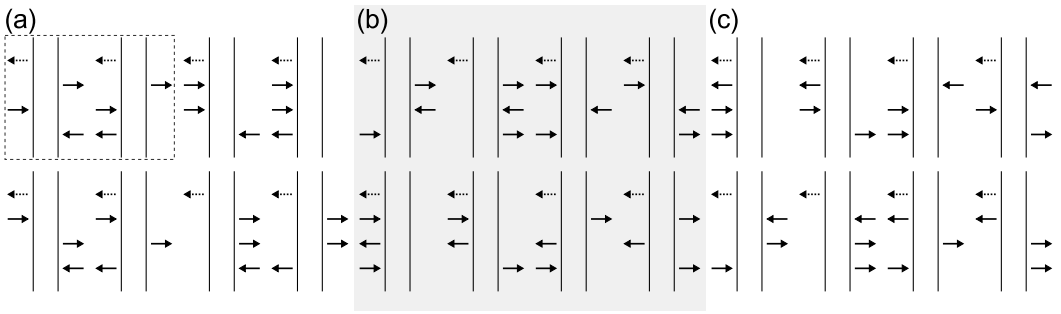

Figure 2.1: The eight 2FDs contributing to (a) $R^{(3)}_{++-}$, (b) $R^{(3)}_{+-+}$, and (c) $R^{(3)}_{-++}$

2.1 One Degree of Freedom

Consider a quantum mechanical system consisting of a single degree of freedom described by Hamiltonian $\hat{H}$ in terms of the coordinate and momentum operators, $\hat{q}$ and $\hat{p}$. This system can also be described by eigenstates of the Hamiltonian, $|n\rangle$, with quantum number n. The corresponding classical Hamiltonian is taken to be H, defined as a function of the coordinate q and its conjugate momentum p. For a single degree of freedom, action-angle variables, J and ϕ are guaranteed to exist for which the conjugate momentum J is a constant of the motion and the angle ϕ evolves linearly with time.

For such a system, the quantum mechanical response function in Eq. (1.10) with $\hat{q}_c = \hat{q}$ can be described by eight 2FDs evaluated in the energy eigenstate basis with harmonic selection rules. These eight diagrams correspond to the contributions to the system response obtained by expanding the three commutators in Eq. (1.10). The final interaction with the field is taken to cause deexcitation of the ket aspect of the density operator. These eight diagrams are shown in Fig. 2.1 for the signal associated with wavevectors (a) $\mathbf{k}_{\mathrm{I}} = -\mathbf{k}_1 + \mathbf{k}_2 + \mathbf{k}_3$, (b) $\mathbf{k}_{\mathrm{II}} = \mathbf{k}_1 - \mathbf{k}_2 + \mathbf{k}_3$ and (c) $\mathbf{k}_{\mathrm{III}} = \mathbf{k}_1 + \mathbf{k}_2 - \mathbf{k}_3$. These 2FDs can be associated into pairs that undergo the same time evolution during the t_1, t_2 and t_3 time periods but that contribute to Eq. (1.10)

with different statistical weight. One such pair is boxed in Fig. 2.1(a). In addition to the density operator time propagation, each 2FD encodes a thermal average over a four-point correlation function that defines its contribution to the third order response function. For example, the contribution to the response function from the boxed pair of 2FDs in Fig. 2.1(a) is,

$$\frac{i}{2^4\hbar^3}\mathrm{Tr}\left\{\hat{Q}_-(t_3+t_2+t_1)\hat{Q}_+(t_1)\left[\hat{Q}_-,\hat{\rho}\right]\hat{Q}_+(t_2+t_1)\right\}. \tag{2.1}$$

The overall sign is determined by the expansion of the two outer commutators in Eq. (1.10). We will evaluate this pair of diagrams in the harmonic limit, with $\hat{Q}_\sigma$ defined in terms of the boson creation and annihilation operators $b^\dagger$ and b as $\hat{Q}_- = \sqrt{\frac{2\hbar}{m\omega}}\hat{b}$ and $\hat{Q}_+ = \sqrt{\frac{2\hbar}{m\omega}}\hat{b}^\dagger$. It should be emphasized that the nonlinear response function in Eq. (1.10) necessarily vanishes for a harmonic potential. However, each 2FD in Fig. 2.1, and each pair of diagrams undergoing the same evolution during each time interval, individually result in nonzero contribution. This permits the use of the harmonic limit of pairs of 2FDs in our analysis. In the harmonic eigenstate basis, the matrix elements of the Q_σ operators are,

$$\langle n|\,\hat{Q}_-(t)\,|n'\rangle = \sqrt{\frac{2n'\hbar}{m\omega}}e^{-i\omega_{n',n}t}\delta_{n+1,n'} \tag{2.2a}$$

$$\langle n|\,\hat{Q}_+(t)\,|n'\rangle = \sqrt{\frac{2n\hbar}{m\omega}}e^{i\omega_{n,n'}t}\delta_{n,n'+1} \tag{2.2b}$$

Although we are evaluating Eq. (2.1) in a harmonic limit, the frequencies $\omega_{n,n'} \equiv (E_n - E_{n'})/\hbar$ are left in a general form. Evaluating Eq. (2.1) with the harmonic selection rules in Eq. (2.2) results in the contribution to the response function,

$$\frac{-i}{4m^2\omega^2\hbar}\sum_{n=0}^{\infty}(\rho_{nn}-\rho_{n+1,n+1})\,(n+1)^2 e^{i\omega_{n+1,n}(t_1-t_3)}. \tag{2.3}$$

The difference of density operator matrix elements results from including the two 2FDs through the commutator in Eq. (2.1).

We define the OMT approximation so that the signal from each such pair of 2FDs is reproduced in the harmonic limit. The OMT approximation for the contribution to the quantum mechanical response function in Eq. (2.1) is,

$$\frac{-i}{2^4\hbar^5}\int \mathrm{d}\mathbf{z}_1 \int \mathrm{d}\mathbf{z}_2 \int \mathrm{d}\mathbf{z}_3 \Delta F(\mathbf{z}_1)\Gamma(\mathbf{z}_1)\Delta_{1+}\Delta_{2-}\delta\left(\phi_2-\phi_1(t_1)\right)\delta\left(\phi_3-\phi_2(t_2)\right) \times Q_-(\mathbf{z}_1)Q_+(\mathbf{z}_1(t_1))Q_+(\mathbf{z}_3)Q_-(\mathbf{z}_3(t_3)), \tag{2.4}$$

with,

$$\Delta F(\mathbf{z}) \equiv F(\mathbf{z})|_{J\to J-\hbar/2} - F(\mathbf{z})|_{J\to J+\hbar/2}, \tag{2.5}$$

$$F(\mathbf{z}) \equiv \frac{e^{-\beta H(\mathbf{z})}}{\int d\mathbf{z}' e^{-\beta H(\mathbf{z}')}\hbar\sum_{n=0}^{\infty}\delta\left(J-(n+1/2)\,\hbar\right)}, \tag{2.6}$$

$$\Gamma(\mathbf{z}) \equiv \hbar\sum_{n=1}^{\infty}\delta(J-n\hbar), \tag{2.7}$$

$$\Delta_{\tau\pm} \equiv \hbar\delta\left(J_{\tau+1}-(J_\tau \pm \hbar/2)\right), \tag{2.8}$$

$$Q_\pm(\mathbf{z}(t)) \equiv q(t) \mp ip(t)/(m\omega). \tag{2.9}$$

Although Eq. (2.4) is given explicitly as an integration over three two-dimensional phase space variables, the delta functions in angle in Eq. (2.4) and action in Eq. (2.8) reduce the evaluation of Eq. (2.4) to a numerical integration over the initial phase space variables, $\mathbf{z}_1$. The evaluation is further reduced to a sum over the initial action J_1 by the factor $\Gamma(\mathbf{z})$ defined in Eq. (2.7). These delta functions allow for Eq. (2.4) to be interpreted as the result of evaluating a semiclassical OMT diagram that includes an average over initial conditions J_1 and ϕ_1 in the same sense that Eq. (2.1) is the result of evaluating the boxed pair of 2FDs in Fig. (2.1)(a). The pair of 2FDs are described by a single OMT diagram through the difference of the renormalized classical distributions in the factor ΔF, defined in Eq. (2.5), analogous to the difference in density operator matrix elements in Eq. (2.3). In the harmonic limit, $\Delta F(\mathbf{z}_1) = \hbar^{-1}\left(\rho_{nn}-\rho_{n+1,n+1}\right)$ due to the action quantization conditions in Eqs. (2.7) and (2.5) and the renormalization of

the classical distribution in Eq. (2.6). OMT diagrams consist of two parts. The first is an underlying path, defined by the delta functions in Eqs. (2.4), (2.7) and (2.8), which approximates the evolution of the density operator by the evolution of linked classical trajectories with discrete action values. The underlying OMT path ensures that the correct frequency dependences in Eq. (2.3) are obtained in the harmonic limit from evaluating the factors Q_σ, defined in Eq. (2.9). The second part of each OMT diagram is the four factors of Q_σ evaluated along the path whose placement generate the correct factor, $(n+1)^2$, in Eq. (2.3). In the remainder of this section the equivalence of Eq. (2.1) and Eq. (2.4) in the harmonic limit will be demonstrated and the general correspondence between pairs of 2FDs and OMT diagrams made explicit.

The evolution of the density operator $|n_l\rangle \langle n_r|$ in a 2FD is approximated in the OMT method by a classical trajectory with action given by the mean action associated with the bra and ket aspects of the density operator in the harmonic limit. This action is obtained from the mean quantum number $\bar{n} \equiv (n_l + n_r)/2$ for a population ($n_l = n_r$) or coherence ($n_l \neq n_r$). The quantum mechanical and classical energies for a single harmonic degree of freedom are $E_n = (n+1/2)\hbar\omega$ and $E = J\omega$, respectively. Therefore, the mean action corresponding to the average quantum number $\bar{n}$ is given by, $J(\bar{n}) \equiv (\bar{n} + 1/2)\hbar = (n_l + n_r + 1)\hbar/2$. Within this harmonic approximation, each interaction with the electric field will increase or decrease n_l or n_r by 1, corresponding to an increase or decrease in the action of the classical trajectory by $\hbar/2$. These jumps in action are controlled by the factors $\Delta_{\tau\sigma}$ defined in Eq. (2.8). We take this interaction to leave the value of the angle variable unchanged as dictated by the delta functions in angle in Eq. (2.4). In this way, the quantum mechanical 2FDs are translated into OMT paths consisting of a series of classical trajectories linked by discrete jumps in action at constant angle,

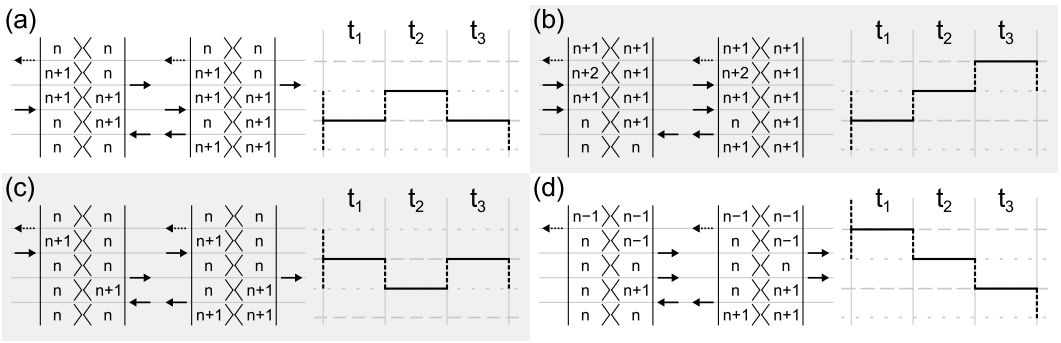

Figure 2.2: 2FDs contributing to rephasing signal, $R^{(3)}_{++-}$, are shown with their corresponding OMT paths.

representing radiation-matter interactions.

In Fig. 2.2 the eight 2FDs contributing to the rephasing signal, $R^{(3)}_{++-}$ are shown. For clarity, the evolution of the density operator is explicitly given in the energy basis with harmonic selection rules. To the right of each pair of 2FDs is the corresponding OMT path. To illustrate the correspondence between 2FDs and OMT paths, consider the 2FDs that generate the signal in Eq. (2.1) shown in Fig. 2.2(a). One of these 2FDs begins with the density operator $|n\rangle\langle n|$ and the other with $|n+1\rangle\langle n+1|$. The mean quantum numbers for these populations are $\bar{n} = n$ and $\bar{n} = n+1$, respectively, corresponding to initial actions $J_0 = (n+1/2)\hbar$ and $J_0 = (n+3/2)\hbar$. In both diagrams, the first interaction with the electric field at time 0 produces the coherence $|n\rangle\langle n+1|$, with $\bar{n} = n+1/2$, corresponding to action $J_1 = (n+1)\hbar$. The second interaction at time $t_1 + t_2$ yields the population $|n+1\rangle\langle n+1|$ with $\bar{n} = n+1$ and corresponding action $J_2 = (n+3/2)\hbar$. The third interaction produces the coherence $|n+1\rangle\langle n|$ with $\bar{n} = n+1/2$ and action $J_3 = J_1$. The final interaction returns the density operator to a population, $|n\rangle\langle n|$, as required by the trace in Eq. (1.10), corresponding to action $J_4 = (n+1/2)\hbar$. In each OMT path in Fig. 2.2 two possible initial interactions with the field are shown as two dashed vertical lines, one increasing and the other decreasing the

action. These correspond to transitions from the two initial actions J_0, that are associated with the left and right 2FDs, with an initial increase and decrease in quantum number, respectively. Following the initial interaction, the OMT path in Fig. 2.2(a) indicates classical propagation at action J_1 for time t_1 by a horizontal solid line. The second interaction with the field at time t_1 increases the oscillator's action by $\hbar/2$ to J_2 and is followed by propagation for time t_2 at this action. The third dashed vertical line decreases the action by $\hbar/2$ to J_3 indicating deexcitation at time $t_1 + t_2$ in the 2FDs, and is followed by propagation for time t_3. The final dashed vertical line decreases the action by $\hbar/2$ to J_4. This analysis can be applied to the remaining three pairs of 2FDs in Fig. 2.2 to obtain the OMT path in each panel. Although Fig. 2.2 explicitly shows 2FDs contributing to the rephasing signal, increasing or decreasing the quantum number with each radiation-matter interaction will translate to a corresponding increase or decrease in action in an OMT diagram, regardless of the phase-matched direction. Therefore, the OMT paths in Fig. 2.2 show the four possible combinations of field interactions and consequently describe the contribution to the response function in each phase-matched direction. This approximation of the density operator evolution will result in the correct frequency dependence of the system response in the harmonic limit as discussed below in connection with Eqs. (2.14) and (2.17).

In addition to the path, which approximates the density operator time evolution, OMT diagrams encode a four-point correlation function involving the classical functions corresponding to the quantum mechanical operators, $\hat{Q}_\sigma$. These classical functions are defined in Eq. (2.9). The factors of Q_σ correspond to the four interactions with the electric field at times 0, t_1, $t_1 + t_2$ and $t_1 + t_2 + t_3$, as in Eq. (2.1) for the quantum mechanical response. The factors of $Q_\sigma(t)$ are defined so that, in the harmonic limit, the quantum mechanical result in Eq. (2.1) is recovered.

For a harmonic oscillator these factors can be written as a function of action-angle variables as,

$$Q_{\pm}(t) = \sqrt{\frac{2J}{m\omega}} \exp(\pm i\phi(t)). \tag{2.10}$$

with action J and angle $\phi(t) = \omega t + \phi_0$. In this limit, correspondence with the quantum result is achieved by evaluating the classical factors in Eq. (2.10) at the action corresponding to the larger of the two quantum numbers being transitioned between in each interaction with the field. It is important to note that this is distinct from evaluating these factors at the action corresponding to the larger of the two average quantum numbers transitioned between in the OMT path. Furthermore, this choice will not affect the time evolution of the angle, $\phi(t)$, which is determined by the underlying path. Evaluating these factors at the action associated with the larger of the two quantum numbers transitioned between in a 2FD will result in all factors of Q_σ being evaluated at integer multiples of $\hbar$, corresponding to the factors of n' and n in the square roots of Eq. (2.2).

In Fig. 2.3 this selection of points is illustrated for the pairs of 2FDs associated with wavevector $\mathbf{k}_{\mathrm{I}}$ in column (i) and wavevector $\mathbf{k}_{\mathrm{III}}$ in column (ii). The 2FDs in this figure are drawn to emphasize the bra and ket aspects of the density operator with harmonic selection rules. The corresponding OMT diagrams are shown adjacent to each pair of 2FDs. Figure 2.3(ai) shows the OMT diagram corresponding to the signal in Eq. (2.4). In both 2FDs in this panel the first interaction with the field causes a transition between states defined by quantum numbers n and $n+1$ for either the ket or bra aspect of the density operator. This corresponds to the factor Q_- at time 0 being evaluated at action $J_1 = (n+1)\hbar$, represented by the red dot at the start of the first trajectory in the OMT diagram in Fig. 2.3(ai). The second interaction also causes a transition between states represented by quantum numbers n and $n+1$ in both 2FDs, corresponding to evaluating Q_+ at time t_1 at

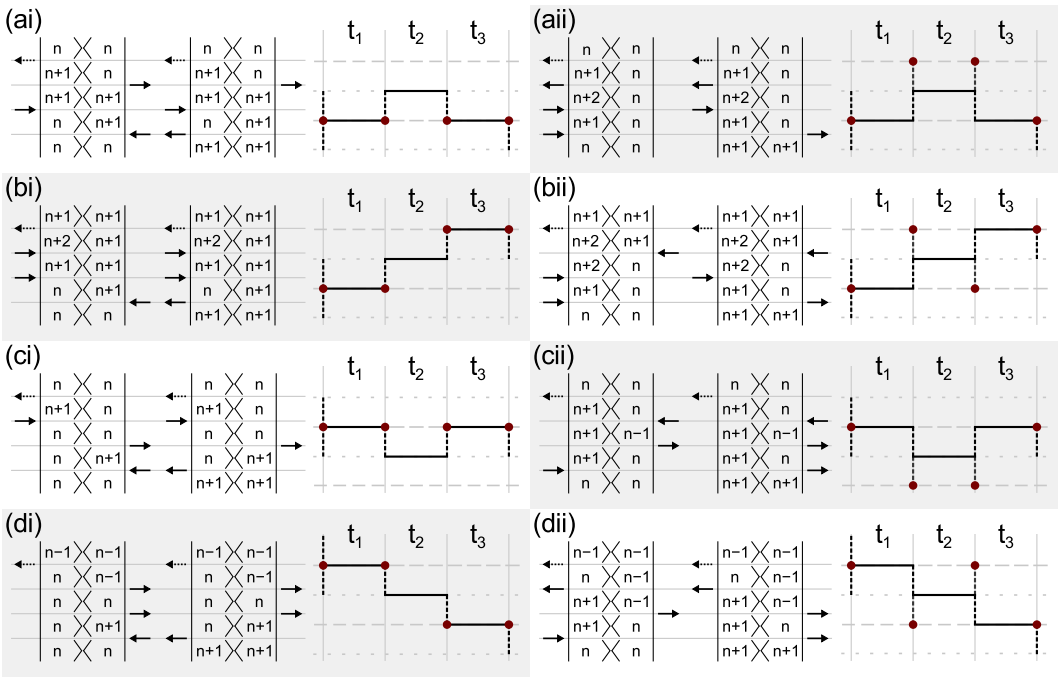

Figure 2.3: Double-sided Feynman diagrams associated with wavevector $\mathbf{k}_{\mathrm{I}}$ are shown in column (i) and with wavevector $\mathbf{k}_{\mathrm{III}}$ in column (ii) with their corresponding OMT diagrams. OMT diagrams in each row correspond to the same semiclassical path but with factors of Q_σ evaluated at different actions, as indicated by the placement of the red dots.

action $(n+1)\hbar$, represented by the red dot at the end of the first classical trajectory in the OMT diagram. Similarly, the final two interactions cause transitions between the states represented by quantum numbers n and $n+1$ so that the factors of Q_σ associated with these times are each evaluated at $J_3 = J_1 = (n+1)\hbar$, as shown by the red dots at the start and end of the third trajectory in the OMT diagram. The dot placements in Fig. 2.3(ai) are indicated by the arguments of the Q_σ factors in the term $Q_-(\mathbf{z}_1)Q_+(\mathbf{z}_1(t_1))Q_+(\mathbf{z}_3)Q_-(\mathbf{z}_3(t_3))$ in Eq. (2.4). The OMT diagrams in each panel of Fig. 2.3 are generated in this manner. The first radiation-matter interaction can always be taken to either cause a population with $\bar{n} = n$ to undergo absorption or with $\bar{n} = n+1$ to undergo stimulated emission, generating a coherence with $\bar{n} = n + 1/2$, Therefore, the factor of Q_σ at time 0 in each OMT path is evaluated at action $J_1 = (\bar{n}+1/2)\hbar = (n+1)\hbar$ for both 2FDs in

a given pair. This ensures that these pairs of 2FDs can be represented by a single OMT diagram.

The 2FDs in column (i) of Fig. 2.3 have the same average quantum number during each time interval as those in the corresponding panel of column (ii). This results in the OMT diagrams in each row having the same underlying OMT path. However, the quantum numbers transitioned between in each interaction are not the same, so that the factors of Q_σ in the two OMT diagrams in each row are evaluated at distinct action values. For example in Fig. 2.3(aii), the interactions with the field at time t_1 and $t_1 + t_2$ cause transitions between states with the quantum numbers $n + 1$ and $n + 2$, and not n and $n + 1$ as in the 2FDs in (ai). These transitions correspond to the factors Q_+ and Q_-, evaluated at times t_1 and t_1+t_2, respectively, each being evaluated at action $J_2+\hbar/2$, as illustrated by the red dots at these times in the OMT diagram in Fig. 2.3(aii). Unlike the OMT diagrams in column (i) of Fig. 2.3, in column (ii) the Q_σ factors are evaluated at actions not associated with the path itself. This is characteristic of paths propagated in a two-quantum coherence. The distinction of dot placement in column (i) and (ii) for rows (a), (b) and (d) are small. As a result of the factorization of the action and angle dependence of the Q_σ factors in Eq. (2.10), the dot placements in (b) and (d) result in identical evaluation in the harmonic limit. However, using the dot placement in (ai) to evaluate the signal represented in (aii) would result in an underestimation of this diagrams contribution by $(1 + \hbar/(2J_1))^{-1}$. The discrepancy that would result from evaluating the signal in (cii) according to the dot placement in (ci) is the most severe. For $n = 0$, Fig. 2.3(cii) does not contribute to the response function, as this sequence of interactions would require emission from the ground state. The diagram in panel (ci), however, contributes for $n = 0$. The specification of these correlation points is an important deviation from the MT method,[63–65]

as discussed in Appendix B, and allows waiting time dynamics of two-quantum coherences to be successfully computed with the OMT approximation.

Evaluating the OMT diagram in Fig. 2.3(ai) according to the expression in Eq. (2.4) with the harmonic approximation of Eq. (2.10) gives,

$$\frac{-i}{4m^2\omega^2}\sum_{n=0}^{\infty}\Delta F(\mathbf{z}_1)(n+1)^2 e^{i(\phi_1(t_1)-\phi_1)}e^{-i(\phi_3(t_3)-\phi_3)}. \tag{2.11}$$

The sum over n is shifted in Eq. (2.11) for comparison with Eq. (2.3). The integration over ϕ_1 was performed analytically since, in the harmonic limit, $\phi_1(t_1) - \phi_1 = \phi_3(t_3) - \phi_3 = \omega t$, so that the integrand has no functional dependence on ϕ_1. Also, there is no t_2 dependence in either Eq. (2.3) or Eq. (2.11) because within the harmonic approximation this model does not include dynamics for a population. The dependences on t_1 and t_3 in the quantum and semiclassical expressions are equal in the event that the quantum frequency associated with a one-quantum coherence and the time dependence of the classical angle variable are related by $\omega_{n+1,n}t = \phi_\tau(t) - \phi_\tau$ with

$$\phi_t = \phi_0 + \omega(J)t, \tag{2.12}$$

$$\omega(J) \equiv \frac{dH(J)}{dJ}. \tag{2.13}$$

Making the substitution $\bar{n} = n + 1/2$ to account for propagating the classical trajectories at the mean action variable, the time dependences are identical if

$$\frac{E_{\bar{n}+1/2} - E_{\bar{n}-1/2}}{\hbar} = \left.\frac{dH(J)}{dJ}\right|_{J=(\bar{n}+1/2)\hbar}. \tag{2.14}$$

The equality in Eq. (2.14) holds exactly for a harmonic oscillator. For an anharmonic oscillator, the quantum energy E_n can be expanded in a power series in $n + 1/2$ and the classical energy $H(J)$ can correspondingly be expanded in powers of J. The equality in Eq. (2.14) also holds for a Morse potential with energy quadratic in J. For a general anharmonic system, Eq. (2.14) is approximate. This

demonstrates that for the choice of action values used to propagate trajectories in the OMT approximation, the frequencies of one-quantum coherences in 2FDs are exactly reproduced for a harmonic oscillator and approximately reproduced to higher order. This ensures that Eq. (2.1) and Eq. (2.4) evaluate to the same result in the harmonic limit. In the $\mathbf{k}_{\mathrm{III}}$ phase-matched direction, two-quantum coherences are propagated during the waiting time as in the 2FDs in column (ii) of Fig. 2.3. The correspondence between 2FDs and OMT diagrams in the harmonic limit also holds for these diagrams. For example, evaluating the 2FDs in Fig. 2.3(aii) in the harmonic limit results in the contribution to the system response,

$$\frac{-i}{4m^2\omega^2\hbar}\sum_{n=0}^{\infty}\left(\rho_{nn}-\rho_{n+1,n+1}\right)(n+1)(n+2)e^{-i\omega_{n+1,n}(t_1+t_3)}e^{-i\omega_{n+2,n}t_2}, \tag{2.15}$$

with the corresponding OMT diagram evaluation,

$$\frac{-i}{4m^2\omega^2}\sum_{n=0}^{\infty}\Delta F(\mathbf{z}_1)(n+1)(n+2)e^{-i(\phi_1(t_1)-\phi_1)}e^{-2i(\phi_2(t_2)-\phi_2)}e^{-i(\phi_3(t_3)-\phi_3)}. \tag{2.16}$$

Although Eqs. (2.15) and (2.16) are derived within a harmonic approximation the frequency dependences in each equation are left in a more general form to allow for an approximate comparison of the quantum mechanical and OMT results for an anharmonic oscillator. The evolution of frequencies associated with one-quantum coherences in Eq. (2.15) during the t_1 and t_3 time periods are reproduced by the OMT result in Eq. (2.16), as evident from Eq. (2.14). Equations (2.15) and (2.16) will therefore be equivalent if these expressions have the same frequency dependence during t_2,

$$\frac{E_{\bar{n}+1}-E_{\bar{n}-1}}{\hbar}=2\frac{dH(J)}{dJ}\bigg|_{J=(\bar{n}+1)\hbar}. \tag{2.17}$$

This equality is exact for a harmonic potential and is approximate for an anharmonic potential. This demonstrates that OMT diagrams reproduce the results of

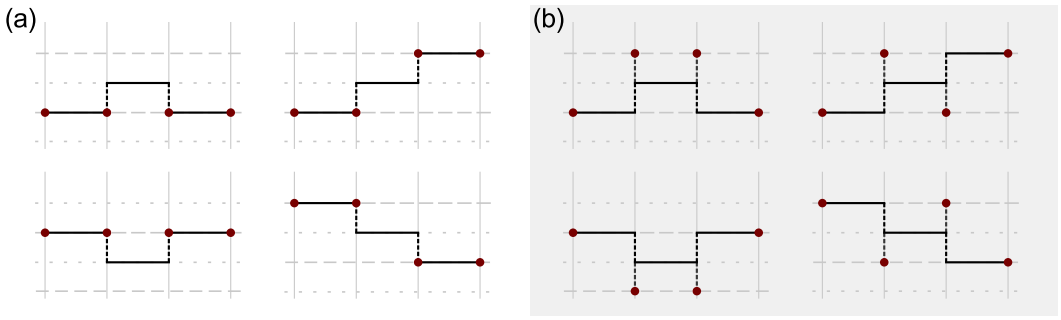

Figure 2.4: OMT diagrams for one degree of freedom. Diagrams in (a) are associated with signals undergoing population dynamics during the waiting time, such as in the signal associated with the $\mathbf{k}_{\mathrm{I}}$ and $\mathbf{k}_{\mathrm{II}}$ wavevectors. Diagrams in (b) are associated with signals characterized by two-quantum coherences during the waiting time, such as the signal associated with wavevector $\mathbf{k}_{\mathrm{III}}$.

their corresponding 2FDs, including the time dependences of populations and one- and two-quantum coherences, in the harmonic limit.

The complete set of OMT diagrams for a single degree of freedom are presented in Fig. 2.4. Expanding the three commutators in Eq. (1.10) for any phase-matching condition yields eight terms, each of which is represented by a 2FD. These eight 2FD associate in pairs to produce four OMT diagrams. There are two distinct sets of OMT diagrams, distinguished by whether they represent populations during the waiting time, as in Fig. 2.4(a), or coherences during the waiting time, as in Fig. 2.4(b). The final and initial interactions with the field are not shown, since they do not effect the evaluation of the diagrams. The OMT approximation for the third order response function generated by these diagrams is,

$$R^{(3)}_{\gamma\beta\alpha}(t_3,t_2,t_1) = \frac{i}{2^4\hbar^5}\sum_{d=1}^{4}\epsilon_d \int \mathrm{d}\mathbf{z}_1 \int \mathrm{d}\mathbf{z}_2 \int \mathrm{d}\mathbf{z}_3 \Delta F(\mathbf{z}_1)\Gamma(\mathbf{z}_1)\Delta_{1\sigma_d}\Delta_{2\sigma'_d}$$
$$\times\, \delta\left(\phi_2-\phi_1(t_1)\right)\delta\left(\phi_3-\phi_2(t_2)\right) Q_\alpha(\mathbf{z}_1)Q_\beta(\mathbf{z}'_d)Q_\gamma(\mathbf{z}''_d)Q_\delta(\mathbf{z}_3(t_3)). \qquad (2.18)$$

The index d labels the four semiclassical diagrams in either (a) or (b) of Fig. 2.4. The overall sign ϵ_d results from expanding the two outermost commutators in

Eq. (1.10). For the diagrams in Fig. 2.4 with the interactions at time t_1 and $t_1 + t_2$ causing opposite change in the oscillators action, $\epsilon_d = -1$, as in the first column of each panel. For diagrams with these interactions causing the same change in action, as in the second column in each panel, $\epsilon_d = 1$. The factor of $\Delta F(\mathbf{z}_1)$ includes contributions from two 2FDs in a single OMT diagram. The factors $\Gamma(\mathbf{z}_1)$ and $\Delta_{\tau\sigma_d}$ are delta functions in action variables defined in Eqs. (2.7) and Eq. (2.8). Together with the delta functions in angle in Eq. (2.18), these factors define the underlying path of the diagram d. The Q_σ factors define the points along the path used to evaluate the response function. In all OMT diagrams, Q_α is evaluated at $\mathbf{z}_1$ and Q_δ at $\mathbf{z}_3(t_3)$, but the phase space points at which Q_β and Q_γ are evaluated, $\mathbf{z}'_d$ and $\mathbf{z}''_d$ respectively, vary according to diagram and phase-matched direction, as shown by the placement of red dots in Fig. 2.4. Although the OMT approximation was derived within a harmonic approximation to 2FDs, Eq. (2.18) can be applied to a general anharmonic potential. OMT diagrams are then evaluated in the good action-angle variables with numerically exact classical trajectories. This incorporates anharmonic effects into the OMT approximation as discussed in Chapter 3 and demonstrated in Chapters 4 and 5.

2.2 Multiple Degrees of Freedom

Within the quasiperiodic regime[56,57] where action-angle variables can be defined, the OMT approximation for one oscillator, presented in Sec. 2.1, can be extended to a collection of f coupled anharmonic vibrations described by the quantum mechanical Hamiltonian

$$\hat{H} = \sum_{i=1}^{f} \hat{H}_i^{\mathrm{HO}} + \sum_{i<j} c_{ij} \sqrt{m_i m_j}\, \omega_i \omega_j \hat{q}_i \hat{q}_j + V_{\mathrm{anh}}(\hat{\mathbf{q}}). \tag{2.19}$$

The harmonic Hamiltonian for local mode i with mass m_i and angular frequency ω_i is denoted $\hat{H}_i^{\mathrm{HO}}$. The second term in Eq. (2.19) defines bilinear coupling between the local modes and the third term contains all local mode anharmonicities and anharmonic couplings. By analogy to the $f = 1$ case, we construct OMT diagrams based on 2FDs in the harmonic limit which amounts to neglecting $V_{\mathrm{anh}}(\hat{\mathbf{q}})$ in Eq. (2.19). Normal mode coordinates $\{\hat{x}_j\}$ that are non-interacting within the harmonic approximation can then determined. The momentum operator for normal mode j is denoted $\hat{p}_j$. OMT diagrams can then be constructed from 2FDs evaluated within this harmonic approximation to the Hamiltonian in Eq. (2.19) in the outer product basis of the normal mode eigenstates.

The chromophore coordinate $\hat{q}_c$ in Eq. (1.10) may be written as a linear combination of normal modes,

$$\hat{q}_c = \sum_{i=1}^{f} \kappa_{ci} \hat{x}_i. \tag{2.20}$$

For example, if local mode a is taken to be the sole chromophore then $\hat{q}_c = \hat{q}_a$ and $\hat{q}_c = \sum_i \kappa_{ai} \hat{x}_i$, with κ_{ji} generally defined by the expansion $\hat{q}_j = \sum_i \kappa_{ji} \hat{x}_i$. Similarly, if the chromophore is described by a collective coordinate, $\hat{q}_c = \sum_j \lambda_{cj} \hat{q}_j$, with $\hat{q}_j$ local mode coordinates of the Hamiltonian, then the factors κ_{ci} in Eq. (2.20) are given by, $\kappa_{ci} = \sum_j \lambda_{cj} \kappa_{ji}$. A third possible model is to treat the normal modes as directly interacting with the electric field with relative strengths κ_{ci}. Generally, all of the coefficients $\{\kappa_{ci}\}_{i=1}^{f}$ may be nonzero, so that each radiation-matter interaction can excite or deexcite any of the f normal modes. Therefore, in evaluating both 2FDs and OMT diagrams the identity of the normal mode involved in each interaction must be allowed to vary.

If all f normal modes are non-negligibly coupled to the radiation, the four interactions in each 2FD generate f^4 combinations of normal mode interactions. If

we assume 2FDs not satisfying the trace in the harmonic limit contribute negligibility to the response function this number can be greatly reduced. To satisfy the trace in the harmonic limit it is necessary for an even number of interactions to occur with each interacting normal mode, therefore the $6f(f-1)(f-2)$ and $f(f-1)(f-2)(f-3)$ combinations of normal mode interactions involving three or four distinct normal modes, respectively, are excluded from the calculation. This criterion also dictates that sequences involving two modes must have two interactions with each mode, excluding an additional $4f(f-1)$ combinations. While having an even number of interactions with each mode is a necessary condition to satisfy the harmonic trace, it is not sufficient. Two of the six orderings of two modes each interacting twice with the electric field do not satisfy the trace in the harmonic limit for each phase-matched direction, eliminating $f(f-1)$ combinations of normal mode interactions. This non-trace-satisfying ordering corresponds to both interactions with each normal mode occurring with the same phase. For example, taking two interactions to be with mode r and two with mode s, and the interaction at time 0 to be with mode r, $rssr$ is a non-trace-satisfying ordering for the signal associated with wavevector $-\mathbf{k}_1+\mathbf{k}_2+\mathbf{k}_3$, since $\alpha=\delta=-$ and $\beta=\gamma=+$. Similarly, $rsrs$ is non-trace-satisfying for the signal associated with wavevector $\mathbf{k}_1-\mathbf{k}_2+\mathbf{k}_3$, and $rrss$ is non-trace-satisfying for $\mathbf{k}_1+\mathbf{k}_2-\mathbf{k}_3$. Therefore, of the f^4 possible sequences of interactions normal mode interactions only $2f^2-f$ satisfy the harmonic trace condition in each phase-matched direction, of which f possibilities involve all interactions with one mode and $2f(f-1)$ involve interactions with two distinct modes.

Figure 2.5 shows one pair of 2FDs corresponding to three of the trace allowed sequences of normal mode interactions in the $\mathbf{k}_\mathrm{I}$ phase-matched direction for a system described by two normal modes, 1 and 2. The remaining three possible normal

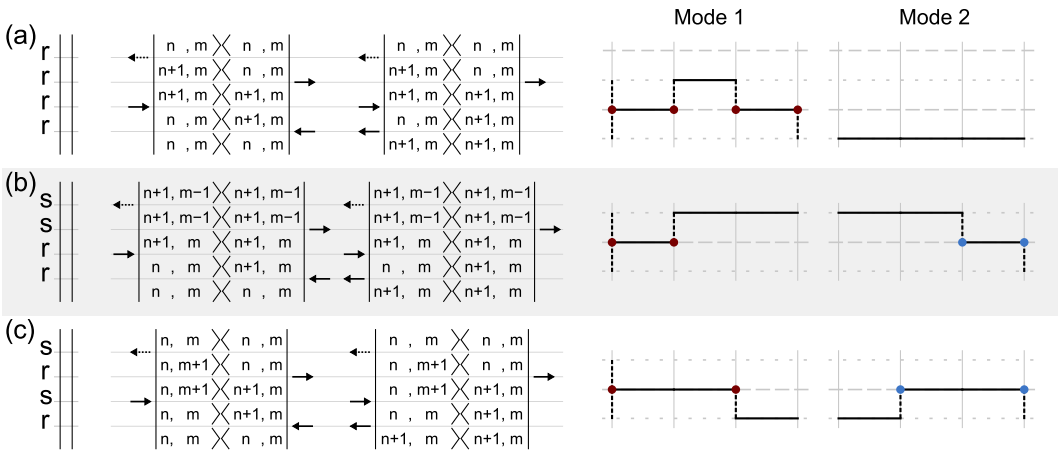

Figure 2.5: Pairs of 2FDs with different sequences of mode interactions contributing to the $\mathbf{k}_{\mathrm{I}}$ phase-matched direction are shown with their corresponding OMT diagrams. Diagrams are drawn to emphasize sequences of mode interactions for $f = 2$. All interactions occur with mode 1 in the diagrams in panel (a). Diagrams corresponding to the two trace-allowed orderings with two interacting modes with $\zeta_0 = 1$ are shown in (b) and (c), respectively.

mode sequences are obtained by switching the identities of modes r and s in each panel. For each sequence of normal mode interactions, $\boldsymbol{\zeta}$, we take the interacting mode at time 0, t_1, $t_1 + t_2$ and $t_1 + t_2 + t_3$ to be ζ_0, ζ_1, ζ_2, and ζ_3, respectively. For example in panel (a) $r = \zeta_0 = \zeta_1 = \zeta_2 = \zeta_3 = 1$, while in (b) $r = \zeta_0 = \zeta_1 = 1$ and $s = \zeta_2 = \zeta_3 = 2$. The 2FDs in Fig. 2.5 are drawn to emphasize the density operator time evolution with harmonic selection rules. The correspondence between the quantum and semiclassical diagrams is a straightforward generalization of the $f = 1$ case described in Section 2.1. In the harmonic limit, each normal mode evolves independently, so that the quantum evolution of the density operator $|n_{l1}, n_{l2}, \cdots\rangle\langle n_{r1}, n_{r2}, \cdots|$ is represented by a classical trajectory in which the action of each normal mode j is $(n_{lj} + n_{rj} + 1)\hbar/2$. An interaction with mode ζ causes an $\hbar/2$ jump in this mode's action, with all of the mode's angles and all other mode's actions held fixed. The four-point correlation function involves factors of $x_\tau^\zeta(t) + ip_\tau^\zeta(t)/(m_\zeta\omega_\zeta)$, with x and p the classical coordinate and momenta

corresponding to $\hat{x}$ and $\hat{p}$. These factors are evaluated at the action corresponding to the larger of the two quantum numbers being transitioned between, as for the single mode case.

In Fig. 2.5(a) 2FDs are shown with all interactions occurring with mode 1. This sequence of interactions corresponds to an initial increase or decrease in action of mode 1, followed by propagation for time t_1 at actions $J_1^1 = (n+1)\hbar\omega_1$ and $J_1^2 = (m+1/2)\hbar\omega_2$. Following this propagation, a second interaction with the field causes the action of mode 1 to increase by $\hbar/2$. The system is the propagated for time t_2 with $J_2^1 = (n+3/2)\hbar\omega_1$ and $J_2^2 = (m+1/2)\hbar\omega_2$. Then the action of mode 1 decreases by $\hbar/2$ at time $t_1 + t_2$, to $(n+1)\hbar\omega_1$, so that trajectory 3 is propagated with $J_3^1 = (n+1)\hbar\omega_1$ and $J_3^2 = (m+1/2)\hbar\omega_2$. The final interaction returns mode 1 to a population. These 2FDs correspond to the OMT diagram to the right in Fig. 2.5(a). This diagram consists of two fragments which correspond to the time evolution of mode 1 and mode 2. Because all of the interactions occur with mode 1, the action of mode 2 is continuous. Henceforth, fragments of OMT diagrams corresponding to modes not directly interacting with the field are not shown. The evaluation of the four-point correlation function is indicated by red dots along the mode 1 fragment of the OMT diagram. In panels (b) and (c) both modes interact with the field directly, so that both fragments in the OMT diagram have action jumps and are involved in the evaluation of the response function. Factors of $x_\tau^2(t) + ip_\tau^2(t)/(m_2\omega_2)$ evaluated in computing the response function are indicated by blue dots along the second trajectory fragment, which represents the evolution of mode 2.

The full OMT approximation to $R^{(3)}_{\gamma\beta\alpha}$ for f degrees of freedom is

$$R^{(3)}_{\gamma\beta\alpha}(t_3,t_2,t_1) = \sum_{r=1}^{f} \kappa_{cr}^4 \rho^r_{\gamma\beta\alpha}(t_3,t_2,t_1) + \sum_{r=1}^{f}\sum_{s\neq r} \kappa_{cr}^2\kappa_{cs}^2 \sum_{\boldsymbol{\zeta}} \rho^{\boldsymbol{\zeta}}_{\gamma\beta\alpha}(t_3,t_2,t_1). \quad (2.21)$$

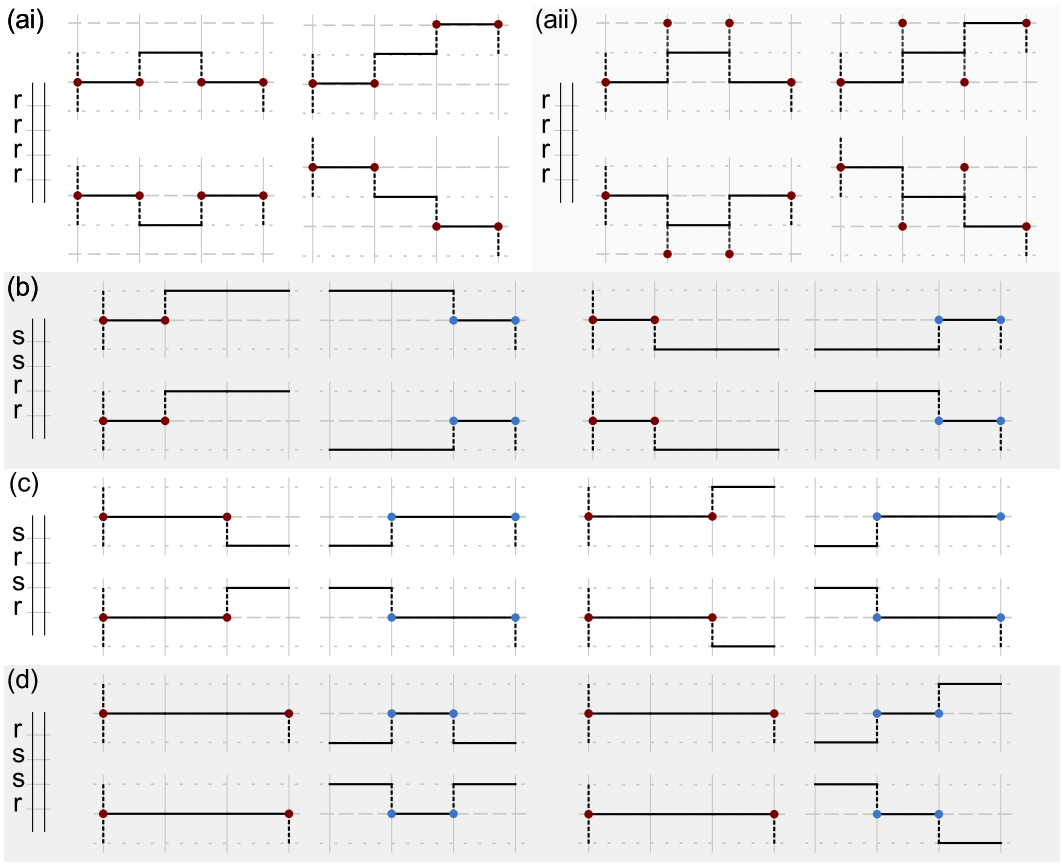

Figure 2.6: OMT diagrams for a general multidimensional system are shown. For each phase-matched direction either diagrams in panel (ai) or (aii) contribute. Additionally, two of the panels (b), (c) and (d) contribute. The time evolution of interacting modes are shown in each OMT diagram; all other modes are taken to evolve continuously in time.

This calculation is represented by the OMT diagrams in Fig. 2.6. The first sum in Eq. (2.21) contains contributions from diagrams with all interactions occurring with the same normal mode, r, such as the OMT diagrams in panels (ai) and (aii) of Fig. 2.6. The second sum in Eq. (2.21) contains contributions from OMT diagrams with interactions occurring with two normal modes, r and s, such as in panels (b)-(d) of Fig. 2.6. The label $\boldsymbol{\zeta}$ denotes the trace allowed sequences of interactions in each phase-matched direction, which are represented by two of the panels (b)-(d). In Fig. 2.6 all modes not interacting directly with the field are propagated at constant action equal to a half-odd-integer multiple of $\hbar$ for the

entire time interval $t_1 + t_2 + t_3$. The initial actions of all modes are independently varied so that the relative vertical positions of the red and blue OMT diagram fragments have no significance in Fig. 2.6. The contribution to Eq. (2.21) from processes in which all interactions occur with a single normal mode r is

$$\begin{aligned}
\rho^r_{\gamma\beta\alpha}(t_3,t_2,t_1) =& \frac{i}{2^4\hbar^{2f+3}}\sum_{d=1}^{4}\epsilon_d\int d\mathbf{z}_1\int d\mathbf{z}_2\int d\mathbf{z}_3\Delta F^r(\mathbf{z}_1)\Gamma^r(\mathbf{z}_1)\Delta^r_{1\sigma_d}\Delta^r_{2\sigma'_d} \\
&\times\delta(\boldsymbol{\phi}_2-\boldsymbol{\phi}_1(t_1))\delta(\boldsymbol{\phi}_3-\boldsymbol{\phi}_2(t_2))Q^r_\alpha(\mathbf{z}_1)Q^r_\beta(\mathbf{z}'_d)Q^r_\gamma(\mathbf{z}''_d)Q^r_\delta(\mathbf{z}_3(t_3)), \qquad (2.22)\\
\Delta F^r(\mathbf{z}_\tau) \equiv& F(\mathbf{z}_\tau)|_{J^r_\tau\to J^r_\tau-\hbar/2} - F(\mathbf{z}_\tau)|_{J^r_\tau\to J^r_\tau+\hbar/2}, \qquad (2.23)\\
F(\mathbf{z}_\tau) \equiv& \frac{e^{-\beta H(\mathbf{z}_\tau)}}{\int d\mathbf{z}' e^{-\beta H(\mathbf{z}')}\prod_{r=1}^{f}\sum_{n_r=0}^{\infty}\delta\left(J^r-(n_r+1/2)\,\hbar\right)} \qquad (2.24)\\
\Gamma^r(\mathbf{z}_\tau) \equiv& \hbar^f\sum_{n_r=1}^{\infty}\delta\left(J^r_\tau-n_r\hbar\right)\prod_{s\neq r}\sum_{n_s=0}^{\infty}\delta\left(J^s_\tau-(n_s+1/2)\,\hbar\right), \qquad (2.25)\\
\Delta^r_{\tau\pm} \equiv& \hbar^f\delta\left(J^r_{\tau+1}-(J^r_\tau\pm\hbar/2)\right)\prod_{s\neq r}\delta\left(J^s_{\tau+1}-J^s_\tau\right), \qquad (2.26)\\
Q^r_\pm(\mathbf{z}_\tau(t)) \equiv& x^r_\tau(t)\mp ip^r_\tau(t)/(m_r\omega_r). \qquad (2.27)
\end{aligned}$$

In Eq. (2.22), each contribution to the response function is expressed as an integration over three $2f$-dimensional phase space variables $\mathbf{z}_\tau$ with $\tau = 1, 2, 3$. In the OMT diagrams of Fig. 2.6 $\mathbf{z}_\tau$ represents the initial condition of the trajectory τ evolved for time t_τ. The index d labels the four semiclassical paths in which radiation interacts with a single mode, presented in Fig. 2.6(ai) and (aii). Whether the sum is over the diagrams in (ai) or (aii) is determined by the phase-matched direction as discussed in connection with Fig. 2.4 for $f = 1$. The factor Γ^r in Eq. (2.25) ensures the action of each mode is properly quantized following the first interaction with radiation. Mode r, which interacts with radiation at time 0, has an action J^r_1 quantized to an integral multiple of $\hbar$, while the other modes not interacting with radiation have actions quantized to a half-odd-integer multiple of $\hbar$. The factors $\delta(\boldsymbol{\phi}_j - \boldsymbol{\phi}_l)$ in Eq. (2.22) ensure that angle variables for each mode are unchanged

after each radiation-matter interaction, while the factors $\Delta^r_{\tau\pm}$ in Eq. (2.26) constrain the action of the mode interacting with radiation to increase or decrease by $\hbar/2$ after trajectory τ, with the action of all non-interacting modes unchanged. The statistical weight of each diagram is determined by the renormalized classical equilibrium distribution function, F in Eq. (2.32), the multimode generalization of the corresponding quantity in Eq. (2.5). This function is evaluated at the two states prior to the first interaction with the field. The actions of these states are obtained by replacing the interacting mode's action, J^r_1, in $\mathbf{J}_1$ with $J^r_1 \pm \hbar/2$ and the angle values are the same as after the first field interaction. The total weight is given by adding the contributions of these two terms as in Eq. (2.23), where the terms have opposite sign due to the innermost commutator in Eq. (1.10). In Eq. (2.22), ϵ_d is an overall sign arising from the remaining commutators. As for $f = 1$, for diagrams with the t_1 and $t_1 + t_2$ action jumps occurring with different sign, $\epsilon_d = -1$, while $\epsilon_d = 1$ for the diagrams with both jumps causing either an increase or decrease in action. The classical states $\mathbf{z}'_d$ and $\mathbf{z}''_d$ in Eq. (2.22) are determined by the diagram d, and are designated by the placement of the dots at times t_1 and $t_1 + t_2$ in each diagram. For example, in the first upper left path in Fig. 2.6(ai), $\mathbf{z}'_d = \mathbf{z}_1(t_1)$ and $\mathbf{z}''_d = \mathbf{z}_3$. For $f = 1$, Eq. (2.21) is represented by a single term of Eq. (2.22) which reduces to the expression for the third order response function in Eq. (2.18).

The expression in Eq. (2.21) also includes contributions from processes in which the radiation interacts twice with mode r (labeled red in Fig. 2.6) and twice with mode s (labeled blue in Fig. 2.6),

$$\rho^{\boldsymbol{\zeta}}_{\gamma\beta\alpha}(t_3,t_2,t_1) = \frac{i}{2^4\hbar^{2f+3}}\sum_{d=1}^{4}\epsilon_d\int d\mathbf{z}_1\int d\mathbf{z}_2\int d\mathbf{z}_3\Delta F^{\zeta_0}(\mathbf{z}_1)\Gamma^{\zeta_0}(\mathbf{z}_1)\Delta^{\zeta_1}_{1\sigma_d}\Delta^{\zeta_2}_{2\sigma'_d}$$
$$\times\,\delta(\boldsymbol{\phi}_2-\boldsymbol{\phi}_1(t_1))\delta(\boldsymbol{\phi}_3-\boldsymbol{\phi}_2(t_2))Q^{\zeta_0}_\alpha(\mathbf{z}_1)Q^{\zeta_1}_\beta(\mathbf{z}'_d)Q^{\zeta_2}_\gamma(\mathbf{z}''_d)Q^{\zeta_3}_\delta(\mathbf{z}_3(t_3)). \quad (2.28)$$

In the factors $\Delta_{j\sigma}^{\zeta_1}$ and $Q_{\sigma}^{\zeta_2}$ the identity of the mode ζ_τ interacting with radiation, r or s, is determined by the sequence of mode interactions, $\boldsymbol{\zeta}$. For example, in the second semiclassical path in panel (a) of Fig. 2.6, these path-dependent factors are $\Delta_{1+}^{r}\Delta_{2-}^{s}Q_{-}^{r}(\mathbf{z}_1)Q_{+}^{r}(\mathbf{z}_1(t_1))Q_{+}^{s}(\mathbf{z}_3)Q_{-}^{s}(\mathbf{z}_3(t_3))$. Equations (2.21)-(2.28) present the OMT approximation to the phase-matched third order vibrational response function for coupled vibrations.

As for a single degree of freedom, OMT diagrams in the multimode case are evaluated using classical trajectories for the full anharmonic Hamiltonian with quantization rules applied to the good action variables or approximations to these variables, thereby including anharmonic effects, as discussed in Chapter 3. This approach relies on each action variable being unambiguously associated with one normal mode. This is possible if the anharmonic couplings between normal modes in the full Hamiltonian are sufficiently small so that the transformation to good action-angle variables is well approximated by perturbation theory in anharmonicity,[56] as briefly reviewed in Appendix A. Double-sided Feynman diagrams, and therefore their corresponding OMT diagrams, can be associated with distinct physical processes. This aids in the interpretation of 2D spectra and allows for simplification of the OMT calculation of the response function for systems with multiple degrees of freedom when only certain physical processes or spectral peaks are of interest. The number of OMT diagrams may be reduced, for example, by neglecting diagrams with jumps in normal modes that are weakly coupled to the electric field as contributions from these diagrams to Eq. (2.21) scale as either κ_{cr}^2 or κ_{cr}^4.

2.2.1 OMT Approximation with Energy Transfer

The OMT diagrams in Fig. 2.6 are semiclassical representations of quantum 2FDs evaluated in a basis of stationary states so that coherence and population transfer processes are not included in the structure of the diagrams. These 2FDs correspond to OMT diagrams evaluated with quantized values of good action variables. In practice, OMT diagrams are evaluated numerically using perturbative corrections to the action variables of the normal modes. For some anharmonic couplings, the classical modes may exchange an appreciable amount of energy. This exchange of energy corresponds to quantum coherence or population transfer in quantum mechanical 2FDs. To allow for the inclusion of these processes, we enlarge the collection of 2FDs, and therefore the set of associated OMT diagrams, that contribute to the third order response function.

Consider the Hamiltonian in Eq. (2.19), consisting of two near-resonant local chromophore modes a and b coupled to a bath of N_{B} low frequency local bath modes. Suppressing anharmonicity in the local mode Hamiltonians $\hat{H}_a$ and $\hat{H}_b$ allows the construction of $f = N_{\mathrm{B}} + 2$ normal modes with coordinates denoted $\hat{x}_j$. For an off-resonant bath, two normal modes are dominated by contributions from the local chromophore modes, with the remaining normal modes representing perturbed bath modes. We label the chromophore normal modes 1 and 2, with labels 3, ..., f referring to bath normal modes. These normal modes are coupled by anharmonic terms in $\hat{H}_a$ and $\hat{H}_b$. For certain anharmonic couplings, 2FDs evaluated in this normal mode basis may show appreciable non-stationary state behavior.

Taking both normal modes 1 and 2 to interact with the electric field, 2FDs with coherence and population-coherence transfer that may contribute to the rephas-

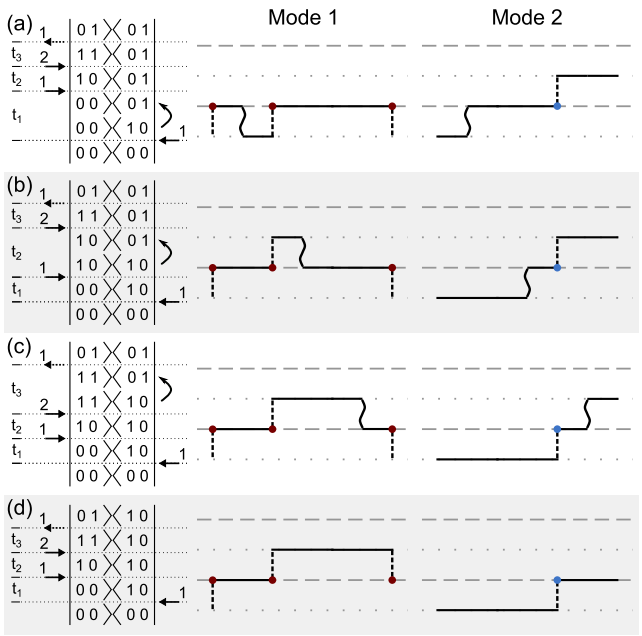

Figure 2.7: At left trace-satisfying 2FDs are shown with coherence transfer occurring during the t_1, t_2 and t_3 time periods in panels (a)-(c), respectively. Corresponding OMT diagrams are shown at right. These form a subset of the possible 'child' diagrams that can be generated from the non-trace-satisfying 'parent' diagram in (d) with all-forward time propagation.

ing signal for such a system are shown in Figs. 2.7(a)-(c). For clarity the bath mode quantum numbers are not specified and all 2FDs shown begin with both chromophore modes in the ground state. However, the OMT diagram shown to the right in each panel corresponds to a pair of 2FDs starting in a general initial state, as in previous sections. The OMT diagrams in Fig. 2.7 are obtained from 2FDs by applying the same rules used to generate the diagrams in Fig. 2.6 with the additional wavy vertical lines representing nonradiative energy transfer processes. Since the bath is assumed to be off-resonant, an increase in the energy of one chromophore mode is accompanied by a decrease in energy of the other chromophore. For example, in the 2FD in Fig. 2.7(a), at the start of the t_1 propagation period, mode 1 is in the coherence $|0\rangle\langle 1|$ and mode 2 is in the population $|0\rangle\langle 0|$, while by the end of this period, mode 1 is in the population $|0\rangle\langle 0|$ and mode 2 is in the

coherence $|0\rangle\langle 1|$. In the corresponding OMT diagram in Fig. 2.7(a), this coherence transfer process is represented by the transfer of energy between two classical oscillators during the t_1 period. The action of mode 1 decreases by $\hbar/2$ and the action of mode 2 increases by this amount. In the general case, energy can be exchanged between any two oscillators in the system, including those not interacting with the radiation in a given diagram. The 2FDs in Figs. 2.7(b) and 2.7(c) include similar population-coherence and coherence transfer processes during the t_2 and t_3 propagation periods, respectively, and these processes are represented in the associated semiclassical diagrams as energy transfer between classical oscillators during the appropriate time intervals. The 2FDs in Figs. 2.7(a)-(c) are trace-satisfying and hence contribute to the response function, as should the corresponding OMT diagrams.

The diagrams in Fig. 2.7(a)-(c) cannot be directly incorporated into the OMT calculation since these diagrams are generated numerically only if specific dynamical processes occur. The inclusion of OMT diagrams such as those in Figs. 2.7(a)-(c) is instead based on consideration of non-trace-satisfying 'parent' diagrams that do not explicitly include energy transfer processes, such as the diagram in Fig. 2.7(d). The 2FD in Fig. 2.7(d) does not satisfy the trace and hence does not contribute to $R^{(3)}$. The OMT diagram in Fig. 2.7(d), if evaluated in the harmonic limit, would similarly vanish as a consequence of integration over angle variables. However, if in evaluating the OMT diagram in Fig. 2.7(d) mode 1 were found to have transferred energy to mode 2 during the t_1 evolution period, the result would be the sequence of events represented by the OMT diagram in 2.7(a). Similarly, energy transfer between modes 1 and 2 during the t_2 or t_3 trajectories in the OMT diagram in Fig. 2.7(d) would yield the diagrams in Figs. 2.7(b) and 2.7(c), respectively. We will refer to the diagrams in Figs. 2.7(a)-(c) as 'child' diagrams of

the parent in Fig. 2.7(d). Including the diagram in Fig. 2.7(d) incorporates the processes shown in diagrams 2.7(a)-(c) into the OMT calculation through the use of full classical dynamics. The importance of processes such as those represented by the OMT diagrams in Figs. 2.7(a)-(c) to the response function is entirely determined by the extent to which the numerical classical trajectories of the coupled chromophores exhibit these processes.

For systems with energy transfer, the response function should be computed from all parent OMT diagrams generated from Eq. (1.10), including non-trace-satisfying diagrams excluded from the response function calculation in Eq. (2.21). This can be achieved by modifying the OMT approximation to the response function in Eq. (2.21) to include contributions from any sequence of normal mode interactions,

$$R^{(3)}_{\gamma\beta\alpha}(t_3,t_2,t_1) \;=\; \sum_{r_j=1,\ldots,f} \kappa_{cr_0}\kappa_{cr_1}\kappa_{cr_2}\kappa_{cr_3}\rho^{r_0,r_1,r_2,r_3}_{\gamma\beta\alpha}(t_3,t_2,t_1). \tag{2.29}$$

The indices r_0, r_1, r_2 and r_3 specify the normal mode interacting with the field at time 0, t_1, t_1+t_2 and $t_1+t_2+t_3$, respectively. These indices are used rather than summing over $\boldsymbol{\zeta}$ as in Eq. (2.21) to emphasize that all possible combinations of normal mode interactions are included in Eq. (2.29), not just trace-satisfying combinations. For a general f-dimensional system there are therefore f^4 terms contributing to Eq. (2.29). The contribution from a given sequence of normal mode interactions is,

$$\rho^{r_0,r_1,r_2,r_3}_{\gamma\beta\alpha}(t_3,t_2,t_1) = \frac{i}{2^4\hbar^{2f+3}}\sum_{d=1}^{4}\epsilon_d\int d\mathbf{z}_1\int d\mathbf{z}_2\int d\mathbf{z}_3\Delta F^{r_0}(\mathbf{z}_1)\Gamma^{r_0}(\mathbf{z}_1)\Delta^{r_1}_{1\sigma_d}\Delta^{r_2}_{2\sigma'_d}$$

$$\times\,\delta(\boldsymbol{\phi}_2-\boldsymbol{\phi}_1(t_1))\delta(\boldsymbol{\phi}_3-\boldsymbol{\phi}_2(t_2))Q^{r_0}_{\alpha}(\mathbf{z}_1)Q^{r_1}_{\beta}(\mathbf{z}'_d)Q^{r_2}_{\gamma}(\mathbf{z}''_d)Q^{r_3}_{\delta}(\mathbf{z}'''_d), \tag{2.30}$$

$$\Delta F^{r}(\mathbf{z}) \equiv F(\mathbf{z})|_{J^r\rightarrow J^r-\hbar/2} - F(\mathbf{z})|_{J^r\rightarrow J^r+\hbar/2}, \tag{2.31}$$

$$F(\mathbf{z}) \equiv \frac{e^{-\beta H(\mathbf{z})}}{\int d\mathbf{z}' e^{-\beta H(\mathbf{z}')}\prod_{s=1}^{f}\sum_{n_s=0}^{\infty}\hbar\delta\left(J^s-\left(n_s+\frac{1}{2}\right)\hbar\right)}, \tag{2.32}$$

$$\Gamma^r(\mathbf{z}) \equiv \hbar^f \sum_{n_r=1}^{\infty} \delta\left(J^r - n_r\hbar\right) \prod_{s\neq r} \sum_{n_s=0}^{\infty} \delta\left(J^s - \left(n_s + \tfrac{1}{2}\right)\hbar\right), \tag{2.33}$$

$$\Delta^r_{\tau\pm} \equiv \hbar^f \delta\left(J^r_{\tau+1} - \left(J^r_\tau(t_\tau) \pm \tfrac{\hbar}{2}\right)\right) \prod_{s\neq r} \delta\left(J^s_{\tau+1} - J^s_\tau(t_\tau)\right), \tag{2.34}$$

$$Q^r_\pm(\mathbf{z}_\tau(t)) \equiv x^r_\tau(t) \mp i p^r_\tau(t)/(m_r\omega_r). \tag{2.35}$$

The index d in Eq. (2.30) sums over semiclassical diagrams with four parent diagrams contributing to each term, corresponding to combinations of either increasing or decreasing the action at the second and third interactions with the field. Only combinations of these two interactions are considered since both initial interactions are included in a single diagram through the factor ΔF^{r_0} defined in Eq. (2.31), as discussed in connection with Eq. (2.23) in Sec. 2.2. Therefore, up to $4f^4$ parent diagrams may contribute to Eq. (2.29). In Eq. (2.30) ϵ_d is an overall sign arising from the remaining commutators, determined as discussed in connection with Eq. (2.22) in Sec. 3.3. The action of mode r is increased or decreased following trajectory τ in the OMT path according to the subscripts σ in $\Delta^r_{\tau\sigma}$, which can be either $+$ or $-$, as defined in Eq. (2.34). Unlike in the corresponding factor without energy transfer, defined in Eq. (2.26), in Eq. (2.34) the final action values of each trajectory are explicitly given as functions of time, since the assumption that these actions are fixed has been relaxed. The arguments of Q^r_σ in Eq. (2.30) determine the four phase space points in the path required to compute the response function chosen according to the procedure described in Secs. 2.1 and 2.2. The arguments of these factors are determined not only by the parent diagram d, but also by the specific dynamical processes that occur during time propagation. For example, the parent diagram in Fig. 2.7(d) indicates the evaluation, $Q^1_-(\mathbf{z}_1)Q^1_+(\mathbf{z}_1(t_1))Q^2_+(\mathbf{z}_3)Q^1_-(\mathbf{z}_3(t_3)|_{J^1_3\to J^1_3-\hbar/2})$, while its child diagram with energy transfer during the t_1 time period in Fig. 2.7(a), indicates the alternative evaluation, $Q^1_-(\mathbf{z}_1)Q^1_+(\mathbf{z}_2)Q^2_+(\mathbf{z}_2(t_2))Q^1_-(\mathbf{z}_3(t_3))$.

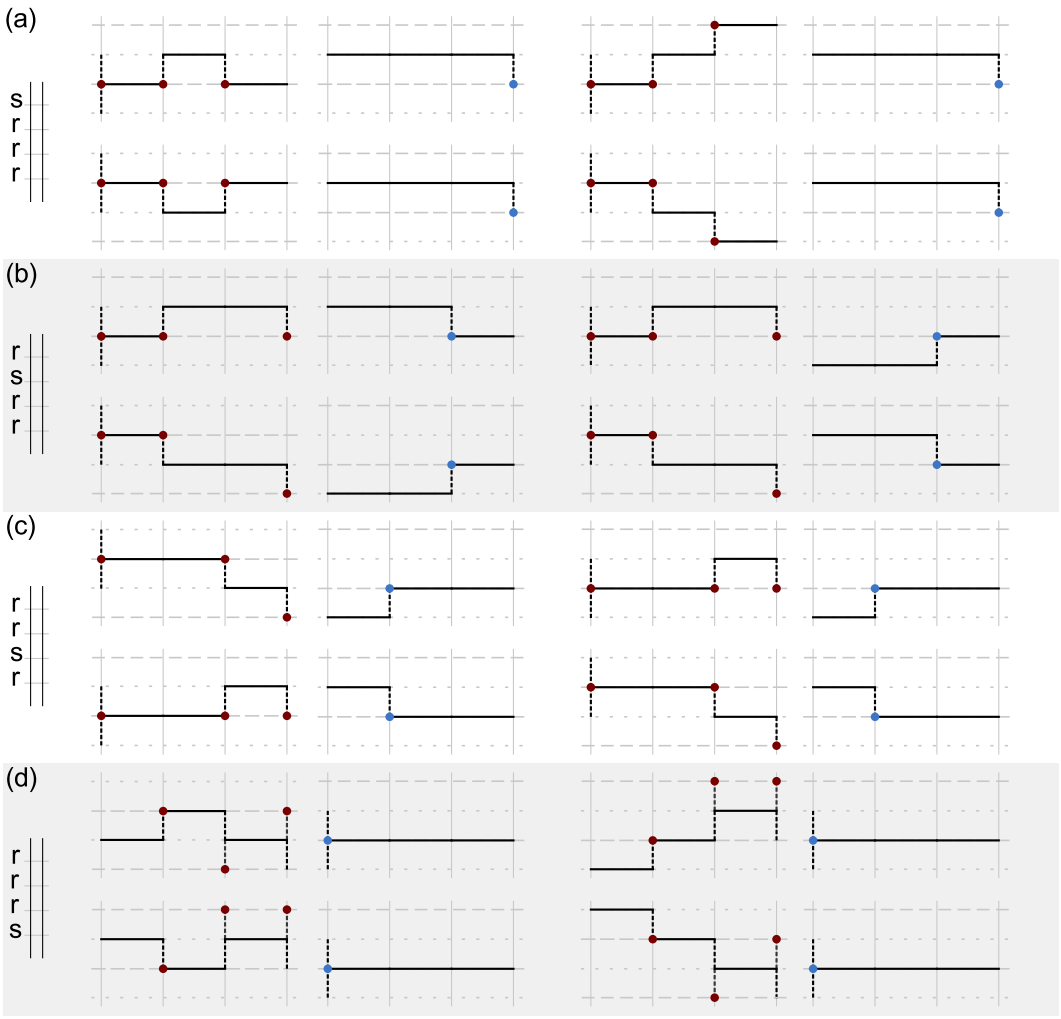

Figure 2.8: Non-trace-satisfying OMT diagrams are shown that contribute in the $\mathbf{k}_{\mathrm{I}}$ phase-matched direction with three interactions with mode r and one with mode s. These diagrams only contribute non-negligibly through anharmonic effects.

Contributions from all of the diagrams shown in Fig. 2.6 panels (b)-(d) are calculated in Eq. (2.29), including contributions from the non-trace-satisfying sequence of normal mode interactions for each phase-matched direction. Additionally, diagrams with more than two interacting modes or an odd number of interactions with each mode are included in Eq. (2.29). Figure 2.8 shows the non-trace-satisfying OMT parent diagrams contributing in the $\mathbf{k}_{\mathrm{I}}$ phase-matched direction with three interactions with mode r and one with mode s. As these diagrams do not satisfy the trace in the harmonic limit, it is not necessary for all diagram

fragments to end on a dotted horizontal line, corresponding to a half-odd-integer multiple of $\hbar$. For some non-trace-satisfying diagrams there is ambiguity in the action at which Q_δ is evaluated according to the rules in Sec. 2.2. For example, the upper leftmost diagram in Fig. 2.8(d) represents the evolution of the density operator $|n+1\rangle\langle n-1|$ during the t_3 time interval for mode r, so that if the final interaction with the field occurs with the ket aspect of the density operator the states $n+1$ and n will be transitioned between in this interaction. However, if the last interaction occurs with the bra aspect of the density operator the states $n-1$ and n will be transitioned between. Therefore it is ambiguous whether the factor Q_δ should be evaluated at action $J_3^r - \hbar/2$ or at action $J_3^r + \hbar/2$, as indicated in Fig. 2.8(d). This ambiguity arises because the cyclic invariance of the trace holds in the harmonic limit irrespective of this choice, as the angle average causes these diagrams to have zero contribution to the response function in the harmonic limit. If an energy transfer event generates a trace-satisfying child diagram then evaluation of the correlation function should, in principle, be dictated by the corresponding 2FDs with the appropriate coherence or population transfer event, not by the 2FDs corresponding to the parent diagram. Therefore, the choice of argument for Q_δ in the parent diagram will not dictate the evaluation of its child diagrams. In practice, this can complicate the calculation of the OMT approximation with energy transfer as discussed in Chapter 3. As this choice does not change the result of evaluating either the parent or child OMT diagrams in the harmonic limit, we choose to derive all OMT diagrams assuming that the final field interaction causes a deexcitation of the ket aspect of the density operator.

OMT diagrams contributing to the signal associated with wavevector $\mathbf{k}_{\mathrm{II}}$, with the same sequences of normal mode interactions as Fig. 2.8, are shown in Fig. 2.9. Unlike the trace-satisfying diagrams contributing to Eq. (2.21) non-trace-satisfying

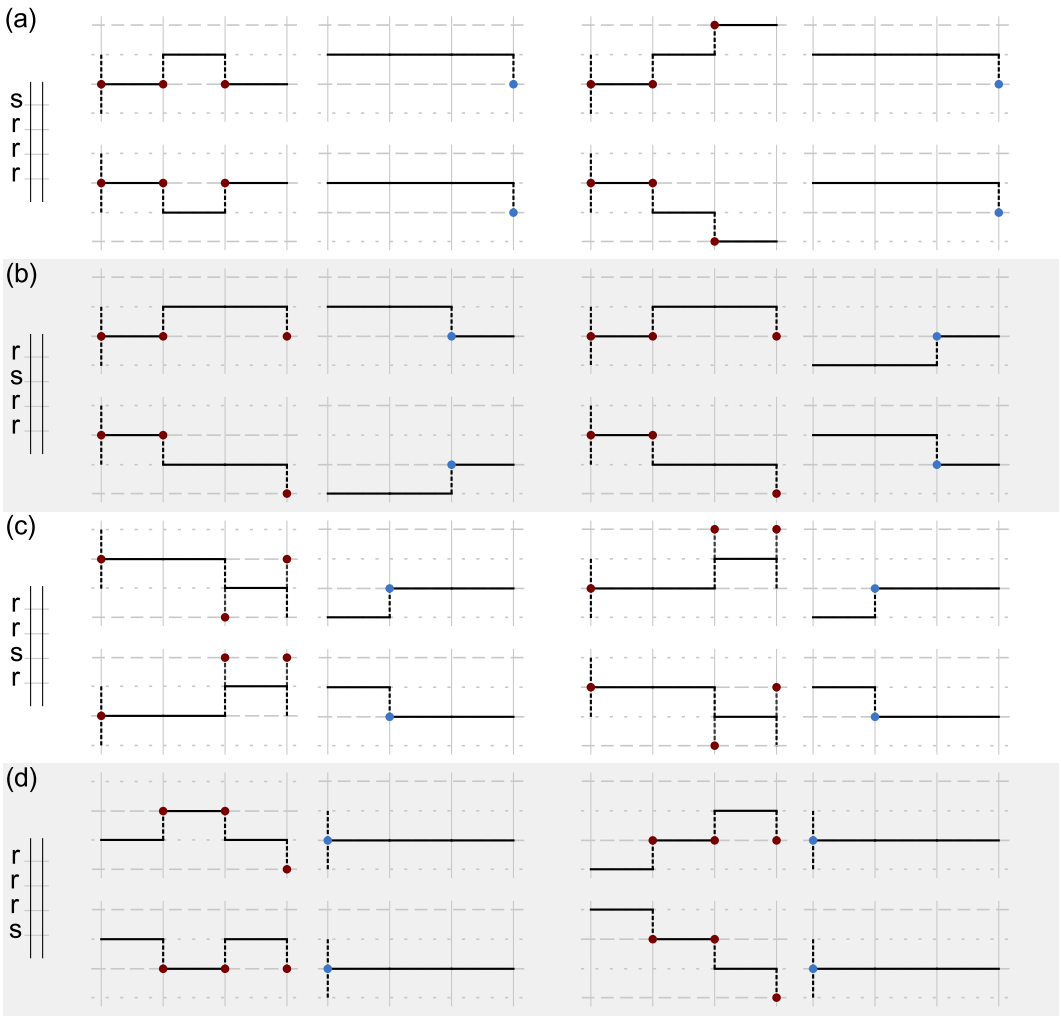

Figure 2.9: Non-trace-satisfying OMT diagrams are shown that contribute in the $\mathbf{k}_{\mathrm{II}}$ phase-matched direction with three interactions with mode r and one with mode s.

diagrams contributing to the $\mathbf{k}_{\mathrm{I}}$ and $\mathbf{k}_{\mathrm{II}}$ signals can represent the dynamics of two-quantum coherences. These diagrams are characterized by factors of Q_σ being evaluated at action values not associated with the underlying path. For three interactions with mode r and one with mode s, the $srrr$ sequence of normal mode interactions in Fig. 2.8(d), for example, represents the evolution of a two-quantum coherence for mode r during the t_3 time period. Similarly, the $rrsr$ sequence of normal mode interactions in Fig. 2.9(c) represents the evolution of a two-quantum coherence during the t_3 time period for mode r. Figures 2.8 and 2.9 also demon-

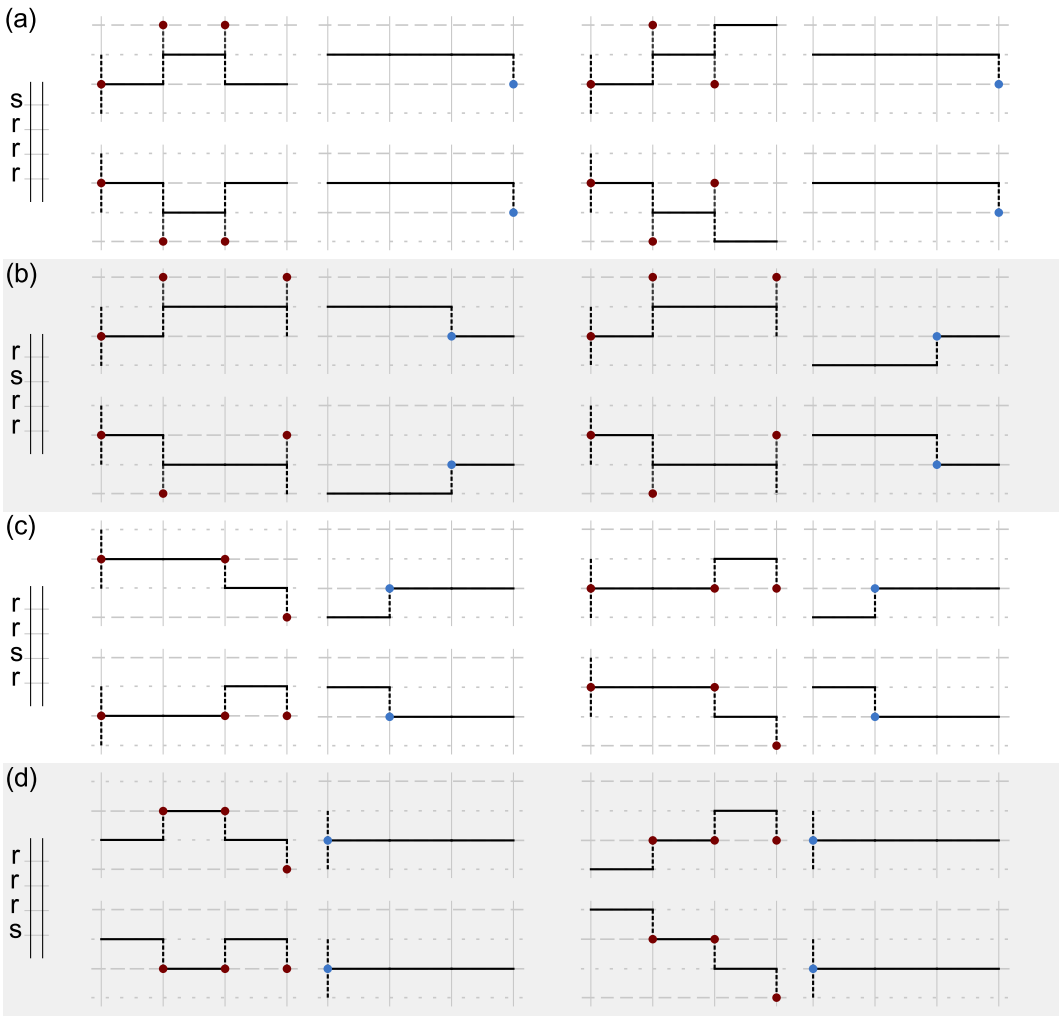

Figure 2.10: Non-trace-satisfying OMT diagrams contributing to Eq. (2.29) in the $\mathbf{k}_{\mathrm{III}}$ phase-matched direction with three interactions with mode r and one with mode s are shown.

strate that the four-point-correlation functions encoded by non-trace-satisfying OMT diagrams contributing to the $\mathbf{k}_{\mathrm{I}}$ and $\mathbf{k}_{\mathrm{II}}$ signals are not evaluated at the same actions for all sequences of interactions.

Non-trace-satisfying parent diagrams contributing to the signal associated with the $\mathbf{k}_{\mathrm{III}}$ wavevector for these sequences of normal mode interactions are shown in Fig. 2.10. Non-trace-satisfying diagrams in this phase-matched direction can also represent the evolution of two-quantum coherences. In Fig. 2.10(a) and (b), the

OMT diagrams represent an evolution of a two-quantum coherence in mode r during the t_2 and both the t_2 and t_3 time periods, respectively. The diagrams shown in Figs. 2.8–2.10 are the additional diagrams contributing to the response function calculation in Eq. (2.29) with three interactions with one normal mode and the fourth with a distinct mode. Generally, this is only a subset of the non-trace-satisfying diagrams contributing to Eq. (2.29), as up to four distinct modes may interact with the field in a given OMT diagram. This set of diagrams demonstrates that the evaluation of the Q_σ factors is more complicated in non-trace-satisfying diagrams than in the trace-satisfying diagrams shown in Fig. 2.6. When energy transfer occurs, so that the parent diagrams in Figs. 2.8–2.10 may appreciably contribute to the system response, the evaluation of these factors should vary, as in Fig. 2.7, which further complicates the diagrams evaluation and leads to inherent ambiguities in the "correct" evaluation points, as discussed in the implementation details in Sec. 3.4.

Chapter 3

Implementations of the OMT

Implementing the OMT approximation presented in Chapter 2 can be computationally demanding. If naively implemented the number of trajectory propagations required for a single OMT diagram scales as $n_{t_1}(1+n_{t_2})$ where n_t is the number of response function values calculated during the t-time interval. This scaling arises because, for each diagram, a single t_1 trajectory is numerically propagated from initial action-angle variables $\mathbf{J}_1$ and $\boldsymbol{\phi}_1$. Then, for each t_1 value, a trajectory with initial actions $\mathbf{J}_2$ and angles $\boldsymbol{\phi}_2 = \boldsymbol{\phi}_1(t_1)$ is propagated, resulting in n_{t_1} propagations. Finally, for each t_1 and t_2 value a t_3 trajectory is propagated, resulting in $n_{t_1}n_{t_2}$ propagations. Similarly, the number of constant-angle action jumps computed for a single diagram scales as $n_{t_1}(1+n_{t_2})$. For a single degree of freedom, a phase-matched contribution to the response function is given by Eq. (2.18), which includes a numerical average over the initial action and angle and corresponds to the evaluation of one of the sets of four OMT diagrams in Fig. 2.4. This calculation becomes more challenging for systems with multiple degrees of freedom, as both the dimensionality of the phase space average and the number of OMT diagrams per initial condition may increase, as seen in Eqs. (2.21) and (2.29).

There are three primary numerical challenges associated with implementing the OMT approximation. First, classical trajectories with specified action values must be determined. Each horizontal solid line in an OMT diagram represents one of these quantized classical trajectories. Second, discrete jumps in action must be carried out at constant angle values. Each vertical dashed line in an OMT diagram represents one such transition. Third, a $2f$-dimensional average over the initial phase space distribution must be performed as an f-dimensional sum over action

variables and an f-dimensional integration over initial angles. These calculations must be computed efficiently as, if all modes interact with the field, the number of thermally averaged OMT diagrams scales with f either as $8f^2 - 4f$ in Eq. (2.21) or as $4f^4$ when including all possible energy transfer contributions in Eq. (2.29).

A numerically exact fixed-trajectory (NEFT) implementation is described in Sec. 3.1 for a single high frequency degree of freedom. This implementation achieves a higher efficiency than the naive implementation by taking advantage of analytic properties of action-angle variables. For multidimensional systems this implementation is generally not practical, but can be used as a framework for developing more tractable implementations. In Secs. 3.2 and 3.3 two approximate implementations are presented that maintain some of the desirable properties of the NEFT implementation while being practical for different types of multimode systems. For systems containing a few high frequency oscillators the fixed-trajectory (FT) method, described in Sec. 3.2, can be applied. This approach is highly efficient and requires the minimum number of trajectory propagations, but breaks down for systems that include disparate frequency scales or many degrees of freedom. The forward-backward (FB) implementation can be applied to these types of systems, as presented in Sec. 3.3. Modifications to the FB implementation that allow for energy transfer processes to contribute to the system response are presented Sec. 3.4.

3.1 Numerically Exact Fixed-Trajectory Implementation

In this section, the three numerical challenges associated with implementing the OMT approximation are discussed in the context of computing the third order response function for a single degree of freedom. An implementation of the OMT

that is significantly more efficient than the naive implementation is presented. This numerically exact fixed-trajectory implementation (NEFT) takes advantage of properties of the action-angle variables to achieve this high efficiency. Therefore, before presenting the details of the NEFT implementation, the relevant features of action-angle variables are briefly reviewed.

In general, action and angle variables, $\mathbf{J}$ and $\boldsymbol{\phi}$, result from a canonical transformation of the Cartesian coordinates and their conjugate momenta, $\mathbf{q}$ and $\mathbf{p}$, such that the resulting transformed Hamiltonian is a function of the actions alone.[55] We restrict our discussion here to a one-dimensional system, for which such variables are guaranteed to exist. The properties discussed generalize when action-angle variables can be defined for a multidimensional system.

By construction, the transformed one-dimensional Hamiltonian H is a function of the action alone, so that the action J is a constant of the motion. Therefore, the angle evolves linearly in time,

$$\phi(t) = \omega(J)t + \phi_\circ. \tag{3.1}$$

Here $\omega(J) \equiv \partial H/\partial J$ is the frequency of the oscillation and $\phi_\circ$ is the initial angle of the oscillator. The action variable can be determined in terms of the Cartesian coordinate and momenta as an integration over one period of this oscillation,

$$J = \frac{1}{2\pi} \oint p(t)\dot{q}(t)dt. \tag{3.2}$$

Because the oscillator's evolution is confined to a well defined periodic trajectory for each action value, computing $n_{t_1}(1 + n_{t_2})$ trajectory propagations for each OMT diagram is unnecessary. Rather than propagating a distinct trajectory for each segment of an OMT diagram, the periodic trajectories corresponding to the required quantized action values can be computed once at the start of the calculation. These precomputed trajectories can then be reused to determine the time

evolution of each appropriate segment of an OMT diagram. For a single degree of freedom, these fixed trajectories can be determined by numerically searching for initial coordinate and momentum values that satisfy Eq. (3.2) for the desired action value when $q(t)$ and $p(t)$ are propagated according to Hamilton's equations of motion. The origin of the angle value is arbitrary but must be consistently maintained for all trajectories. For convenience we start trajectories at $\phi_\circ = 0$ for all actions with $p(0) = 0$ and $q(0) > 0$. Therefore, in the NEFT implementation, the number of time propagations is only dependent on the number of action values used in the phase space average, not on the number of time values at which the response function is evaluated.

The second numerical challenge in applying the OMT approximation is to link these propagated classical trajectories by transitions at constant angle. The angle $\phi(t)$, evolves linearly in time according to Eq. (3.1). Therefore, the frequency $\omega(J)$ can be calculated from the numerically determined period of oscillation, $T(J)$, as $\omega(J) = 2\pi/T(J)$. A constant angle transition from a trajectory at action J_i at time τ to a trajectory at action J_f can be completed using the frequencies associated with these trajectories. The angle at time τ in a trajectory at action J_i with initial angle, $\phi_\circ = 0$ is given by $\phi(\tau) = \omega(J_i)\tau$. This angle corresponds to time, $\tau' = \frac{\omega(J_i)\tau}{\omega(J_f)}$ in the final trajectory at action J_f, similarly with initial angle 0. Because the trajectories are periodic we are free to take the times τ and τ' modulo the periods $T(J_i)$ and $T(J_f)$, respectively. Computing a constant angle transition is therefore trivial given the precomputed closed trajectories and their associated frequencies.

The final challenge to computing the vibrational response function in the OMT approximation is the phase space average. The delta functions in Eq. (2.18) re-

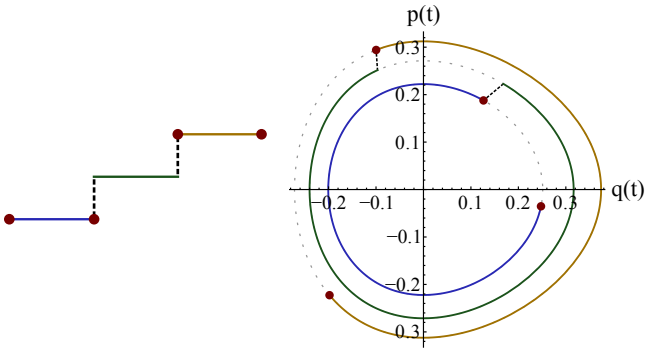

Figure 3.1: An OMT diagram and a schematic corresponding to its evaluation in phase space for a Morse oscillator is shown for one initial condition and set of propagation times. Gray dotted lines show precalculated fixed trajectories at actions $\hbar$, $3\hbar/2$, and $2\hbar$. Colored solid lines represent the evolution of the trajectories for times t'_j, the propagation times modulo $T(J_j)$. Red dots indicate phase space points where factors of Q_σ are evaluated.

duce the OMT calculation for a single degree of freedom to a sum over the action J_1 and an integration over the initial angle ϕ_1. The number of terms required to converge the sum over J_1 is controlled by the difference of the renormalized classical distributions in Eq. (2.18). If $\beta\hbar\omega \gtrapprox 1$ a few terms will suffice to accurately reproduce the system response. The response function can then be determined by performing a numeric integration over the initial angle, which can be translated into a numeric integration over the initial time in the precomputed trajectory corresponding to the first segment of each OMT path. In the quasiharmonic approximation of Eq. (2.10), the integrand of Eq. (2.18) is independent of ϕ_1. This can be seen, for example, from Eq. (2.11), in which the angle differences $\phi_1(t_1) - \phi_1$ and $\phi_3(t_3) - \phi_3$ are independent of initial angle ϕ_1. In practice this means that relatively few evaluations are needed to converge this integral.

Figure 3.1 shows an OMT diagram and a schematic of its evaluation in phase space for one set of initial conditions and propagation times t_1, t_2, and t_3. The OMT diagram begins with propagating a trajectory at action J_1 for time t_1. Then a constant angle jump transitions the oscillator to action $J_1 + \hbar/2$ and the system

is propagated for time t_2 starting from the initial angle $\phi_1(t_1)$. A second constant angle jump increases the oscillator's action to $J_1+\hbar$ and a trajectory is propagated for time t_3 from the initial angle $\phi_2(t_2)$. To evaluate the contribution to the system response from this diagram for $J_1 = \hbar$ using the NEFT implementation three classical trajectories are precalculated corresponding to actions $\hbar$, $3\hbar/2$, and $2\hbar$. The three precalculated trajectories are shown as dotted gray lines in Fig. 3.1 for a Morse oscillator with potential $D\left(1-e^{-\xi q}\right)^2$. The coordinate and momentum plotted in Fig. 3.1 are made dimensionless as ξq and $\xi p/m\omega$ with mass m and harmonic frequency ω. The propagation times t_1, t_2, and t_3 are taken modulo the period of the appropriate trajectory, $T(\hbar)$, $T(3\hbar/2)$, and $T(2\hbar)$ respectively, so that the resulting evolution times t'_j are between 0 and the period of the oscillator at the appropriate action. The system response for the OMT diagram in Fig. 3.1 is computed from a four-point correlation function consisting of the values $Q_\alpha(z_1)$, $Q_\beta(z_1(t_1))$, $Q_\gamma(z_3)$ and $Q_\delta(z_3(t_3))$, defined in Eq. (2.9), as indicated by red dots in Fig. 3.1. Given precalculated trajectories with known frequencies, the values $Q_\alpha(z_1)$ and $Q_\beta(z_1(t_1))$ evaluated during the first propagation time, shown in blue, can be calculated. The initial angle ϕ_1 can be converted to a time on the J_1 trajectory using Eq. (3.1) and this time can be added to t'_1 (modulo $T(\hbar)$) to give the two times on the fixed-trajectory for these evaluations. The remaining two correlation points can be calculated by propagating the diagram through the two constant angle jumps. During the action jump at t_1 the angle is given by converting the time used to evaluate $Q_\beta(z_1(t_1))$ to an angle using Eq. (3.1). Propagation during t_2 can be determined by converting this angle to a time in the $3\hbar/2$ trajectory and adding this result to t'_2, taking the resulting time modulo $T(3\hbar/2)$. The second jump can be similarly carried out using Eq. (3.1) and finally, the procedure used to compute $Q_\alpha(z_1)$ and $Q_\beta(z_1(t_1))$ can be used to evaluate $Q_\gamma(z_3)$ and $Q_\delta(z_3(t_3))$.

The system response contributions from these linked classical trajectories must be determined while varying the initial action and angle, with each initial condition being weighted by a difference of renormalized classical thermal distributions, as given in Eq. (2.18). The energies $H(J)$ can be determined numerically using the untransformed Hamiltonian and the precomputed fixed trajectories.

3.2 Fixed-Trajectory Implementation

For systems with multiple degrees of freedom it is difficult to compute trajectories in the good action-angle variables to numerical precision, even in the quasiperiodic regime where action-angle variables can be defined. Therefore, the NEFT implementation, which relies heavily on the action-angle variable formalism, cannot be applied to multidimensional systems as presented in Sec. 3.1. A fixed-trajectory implementation has been developed that efficiently computes the OMT approximation to the response function by maintaining several desirable features of the NEFT calculation while making the modifications necessary to treat systems consisting of a few high frequency modes.

Trajectories with quantized good action values can be approximated using perturbation theory in anharmonicity, as presented in Ref. 56. The central object in this approach is a type 2 generating function[55] associated with the canonical transformation from zeroth-order action and angle variables $(\mathbf{I}, \boldsymbol{\theta})$ to good variables $(\mathbf{J}, \boldsymbol{\phi})$. The zeroth-order variables are correct for the harmonic classical Hamiltonian corresponding to the quantum Hamiltonian in Eq. (2.19) with $V_{\mathrm{anh}}(\hat{\mathbf{q}}) = 0$. The generating function, which is a function of $\mathbf{J}$ and $\boldsymbol{\theta}$, is expanded in a Fourier series in $\boldsymbol{\theta}$ and the Fourier coefficients are determined perturbatively to the desired

order in anharmonicity. This procedure results in expressions for the coordinates and momenta of each normal mode, r, as functions of good actions and harmonic angles, $x^r(\mathbf{J}, \boldsymbol{\theta})$ and $p^r(\mathbf{J}, \boldsymbol{\theta})$. The focus of Ref. 56 is on calculating semiclassical energies, which does not require expressing the harmonic angle variables $\boldsymbol{\theta}$ in terms of $\mathbf{J}$ and $\boldsymbol{\phi}$. To approximate the normal mode coordinates and momenta as $x^r(\mathbf{J}, \boldsymbol{\phi})$ and $p^r(\mathbf{J}, \boldsymbol{\phi})$ these expressions are needed. Differentiating the generating function with respect to the good action variables yields $\boldsymbol{\phi}$ as a function of $\mathbf{J}$ and $\boldsymbol{\theta}$. Inverting these equations to the appropriate order yields $\boldsymbol{\theta}(\mathbf{J}, \boldsymbol{\phi})$, so that the position and momentum of each normal mode can be approximated as a function of $\mathbf{J}$ and $\boldsymbol{\phi}$. This approach is discussed in more detail in Appendix A. To incorporate additional anharmonic effects, time evolution of the trajectories is not approximated using perturbation theory. Rather, initial conditions computed within this framework are propagated using the full anharmonic Hamiltonian, resulting in the OMT approximation to the response function being nonperturbative in anharmonicity.

In general, the trajectories propagated from these initial conditions are approximations of the desired multiply periodic good action-angle trajectories. Therefore, the time dependence of the angles cannot be derived from these trajectories to numerical precision as they were for a single degree of freedom. The relationship between the angle and time in Eq. (3.1) allows for efficient computation of the response function in the NEFT implementation primarily by enabling the use of precalculated action-quantized trajectories. The fixed-trajectory (FT) implementation maintains the use of precalculated trajectories, but in an approximate manner. As in the NEFT implementation, only one classical trajectory at each set of actions reached during any OMT diagram is computed in the FT implementation. Therefore, a minimal set of trajectories is computed, with the number of

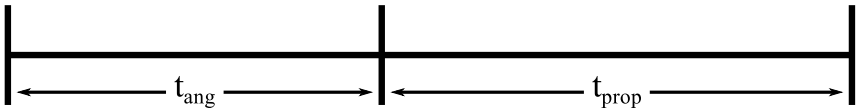

Figure 3.2: Time evolution of trajectories in the FT implementation. Each trajectory can be thought of as consisting of two parts, the first of length t_{ang} should be long enough to sample all combinations of angles. Depending on the angle values, any point in this portion of the trajectory can be treated as the initial state of the trajectory or the state after an action jump. The second portion of the trajectory of length t_{prop} accommodates time evolution of the trajectory for any initial angles.

trajectories depending only on the number of initial action values, not on the time values at which the response function is calculated. In the NEFT implementation each trajectory is propagated for one period of the appropriate oscillation, a time on the order of $2\pi/\omega$. This ensures that all angle values are sampled during each trajectory. For multiple degrees of freedom, each combination of angle values should be sampled in a trajectory propagated at actions, $\mathbf{J}$. To achieve this, each trajectory is propagated for a time, t_{ang}, on the order of the least common multiple of the normal mode's periods. This part of the trajectory approximately samples all angle combinations, assuming the normal mode frequencies are incommensurate. Trajectories are then propagated an additional time, t_{prop}, the maximum propagation time in the appropriate time-interval. The two portions of the trajectory are illustrated in Fig. 3.2. The additional propagation time, t_{prop}, allows for forward-propagation under the full anharmonic Hamiltonian starting from any time in the angle sampling portion of the trajectory and, thereby, from any initial angle values. This was not necessary in the NEFT implementation because the period of the oscillation was known to numerical precision for each action, allowing all times to be taken modulo this value without affecting the accuracy of the calculation.

The second numerical challenge in applying the OMT approximation is computing constant angle jumps between these precomputed action-quantized trajectories. This requires transforming the normal mode coordinates and momenta following trajectory τ according to $\{(x^s(\mathbf{J}_\tau, \boldsymbol{\phi}), p^s(\mathbf{J}_\tau, \boldsymbol{\phi}))\}_s \rightarrow \{(x^s(\mathbf{J}_{\tau+1}, \boldsymbol{\phi}), p^s(\mathbf{J}_{\tau+1}, \boldsymbol{\phi}))\}_s$. Rather than applying perturbation theory to determine the angle values during each transition, we use an approximate procedure that avoids calculating the angle values explicitly. To compute a constant angle jump between an initial and final trajectory a target state is computed by harmonically scaling the initial coordinate and momentum of the normal mode interacting with the field, r, by the square root of the ratio of that mode's final and initial actions, $(J^r_{\tau+1}/J^r_\tau)^{1/2}$. With the unscaled coordinates and momenta of the other normal modes this defines a $2f$-dimensional target state that would represent a jump in action at constant angle values in the absence of anharmonicity, as can be seen from the action dependence of the Q_σ factors in Eq. (2.10). The point in the angle sampling portion of the final trajectory that minimizes the distance to this target state in phase space is used as the endpoint of the approximate constant angle jump. Constant angle mappings between all pairs of trajectories connected by an OMT transition can be precomputed in this way, with each state on the initial trajectory mapped onto a state on the final trajectory. Because of the approximations involved, the mapping from one trajectory to another need not be the inverse of the mapping from the second trajectory to the first.

The final computational challenge is to perform the thermal average over initial conditions. The number of trajectories that need to be precomputed in the FT implementation is directly dependent on the number of initial actions sampled. If each oscillator has relatively high frequency then few quantum states are accessible at equilibrium and the initial action sum will converge with only a few terms. In

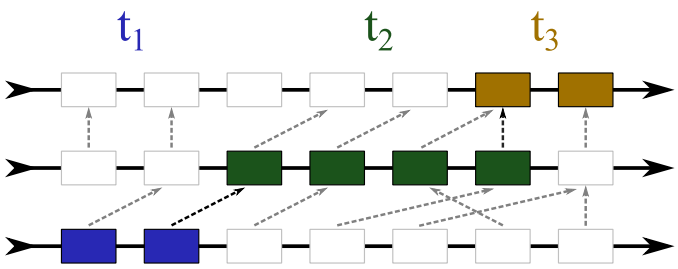

Figure 3.3: Schematic of the FT implementation for an OMT diagram. A single trajectory is computed for each set of actions, depicted by horizontal arrows. Boxes represent discrete classical states along these trajectories. Maps approximating constant angle jumps are represented by dashed arrows connecting classical states on different trajectories. A possible time evolution is shown by colored boxes.

the NEFT method the angle average was performed as a numeric integration, but as noted in Sec. 3.1, the integrands in Eqs. (2.22) and (2.28) have a weak dependence on the initial angle for low-anharmonicity systems. Despite not knowing the explicit time evolution of the angle variables, to the extent that they approximate the good angle variables, they will evolve linearly in time and be multiply periodic. This enables the angle average to be treated as a time average by varying the initial state along the angle sampling part of the trajectory. In our calculations, on the order of a few tens of initial times was sufficient to converge the resulting response functions. The statistical weight of each path ΔF, defined in Eq. (2.23), can be approximated using the same order of perturbation theory used to obtain initial conditions.

The calculations supporting the evaluation of OMT diagrams in the FT implementation are indicated schematically in Fig. 3.3. Each horizontal arrow represents an action-quantized trajectory, with boxes indicating discrete classical states. Dashed arrows indicate mappings between states on different trajectories representing transitions in action at fixed angle values. After the fixed trajectories and mappings between them are computed, time evolution at specified action values is reduced to incrementing the index of the classical state along the appropriate

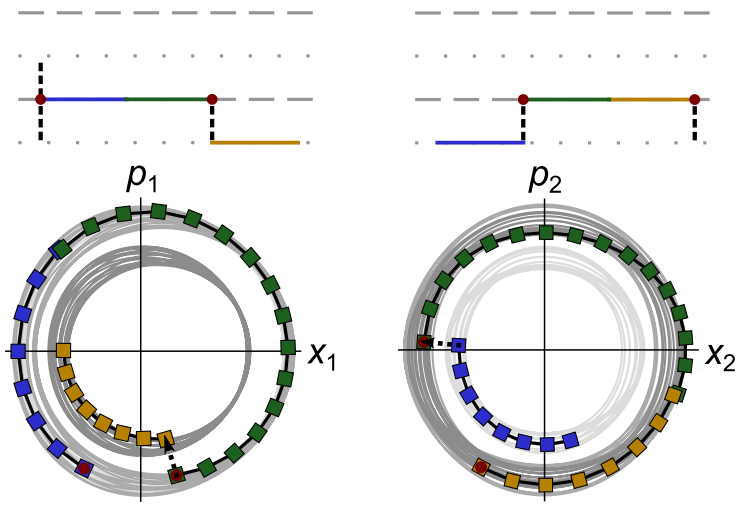

Figure 3.4: Phase space picture of the FT implementation for two coupled Morse oscillators and a given OMT diagram.

trajectory. Similarly, performing transitions between trajectories at constant angle values is reduced to using the appropriate map to identify the starting index on the target trajectory. The phase space average over initial angles is approximated as a time average by varying the starting state indicated by the first blue box in Fig. 3.3. Colored boxes show an example semiclassical path. Depending on the identities of the three trajectories, this schematic could represent the evaluation of any OMT diagram.

Figure 3.4 gives an example OMT diagram and a representation of its evaluation in phase space for two Morse oscillators for a single set of initial conditions and time evolutions. Comparison of Fig. 3.4 with Fig. 3.1 illustrates the essential differences between the NEFT and FT implementations. First, there are differences in the precomputed trajectories used in these two applications of the OMT approximation. In the NEFT implementation continuous trajectories are determined to numerical precision in the good action-angle variables of the system. In the FT implementation perturbation theory is used to determine initial conditions that approximate the coordinate and momenta in good action-angle variables to a

desired order in anharmonicity. These initial conditions are then propagated using the full anharmonic Hamiltonian to obtain discretized classical trajectories. Because the FT implementation is applied to multiple oscillator systems, trajectories must be propagated for longer to ensure that all combinations of action values are reached. Also, trajectories in the FT implementation must be propagated for an additional length of time to allow for correct propagation from any point in the angle sampling part of the trajectory. Fig. 3.4 shows this approximate multiply periodic nature, as the trajectories shown in gray are not simple periodic trajectories as they were in Fig. 3.1. A second distinction between these implementations is that action jumps at constant angle are performed exactly in the NEFT implementation, while they are performed approximately using mappings between discrete classical trajectories in the FT implementation. This can be visualized in Fig. 3.4 where the approximation nature of the action jumps contributes to the non-interacting mode only approximately maintaining its position and momentum in transitioning between trajectories in the OMT diagram. For example, the terminal green and blue boxes are not perfectly aligned in the left phase space plot, nor are the terminal green and yellow boxes in the right phase space plot. A final distinction not visible in these figures is that in the NEFT implementation the angle average is performed using numeric integration while in the FT implementation it is performed using a time average over a few initial conditions.

Each of these approximations will decrease the accuracy of the FT implementation in comparison to the NEFT implementation, but they also enable the OMT to be efficiently applied to multidimensional systems. The cumulative effect of these approximations can be probed by using different sets of fixed trajectories to compute the same spectra. If spectra computed from different initial angle values differ from each other appreciably, the model lies outside of the domain of appli-

cability of this implementation. Such a lack of reproducibility may arise from the approximate method for carrying out transitions in action, from the perturbative identification of action and angle variables to a given order, or from the nonexistence of good action and angle variables. Testing the dependence of final results on initial sets of angle values provides an empirical assessment of the applicability of the theory to a given model.

While the FT implementation is well suited to treat a few high frequency oscillators, there are difficulties when applying it to larger systems or those with disparate frequency scales. The simplicity of the initial action sum is lost when applying the OMT to low frequency oscillators because they thermally access a large range of action values. For these types of systems it is impractical to compute the response function from one fixed set of trajectories. This challenge could be addressed, for example, by computing a fixed set of trajectories for each set of initial, Metropolis sampled, actions for the low frequency modes. A more pressing difficulty arising in systems with disparate frequency scales is a breakdown in the ability to create constant angle mappings between precomputed trajectories. The FT method relies on being able to approximately sample all combinations of bath mode angles in the first part of the discrete trajectories of length t_{ang}. If the oscillators have disparate frequencies then there will be large differences in the oscillator's periods, requiring very long trajectories to be computed on a fine grid to adequately sample all combinations of bath normal mode angles. Failing to maintain the angles of low frequency bath oscillators causes artificial dephasing of the system, and attempting to determine fixed angle jumps for all actions is impractical. These challenges motivate the development of the FB implementation of the OMT described in the following section.

3.3 Forward-Backward Implementation

For systems that include many weakly coupled oscillators or disparate frequency scales the FT implementation presented in Sec. 3.2 is intractable. The forward-backward (FB) implementation can be used to apply the OMT approximation to these types of systems. This implementation has numerical advantages similar to the doorway- and window-function factorization[26,74] described by Hasegawa and Tanimura for the computation of nonlinear spectra with non-equilibrium molecular dynamics simulations.[27]

The FB implementation achieves a higher efficiency than the naive implementation of the OMT approximation by factoring the integrands in Eqs. (2.22) and (2.28) into parts that occur before and after the waiting time propagation, rather than by precomputing fixed trajectories. This factorization can be achieved by replacing $\mathbf{z}_1$ by $\mathbf{z}_1(t_1)$ in the factors Γ and ΔF, defined in Eqs. (2.25) and (2.23), in Eqs. (2.22) and (2.28) and changing integration variables from $\mathbf{z}_1$ to $\mathbf{z}_1(t_1)$. These substitutions leave the response function unchanged since both points lie on the same constant-action trajectory and F, defined in Eq. (2.32), has no angle dependence for the good action variables of the coupled Hamiltonian. Therefore, in the FB implementation the contributions to the response function associated with wavevector, $\alpha\mathbf{k}_1 + \beta\mathbf{k}_2 + \gamma\mathbf{k}_3$, in which all interactions occur with mode r or with a trace-satisfying sequence of mode interactions $\boldsymbol{\zeta}$, previously described by Eqs. (2.22) and (2.28), respectively, are,

$$\rho^r_{\gamma\beta\alpha}(t_3,t_2,t_1) = \frac{i}{2^4\hbar^{2f+3}}\sum_{d=1}^{4}\epsilon_d\int d\mathbf{z}_1(t_1)\left[\Delta F^r(\mathbf{z}_1(t_1))\Gamma^r(\mathbf{z}_1(t_1))Q^r_\alpha(\mathbf{z}_1)Q^r_\beta(\mathbf{z}'_d)\right]$$
$$\times\left[\int d\mathbf{z}_2\int d\mathbf{z}_3\delta(\boldsymbol{\phi}_2-\boldsymbol{\phi}_1(t_1))\delta(\boldsymbol{\phi}_3-\boldsymbol{\phi}_2(t_2))\Delta^r_{1\sigma_d}\Delta^r_{2\sigma'_d}Q^r_\gamma(\mathbf{z}''_d)Q^r_\delta(\mathbf{z}_3(t_3))\right], \quad (3.3)$$

$$\rho^{\boldsymbol{\zeta}}_{\gamma\beta\alpha}(t_3,t_2,t_1) = \frac{i}{2^4\hbar^{2f+3}}\sum_{d=1}^{8}\epsilon_d \int d\mathbf{z}_1(t_1)\left[\Delta F^{\zeta_0}(\mathbf{z}_1(t_1))\Gamma^{\zeta_0}(\mathbf{z}_1(t_1))Q^{\zeta_0}_{\alpha}(\mathbf{z}_1)Q^{\zeta_1}_{\beta}(\mathbf{z}'_d)\right]$$
$$\times\left[\int d\mathbf{z}_2\int d\mathbf{z}_3\delta(\boldsymbol{\phi}_2-\boldsymbol{\phi}_1(t_1))\delta(\boldsymbol{\phi}_3-\boldsymbol{\phi}_2(t_2))Q^{\zeta_2}_{\gamma}(\mathbf{z}''_d)Q^{\zeta_3}_{\delta}(\mathbf{z}_3(t_3))\Delta^{\zeta_1}_{1\sigma_d}\Delta^{\zeta_2}_{2\sigma'_d}\right]. \quad (3.4)$$

In Eqs. (3.3) and (3.4), the integrand is factored into two expressions, grouped in square brackets. The first factor is independent of t_2 and t_3 and the second is independent of t_1. Therefore, the integrand can be computed as the outer product of these two terms. In the fixed-trajectory implementation, initial Cartesian coordinates and momenta are determined as a function of action-angle variables using low-order perturbation theory applied to the normal modes.[56] These results are used to transform the action-angle variables into Cartesian coordinates and momenta, and the full anharmonic Hamiltonian is used to propagate all trajectories. In the FB implementation, the same procedure is followed, except the perturbative results are used to sample $\mathbf{z}_1(t_1)$ and the phase space point $\mathbf{z}_1$ is obtained by propagating the initial point $\mathbf{z}_1(t_1)$ backward. Therefore, to compute the contribution to the system response from each OMT diagram in the FB implementation a single t_1 and a single t_2 trajectory are propagated. Then for each t_2 value a distinct t_3 trajectory is propagated. This results in the total number of trajectories scaling as the number of t_2 values, n_{t_2}. In comparison, the number of propagated trajectories scales as $n_{t_1}\,(1+n_{t_2})$ in a naive implementation. Typically, 2D IR spectra are plotted as Fourier transforms with respect to t_1 and t_3 for a small number of t_2 times, so that $n_{t_2} \ll n_{t_1}$. The FB implementation is therefore significantly more efficient than the naive implementation, although it does require more trajectories than the fixed-trajectory implementation described in Sec. 3.2.

This implementation is illustrated in Figure 3.5(a) for an OMT diagram in which both interactions with the field increase the system action of a single normal

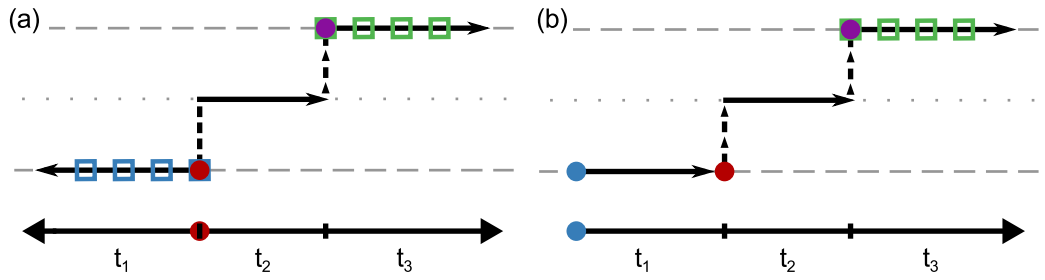

Figure 3.5: The forward-backward implementation of an OMT diagram for a fixed value of t_2 is shown in (a). The diagram is initialized at $\mathbf{z}_1(t_1)$, represented by a red dot, with known $\boldsymbol{\phi}_1(t_1)$ and $\mathbf{J}_1$. The t_1 trajectory is propagated backward from this point to obtain a set of $\mathbf{z}_1$ values, indicated by blue squares. A t_2 trajectory is propagated forward in time from the phase space point $\mathbf{z}_2$, with known initial angles $\boldsymbol{\phi}_2 = \boldsymbol{\phi}_1(t_1)$. For each t_2 value the point after a $\hbar/2$ jump in action $\mathbf{z}_3$, shown as a purple dot, must be determined. From this initial condition a t_3 trajectory is propagated, giving a set of $\mathbf{z}_3(t_3)$ values, shown as green squares. For comparison, an all-forward implementation for a fixed value of t_1 and t_2 is shown in (b), with the starting point of the diagram $\mathbf{z}_1$, indicated by a blue dot.

mode and the system is propagated in a population during the t_2 time. The contribution from this diagram to $\rho^r_{+\pm\mp}$ in Eq. (3.3) is

$$\frac{i}{2^4\hbar^{2f+3}}\int d\mathbf{z}_1(t_1)\left[\Delta F^r(\mathbf{z}_1(t_1))\Gamma^r(\mathbf{z}_1(t_1))Q^r_{\mp}(\mathbf{z}_1)Q^r_{\pm}(\mathbf{z}_1(t_1))\right]$$
$$\times\left[\int d\mathbf{z}_2\int d\mathbf{z}_3\delta(\boldsymbol{\phi}_2-\boldsymbol{\phi}_1(t_1))\delta(\boldsymbol{\phi}_3-\boldsymbol{\phi}_2(t_2))\Delta^r_{1+}\Delta^r_{2+}Q^r_{+}(\mathbf{z}_3)Q^r_{-}(\mathbf{z}_3(t_3))\right]. \quad (3.5)$$

In this implementation the OMT diagram begins at $\mathbf{z}_1(t_1)$, represented by the red dot, instead of at $\mathbf{z}_1$, as in the NEFT and FT implementations. Values of $\mathbf{z}_1$, obtained by propagating backward from $\mathbf{z}_1(t_1)$, are represented by blue squares in Figure 3.5. The constant angle jump at time t_1 is represented by the arrow-less dashed line connecting trajectories 1 and 2 in this path, indicating that the angle at this time is explicitly known. The phase space point $\mathbf{z}_2$ is then propagated forward in time to $\mathbf{z}_2(t_2)$. For each t_2 value a jump in system action at constant angle values is approximately performed to obtain initial conditions $\mathbf{z}_3$ which are finally propagated forward in time to a set of $\mathbf{z}_3(t_3)$ values, shown as green squares. For comparison, Figure 3.5(b) shows an all-forward implementation of the OMT

diagram in (a) for a fixed value of t_1 and t_2. The starting point of this diagram is $\mathbf{z}_1$, represented by a blue dot, and all trajectories are propagated forward in time.

The FB implementation avoids difficulties associated with applying the fixed-trajectory implementation to systems with low frequency oscillations through its treatment of action jumps. By sampling values of $\mathbf{z}_1(t_1)$ directly, $\boldsymbol{\phi}_1(t_1)$ is known, so that computing $\mathbf{z}_2$ requires no approximations in addition to those used to compute $\mathbf{z}_1(t_1)$. Therefore, only the jumps at time t_2 need to be further approximated. Because of the relatively small number of jumps, which scales as n_{t_2} in the FB implementation, these transitions can be treated within the same perturbative framework used to compute initial phase space conditions. This implementation therefore avoids the approximate mapping method for determining constant angle jumps, shown in Fig. 3.3, that is used in the FT approximation.

The final challenge to be addressed is performing the phase space integration. Low frequency bath oscillators thermally sample a large number of action values so that it is impractical to directly sum all combinations of these actions. Therefore, initial conditions for $\mathbf{z}_1(t_1)$ are determined by Metropolis sampling from the equilibrium distribution function F in Eq. (2.32). This results in a set of actions prior to the first interaction with the field, $\mathbf{J}_0 \equiv \mathbf{J}_1|_{J_1^{\zeta_0} \to J_1^{\zeta_0} - \hbar/2}$, and imparts a weight that differs from the desired statistical weight, ΔF in Eq. (2.31). To correct for this difference the response contribution from each diagram is multiplied by $1 - F(\mathbf{z}|_{\mathbf{J}_0, J_0^{\zeta_0} \to J_0^{\zeta_0} + \hbar})/F(\mathbf{z}|_{\mathbf{J}_0})$, with ζ_0 the first interacting mode. As F has no angle dependence, initial angles are chosen from a uniform distribution.

3.4 FB Implementation Including Energy Transfer

In Sec. 2.2.1 the OMT approximation was generalized to include energy transfer by including OMT diagrams with all possible sequences of normal mode interactions. This set of 'parent' OMT diagrams can generate trace-satisfying 'child' diagrams if energy transfer occurs during the numerical propagation of the classical trajectories. To properly incorporate such energy transfer processes, the OMT approximation in Eq. (2.29) must be evaluated so that all child diagrams generated via energy transfer under all-forward propagation can be reached by dynamical processes. This is only possible if the method for executing action jumps alters the interacting mode's current action by $\pm\hbar/2$, even if it changed during the trajectory, and leaves all other actions unchanged, as given in Eq. (2.34). This is fundamentally at odds with a fixed-trajectory implementation of the OMT approximation, which is expected to be otherwise unsuited for the types of systems displaying significant energy transfer, such as the system of two near-resonant chromophores coupled to a low frequency bath presented in Chapter 5. In this section, alterations to the FB implementation in Sec. 3.3 are described that allow for incorporation of energy transfer processes.

The FB implementation achieves a significant increase in efficiency over a naive implementation by factoring OMT diagrams into contributions depending separately on t_1 and t_3. The starting point of each diagram is taken to be $\mathbf{z}_1(t_1)$ with the t_1 trajectory propagated backward in time, and the t_2 and t_3 trajectories propagated forward. This factorization is exact for diagrams propagated at quantized values of the good action variables, but not for diagrams with energy transfer as in Figs. 2.7(a)-(c). Back-propagation during t_1 results in some child diagrams not being naturally generated in the FB implementation as they would be for an im-

plementation with all-forward propagation, a manifestation of the substitution of integration variable $\mathbf{z}_1(t_1)$ for $\mathbf{z}_1$. Also, the substitution of $\mathbf{z}_1(t_1)$ for $\mathbf{z}_1$ in ΔF and Γ cannot be made in Eq. (2.29) as it was in Sec. 3.3 for Eq. (2.21). For these reasons, the FB implementation must be modified from its presentation in Sec. 3.3. First, a simplified method for performing constant angle action jumps is presented that ensures jumps are performed from the mode's current actions. Second, alterations to the implementation that allow for the approximate incorporation of t_1 energy transfer events, otherwise absent from a FB description, are described. Third, approximate methods for determining the statistical weight of each diagram are presented. Finally, the challenge of determining the "correct" arguments of Q^r_σ when energy transfer occurs is discussed. Some of these challenges are inherent to generalizing the OMT to include energy transfer and others are particular to generalizing the FB implementation.

In systems with energy transfer, the normal mode's actions at the time of the interaction may be different from the action values used to initialize the trajectory. Therefore, the action values before and after a jump cannot be determined directly from the initial conditions for a given parent diagram. When propagating new trajectories for each diagram evaluation, as in the FB implementation, constant angle jumps can be approximated within a harmonic limit by scaling the coordinate and momentum of the interacting chromophore r in trajectory τ by $(1 \pm \hbar/2J^r_\tau)^{1/2}$, which is correct for a harmonic oscillator as seen from the action dependence of Q_σ in Eq. (2.10). The actions prior to the jump, $\mathbf{J}_\tau(t)$, can be approximated by equating the perturbative expression for the Hamiltonian in action variables with the full Hamiltonian as a function of time. This allows for interactions with the field to change the interacting mode's action by $\pm\hbar/2$ without assuming the actions are constant in each trajectory. In the FB implementation the action is assumed

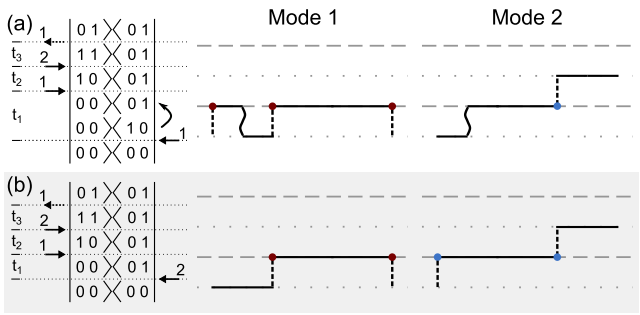

Figure 3.6: Illustration of energy transfer during t_1 in the FB implementation. (a) Child diagram with energy transfer during t_1 reproduced from Fig. 2.7(a). In the FB implementation the parent diagram for (a) is (b) which is a contribution to $\rho^{2,1,2,1}_{++-}$. If energy transfer occurs, the identity of the first interacting mode is changed resulting in child (a).

to be known explicitly at t_1 so that harmonic scaling is not necessary for this jump. We nevertheless include it to ensure that the same energy is propagated during the t_1 and t_3 time periods upon an increasing and decreasing jump when $t_2 = 0$.

The primary challenge in extending the FB implementation to include energy transfer is that not all of the child diagrams with energy transfer during the t_1 time period are naturally generated from the parent diagrams evaluated in Eq. (2.29) in this implementation. For example, Fig. 3.6(a) shows the child diagram from Fig. 2.7(a) with energy transfer during the t_1 time period. In this figure, and in Figs. 3.7 and 3.8, 2FDs are drawn to emphasize the density operator time evolution of two interacting chromophore normal modes of interest. These modes, labeled 1 and 2, are assumed to begin in the ground state and to be coupled to some energy transfer inducing modes, whose quantum numbers are left unspecified. The OMT diagrams in these figures, however, are general and represent possible contributions for any initial actions $\mathbf{J}_1$ and mode identities. To identify a parent diagram in the FB implementation the energy transfer event is removed while the actions at t_1 remain fixed, since these values are associated with the starting point of the diagram. Applying this procedure to the 2FD in Fig. 3.6(a)

results in a spurious diagram in which the field first interacts with mode 1 but the result is an increase in the action of mode 2. To include diagrams like that in Fig. 3.6(a) in the FB implementation, we allow the identity of the first interacting mode r_0 in Eq. (2.29) to vary depending on the chromophore actions at time 0. Specifically, we take the parent diagram for Fig. 3.6(a) in the FB implementation to be the diagram in Fig. 3.6(b), in which the first interacting mode is mode 2. In practice, the identity of the first interacting mode is determined by computing the action of the modes during trajectory 1 as a function of time. We calculate these actions by equating the perturbative expression for the Hamiltonian in action variables with the exact Hamiltonian propagated as a function of the Cartesian coordinates and momenta. The identity of the first interacting mode r_0 is determined by rounding the computed actions to the nearest properly quantized set of values so that $\Gamma^{r_0}(\mathbf{z}_1)$ in Eq. (2.30) is most closely satisfied. We denote the first interacting mode in the parent diagram as r_0', which may or may not be the same as r_0. For example, $r_0' = 2$ for the parent diagram shown in Fig. 3.6(b). If, in evaluating this diagram, back propagation of the t_1 time period results in the actions of modes 1 and 2 changing from approximately $\hbar/2$ and $\hbar$, to approximately $\hbar$ and $\hbar/2$, as in (a) then the identity of the first interacting mode is taken to be mode 1 rather than mode 2 and $r_0 = 1$. This will result in the diagram being evaluated at $Q_\alpha^1(\mathbf{z}_1)$ as in Fig. 3.6(a) and not $Q_\alpha^2(\mathbf{z}_1)$ as in Fig. 3.6(b). As seen in this example, trace-satisfying child diagrams with t_1 energy transfer are generated in the FB implementation from trace-satisfying parent diagrams. In contrast, trace-satisfying diagrams with t_2 and t_3 energy transfer, as in Fig. 2.7(b) and (c), result from non-trace-satisfying parent diagrams, as in Fig. 2.7(d). In an all-forward implementation, trace-satisfying diagrams with t_1 energy transfer are also generated by non-trace-satisfying diagrams, and the OMT diagram in Fig. 2.7(d) would also

be the parent of the diagram in Fig. 3.6(a).

Only OMT diagrams with one chromophore mode's action integer quantized and all other mode's actions half-odd-integer quantized at time t_1 can be generated in the FB implementation by allowing the first interacting mode to vary. If energy transfer can only occur between chromophore modes and all chromophore modes begin in the ground state, this is sufficient to ensure the desired child diagrams generated under all-forward propagation of parent diagrams are included in the FB implementation. Energy transfer can result in other possible states at time t_1 for diagrams not satisfying these conditions. The effect of neglecting these diagrams will depend on the system but does not affect results for the parameters used in Sec. 5.2.

The substitution of $\Delta F^{r_0}(\mathbf{z}_1(t_1))$ for $\Delta F^{r_0}(\mathbf{z}_1)$ in Eq. (2.21) should not be made for systems with energy transfer. Metropolis sampling from the equilibrium distribution F in Eq. (2.32) is used to compute a set of half-odd-integer quantized actions $\mathbf{J}_0$. This sampling weights a diagram initialized with actions $\mathbf{J}_1(t_1) = \mathbf{J}_0|_{J_0^{r_0'} \to J_0^{r_0'}+\hbar/2}$ by $F(\mathbf{z}|_{\mathbf{J}_0})$. As in the original FB approximation, the weight of each diagram can be corrected by multiplying its contribution to the response function by the factor $1 - F(\mathbf{z}|_{\mathbf{J}_0, J_0^{r_0} \to J_0^{r_0}+\hbar})/F(\mathbf{z}|_{\mathbf{J}_0})$. Unlike in the FB approximation without energy transfer, here r_0 is determined according to the procedure described above, so that r_0 is not necessarily equal to the initial interacting mode in the parent diagram, r_0'. This will result in the correct statistical weight in the absence of energy transfer. If energy transfer occurs during the t_1 time period this correction will be approximate in the FB implementation. The effect of this approximation on the calculated response function is expected to be small, especially when energy transfer predominately oc-

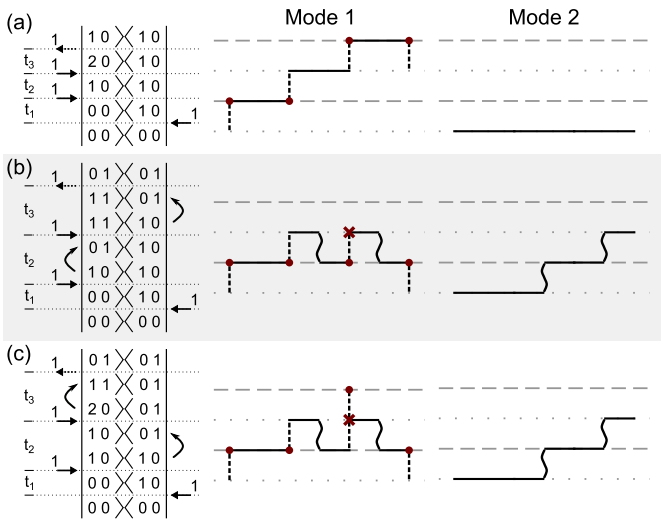

Figure 3.7: Example contributions to $\rho^{1,1,1,1}_{++-}$ are shown. Red dots correspond to points on the diagram where factors of Q^r_σ are evaluated in Eq. (2.29). If a different point is chosen at time t using the approximate method described in text, it is indicated by an x.

curs between modes with similar frequencies. If necessary, better corrections can be made. For example, rather than computing the statistical weight from the sampled action $\mathbf{J}_0$, which assume the bath modes actions are fixed, the statistical weight can be computed from the back-propagated classical trajectories, as $\left(\exp\left[-\beta H\left(\mathbf{z}_1|_{J^{r0}\to J^{r0}-\hbar/2}\right)\right]-\exp\left[-\beta H\left(\mathbf{z}_1|_{J^{r0}\to J^{r0}+\hbar/2}\right)\right]\right)\exp\left[\beta H\left(\mathbf{z}|_{J_0}\right)\right]$.

A final approximation will be applied to determine the arguments of Q^r_σ in Eq. (2.29). In general, the arguments of the factors Q^r_σ should vary if energy transfer occurs in a diagram. In Fig. 3.7(a) a trace-satisfying parent diagram contributing to $\rho^{1,1,1,1}_{++-}$ is shown with two possible child diagrams in (b) and (c). The correct points for evaluating the Q^r_σ factors are shown as colored dots in each OMT diagram, determined according to the procedure described in Chapter 2. As can be seen by comparing the dot placement for the third interaction with mode 1 in panels (a) and (b), energy transfer can change both the magnitude of the action at which Q^r_σ is evaluated as well as its value relative to the action prior to the

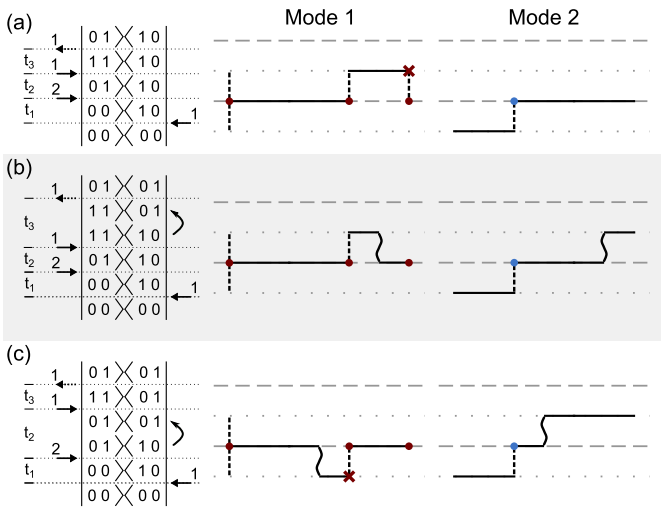

Figure 3.8: Example contributions to $\rho^{1,2,1,1}_{+++-}$ are shown. Red and blue dots correspond to points on the diagram where factors of Q^r_σ are evaluated in Eq. (2.29). If a different point is chosen using the approximate method described in text, it is indicated by an x.

jump. Furthermore, it is not always possible to uniquely determine the correct arguments of Q^r_σ based on the diagram since distinct information about the bra and ket aspects of the density operator is not maintained throughout the trajectory, only the average action. The distinct 2FDs in Fig. 3.7(b) and (c), for example, give rise to their respective OMT diagrams which differ only in the action value at which $Q^1_\gamma(\mathbf{z}'_d)$ is evaluated. When propagating the parent diagram in (a) it is not possible to distinguish between the two sequences of energy transfer events in the 2FDs shown in (b) and (c) since both correspond to the same sequence of changes in the average action of the trajectories. This figure therefore demonstrates that for some sequences of energy transfer events there is inherent ambiguity in determining the arguments of Q^r_σ. To deal with this ambiguity, and simplify the evaluation of OMT diagrams, we will make the following choices for the arguments of Q^r_σ evaluated in Eq. (2.30). The first factor in a trace-satisfying diagram is always given by $Q^{r_0}_\alpha(\mathbf{z}_1)$, with r_0 determined appropriately for each evaluation time. The t_1 phase space points are sampled directly in the FB implementation, and serve as the starting

point of the diagram, so that if $Q_\beta^{r_1}(\mathbf{z}_d)$ is evaluated at the correct action for the parent diagram it will also be correct for all of its child diagrams. For the signal associated with wavevector $\mathbf{k}_{\mathrm{I}}$ or $\mathbf{k}_{\mathrm{II}}$ this will be the integer quantized action value involved in the transition. In the $\mathbf{k}_{\mathrm{III}}$ phase-matched direction this may be a point not directly involved in the path, as in Fig. 2.6(aii) or Fig. 2.10(a) and (b). We will choose to evaluate $Q_\gamma^{r_2}$ at time $t_1 + t_2$ in the $\mathbf{k}_{\mathrm{I}}$ or $\mathbf{k}_{\mathrm{II}}$ phase-matched direction at the action of the oscillator either before or after the jump, whichever is an integer multiple of $\hbar$ in the parent diagram without energy transfer. For example, a non-trace-satisfying parent diagram is shown in Fig. 3.8(a), with (b) and (c) showing example trace-satisfying child diagrams with energy transfer during the t_3 and t_2 time periods, respectively. In the parent diagram in Fig. 3.8(a), mode 1 transitions to a half-odd-integer action in the third interaction with the field. Therefore for all child diagrams, including those in Fig. 3.8(b) and (c), the point prior to the third interaction with the field, $\mathbf{z}_2(t_2)$, is taken as the argument of $Q_\gamma^{r_2}$. This will be the correct evaluation point if, as in Fig. 3.8(b), no energy transfer occurred during the t_2 time interval and if this interaction does not cause a transition to or from a two-quantum coherence. For $\mathbf{k}_{\mathrm{I}}$ and $\mathbf{k}_{\mathrm{II}}$, trace-satisfying parent diagrams will not be in a two-quantum coherence during t_2 or t_3 although some trace-satisfying child diagrams may be. For the $\mathbf{k}_{\mathrm{III}}$ phase-matched direction, we will make this same choice, except for the trace-satisfying diagrams in Fig. 2.6(aii) which will be evaluated at the correct actions for these parent diagrams, with their children evaluated at the same relative actions. We take the final evaluation point at time $t_1 + t_2 + t_3$ to be $Q_\delta^{r_3}(\mathbf{z}_3(t_3))$, which is correct for any trace-satisfying diagram. If a factor of Q_σ^r is not evaluated at the correct argument according to these rules the approximate selected point is shown as an x in Figs. 3.7 and 3.8. This simplifying approximation may select an action that is too high (x higher than dot), as in

3.7(b) or an action that is too low (x lower than dot), as in 3.7(b) or 3.8(c). We expect the effect of this approximation to be small since factors of Q_σ^r are evaluated at the correct arguments in all trace-satisfying parent diagrams, and at least three of the evaluation points will be correct for all trace-satisfying diagrams.

Chapter 4

Results for One and Two Degrees of Freedom

4.1 One Degree of Freedom

OMT calculations of the third order vibrational response function are presented for a single degree of freedom with quantum Hamiltonian,

$$\hat{H} = \frac{\hat{p}^2}{2m} + V(\hat{q}). \tag{4.1}$$

The potential $V(\hat{q})$ in Eq. (4.1) is taken to be either the Morse potential, $V(\hat{q}) = D\left(1 - \exp\left[-\sqrt{\frac{m\omega^2}{2D}}\hat{q}\right]\right)^2$, or the potential for a quartically perturbed harmonic oscillator, $V(\hat{q}) = \frac{1}{2}m\omega^2\hat{q}^2 + a\hat{q}^4$. The response function is plotted in dimensionless form, either as $m^2\omega^2 D R^{(3)}_{\gamma\beta\alpha}(t_3, t_2, t_1)$ for the Morse potential or as $m^4\omega^5 a^{-1} R^{(3)}_{\gamma\beta\alpha}(t_3, t_2, t_1)$ for the quartically perturbed harmonic potential. The response function is taken to be a function of the three dimensionless time intervals, ωt_1, ωt_2, and ωt_3 with two additional dimensionless parameters. The first is a quantum mechanical parameter $\beta\hbar\omega$ and the second is a classical parameter quantifying the system anharmonicity, βD for the Morse potential and $a/(\beta m^2\omega^4)$ for the quartically perturbed potential. In these expressions, $\beta \equiv 1/k_{\mathrm{B}}T$. The classical analog of Eq. (4.1) was used to propagate all trajectories in the OMT calculations. For this set of parameters, the 7 lowest energy eigenstates of the Hamiltonian are sufficient to converge the quantum response function calculation. These states are computed using a basis of 25 harmonic oscillator eigenstates.

4.1.1 NEFT Implementation Results

Here we present results for the numerically exact fixed-trajectory (NEFT) implementation of the OMT, discussed in Sec. 3.1, for all three time-dependences of the third order response function.

The real parts of $R_{\mathrm{I}}^{(3)}(t,0,t)$ and $R_{\mathrm{III}}^{(3)}(t,0,t)$, contributing in the $\mathbf{k}_{\mathrm{I}} = -\mathbf{k}_1 + \mathbf{k}_2 + \mathbf{k}_3$ and $\mathbf{k}_{\mathrm{III}} = \mathbf{k}_1 + \mathbf{k}_2 - \mathbf{k}_3$ phase-matched directions, are shown in column (i) and column (ii) of Figure 4.1, respectively, for a thermal ensemble of Morse oscillators with $\beta\hbar\omega = 2$ and $\beta D = 40$. Quantum mechanical results are shown in row (a) and OMT results computed with the NEFT implementation are shown in row (b). Several quantum states are accessible at thermal equilibrium for this set of parameters. Therefore, OMT results were computed using a maximum initial action of $J_1 = 5\hbar$, which was sufficient to converge the action sum in Eq. (2.21) to the desired accuracy. Results are not presented for the $\mathbf{k}_{\mathrm{II}}$ phase-matched direction for these parameters because, on this scale, they are indistinguishable from results for the $\mathbf{k}_{\mathrm{III}}$ direction, shown in column (ii).

The $R_{\mathrm{I}}^{(3)}(t,0,t)$ signal in column (i) of Figure 4.1 represents the vibrational echo. For this model the quantum mechanical response in (ai) nearly filters out all system frequencies except the anharmonic quantum frequency $\omega_{n+1,n} - \omega_{n+2,n+1} = \hbar\omega^2/2D$, as was previously shown in Fig. 7 of Ref. 64, with $\omega_{n,n'} \equiv (E_n - E_{n'})/\hbar$. The OMT result in (bi) reproduces this dominant oscillation. In the limit of harmonic selection rules, which restrict each field interaction to cause one-quantum transitions, this can be understood as the results of cancellation of time-evolution during the t_1 and t_3 time periods. In the $\mathbf{k}_{\mathrm{I}}$ phase-matched direction the two OMT diagrams with $J_1 = J_3$ evolve with the same frequency during the t_1 and t_3 time periods but with opposite phase, resulting in cancellation of all time dependence

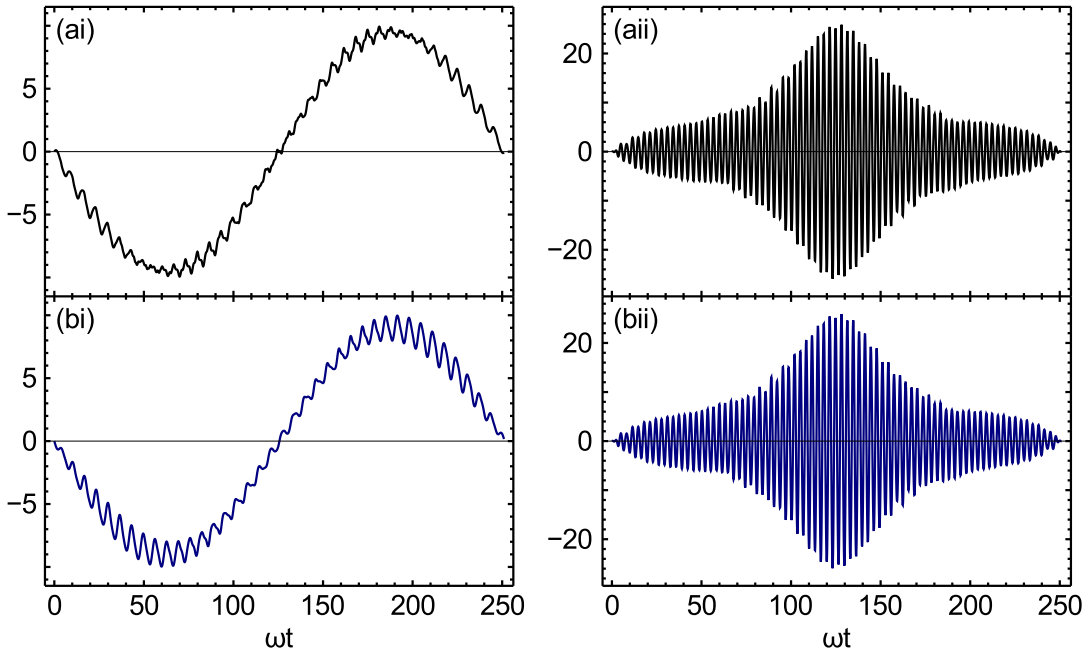

Figure 4.1: The real parts of $R_{\mathrm{I}}^{(3)}(t,0,t)$ and $R_{\mathrm{III}}^{(3)}(t,0,t)$ are shown in columns (i) and (ii), respectively for a thermal ensemble of Morse oscillators with $\beta\hbar\omega = 2$ and $\beta D = 40$. Quantum mechanical results are shown in row (a) and OMT results computed with the NEFT implementation are shown in row (b).

when $t_1 = t_3$, as discussed in Sec. 1.3. The time dependence arises for the echo condition in this limit entirely from the two OMT diagrams with $J_1 \neq J_3$ which contribute at the frequency difference given above. The accuracy of the OMT results demonstrates the ability of the method to reproduce frequency contributions with enough accuracy to replicate this signal cancellation. Both the quantum mechanical and the OMT results also show qualitatively similar higher frequency oscillations which are the result of anharmonic effects beyond the quasiharmonic limit of Eq. (2.10). In addition to the low frequency oscillation, the quantum mechanical $R_{\mathrm{III}}^{(3)}(t,0,t)$ signal in (aii) includes higher frequency contributions at approximately 2ω. The OMT approximation is again able to reproduce the relative contributions of these frequencies to replicate the quantum mechanical results.

All results in Fig. 4.1 are shown for a single period of oscillation given by

$4\pi D/(\hbar\omega^2) \approx 251\omega^{-1}$. This slow oscillation has a frequency proportional to $\hbar$, representing a quantum recurrence that is entirely absent in a fully classical mechanical calculation of the response function for the same potential.[75] Although the results are plotted for only a single period, a similar level of agreement between the results remains at long times as the response repeats. The OMT semiclassical calculation is therefore able to quantitatively reproduce this quantum recurrence, demonstrating that quantum effects in nonlinear vibrational response functions for anharmonic potentials can be accurately reproduced using the OMT approximation based on computing classical trajectories connected by deterministic transitions.

Figure 4.1 demonstrates that the OMT response can accurately reproduce t_1 and t_3 dynamics. Waiting time dynamics are investigated in Fig. 4.2, which shows the real part of $R^{(3)}_{\mathrm{III}}(5,t,0)$ for a thermal ensemble of Morse oscillators with the same parameters as in Fig. 4.1. Panel (a) of Fig. 4.2 shows the quantum mechanical result and the OMT result is given in panel (b). In the limit of harmonic selection rules, this component of the system response has nontrivial t_2 dependence for a single degree of freedom, arising from two-quantum coherences. Results corresponding to wavevectors $\mathbf{k}_{\mathrm{I}}$ and $\mathbf{k}_{\mathrm{II}}$ are not shown because, in this limit, these directions undergo population dynamics during the t_2 period. Therefore, for a single degree of freedom without population dynamics, these components show only weak t_2 dependence arising from multiple-quantum transitions not allowed in the harmonic limit. The OMT result in panel (b) shows overall good agreement with the quantum result, although there are some visible differences.

A quantitative comparison of the quantum mechanical and OMT results' waiting time dependences can be made more readily in the frequency domain. Fig-

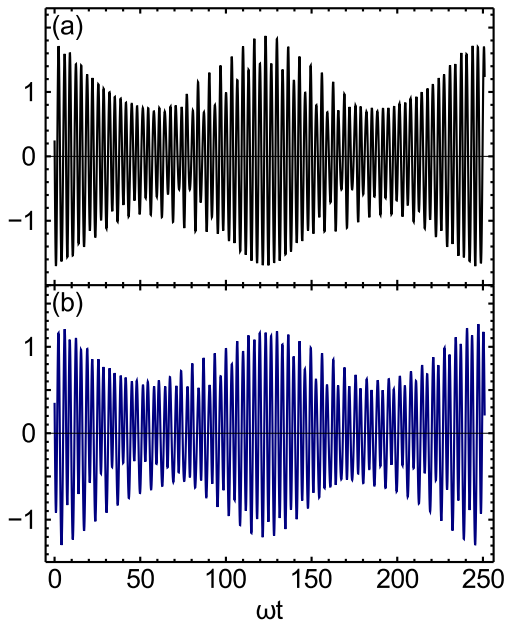

Figure 4.2: The real part of $R^{(3)}_{\mathrm{III}}(5,t,0)$ is shown for a thermal ensemble of Morse oscillators with $\beta\hbar\omega = 2$ and $\beta D = 40$. The quantum mechanical result is shown in (a) and the OMT result calculated with the NEFT implementation is shown in (b).

ure 4.3 shows $|\tilde{R}^{(3)}_{\mathrm{III}}(5,\omega',0)|^2$, the absolute square of the Fourier transform of $R^{(3)}_{\mathrm{III}}(5,t,0)$ in Fig. 4.2 with respect to the waiting time t. The quantum mechanical result is shown in panel (a) and the OMT result in panel (b). The quantum and semiclassical exact spectra for the vibrational Hamiltonian in Eq. (4.1) consist of Dirac delta function peaks since this model does not include any broadening mechanisms. Apparent peak widths in Fig. 4.3 are a result of the finite frequency resolution obtained by taking the discrete Fourier transformation of the response function for a finite time period. To approximately compare the relative contributions to the signal, peak areas have been computed. In Fig. 4.3, the integrated areas are shaded in gray, and the corresponding delta-function peak heights are indicated by colored dots. The spectra are normalized so that the dominant peak, associated with frequency $\omega_{2,0}$, has unit area. Gray dashed vertical lines label the frequencies and relative contributions present in the quantum spectrum in

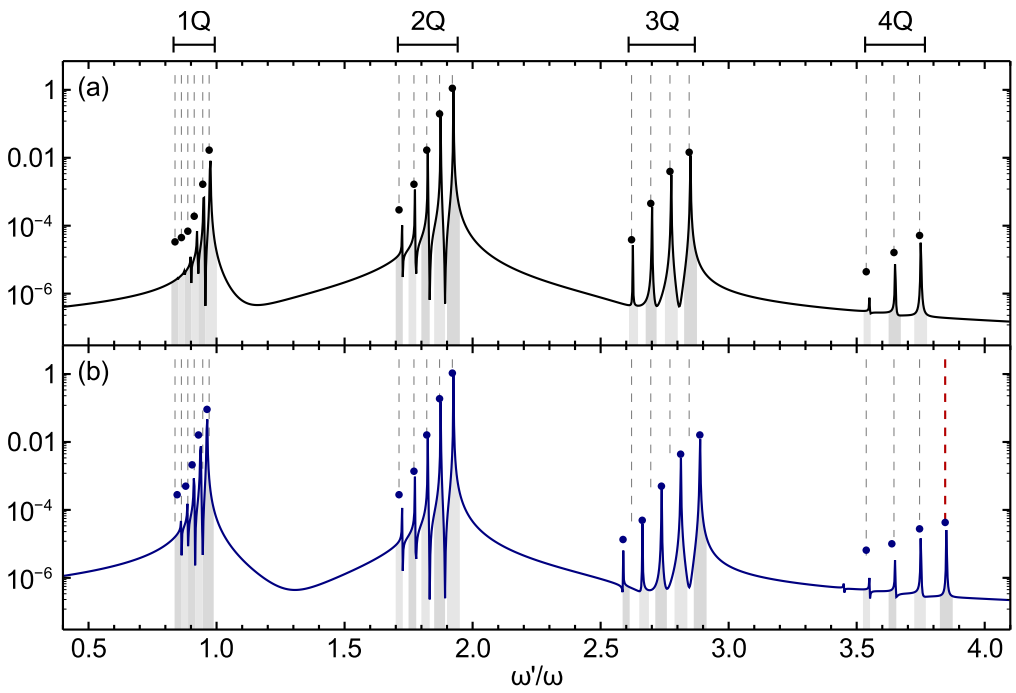

Figure 4.3: The frequency dependence of $|\tilde{R}^{(3)}_{\mathrm{III}}(5,\omega',0)|^2$ for a thermal ensemble of Morse oscillators with $\beta\hbar\omega = 2$ and $\beta D = 40$ is shown on a semilogarithmic plot. The quantum mechanical result is shown in (a) and the OMT calculation in (b). Spectra are normalized so that the dominant peak at $\omega_{2,0}$ has unit area. Peaks associated with n-quantum coherences are labeled nQ.

panel (a). The red dashed vertical line indicates an erroneous frequency in the OMT calculation discussed below.

In the limit of harmonic selection rules, the waiting time evolution of the $\mathbf{k}_{\mathrm{III}}$ signal is a result of two-quantum coherences with frequencies,

$$\omega_{n+2,n} = 2\omega - \left(\frac{\hbar\omega^2}{D}\right)\left(n + \frac{3}{2}\right). \tag{4.2}$$

The peaks corresponding to these frequencies are labeled 2Q in Fig. 4.3. The quantum mechanical result in Fig. 4.3(a) shows five peaks corresponding to these frequencies for $n = 0$ to $n = 4$. The OMT calculation in panel (b) quantitatively reproduces the 2Q frequencies present in the quantum mechanical response. The relative contributions of these frequencies are also well reproduced. In the quantum calculation of Fig. 4.3(a), the integrated areas of the 2Q peaks at $\omega_{3,1}$ and $\omega_{4,2}$ are

18% and 1.7% of the area of the dominant 2Q peak at $\omega_{2,0}$, respectively. In the OMT calculation in Fig. 4.3(b), these peaks have 17% and 1.5% of the relative area, respectively, similar to the quantum mechanical values.

The remaining peaks in Fig. 4.3 labeled 1Q, 3Q, and 4Q correspond to one, three, and four quantum coherence frequencies, respectively. These peaks are present in the spectrum due to deviations from the harmonic approximation of Eq. (2.10) and from harmonic selection rules. The peaks associated with 1Q and 3Q coherences are reproduced qualitatively by the OMT approximation, which results from this calculation employing numerically exact dynamics of the classical trajectories governed by the Morse potential. The 4Q frequencies are reproduced accurately in the OMT results, likely because the 4Q frequencies $\omega_{n+3,n-1}$ correspond to the same average quantum number as the 2Q frequencies $\omega_{n+2,n}$. Because of this, the two frequencies are represented in the OMT approximation by classical trajectories with the same action. The OMT result in Fig. 4.3(b) contains a spurious peak, not present in the quantum spectra, that corresponds to the system frequency $\omega_{3,-1}$. This peak is labeled by a red dashed vertical line in Fig. 4.3(b) and is present in the OMT results because $\omega_{3,-1}$ corresponds to the same average action as the allowed frequency, $\omega_{2,0}$. The intensity of this extra 4Q peak is several orders of magnitude lower than the $2Q$ peaks so its presence does not result a significant discrepancy in the time-domain plots shown in Fig. 4.2.

The calculations in Figs. 4.1-4.3 demonstrate the accuracy of the OMT method for the Morse potential. As noted in connection with Eqs. (2.14) and (2.17), the OMT is expected to be particularly accurate for the Morse potential, because the classically propagated frequencies are the same as the quantum mechanical frequencies. To assess the OMT for a more general anharmonic potential, the t_2

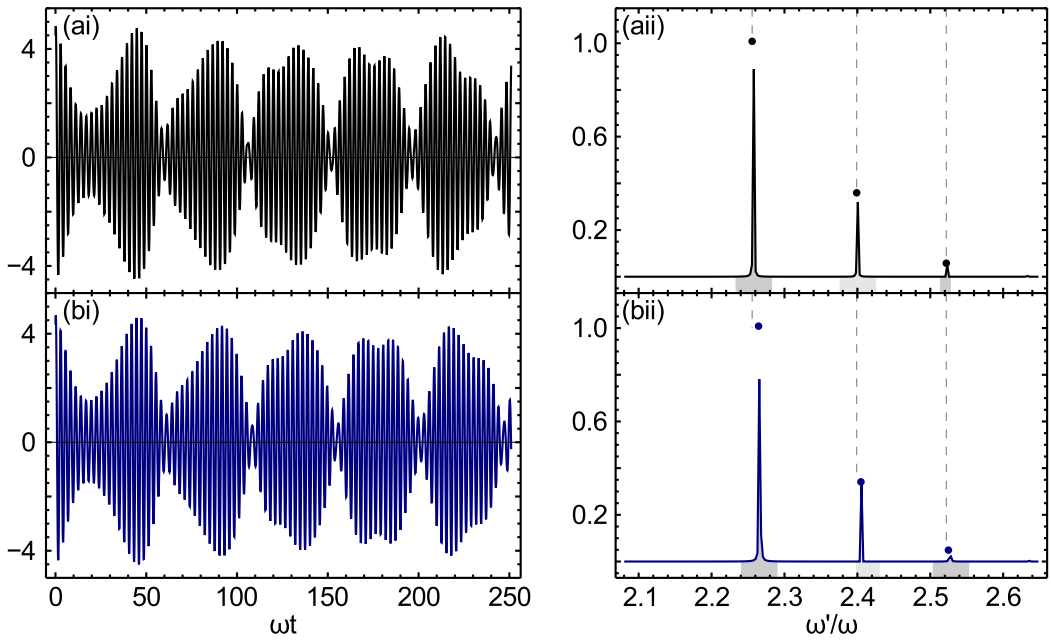

Figure 4.4: The real part of $R^{(3)}_{\rm III}(5,t,0)$ for a thermal ensemble of quartically perturbed harmonic oscillators with $\beta\hbar\omega = \sqrt{2}$ and $a/(\beta m^2\omega^4) = 0.025$ is shown in column (i). The corresponding frequency spectrum, $|\tilde{R}^{(3)}_{\rm III}(5,\omega',0)|^2$, is shown in column (ii). Dots indicate the area of each peak relative to the peak at $\omega_{2,0}$. Quantum mechanical results are shown in row (a) and OMT results in row (b).

dependence of the response function for a quartically perturbed harmonic oscillator is shown in Fig. 4.4, for $\beta\hbar\omega = \sqrt{2}$ and $a/(\beta m^2\omega^4) = 0.025$. Column (i) shows the real part of $R^{(3)}_{\rm III}(5,t,0)$ and column (ii) shows the 2Q peaks of the $\left|\tilde{R}^{(3)}_{\rm III}(5,\omega',0)\right|^2$ signal. Dots indicate peak areas relative to the dominant peak at $\omega_{2,0}$. Quantum mechanical results are given in row (a) and OMT results are shown in row (b). The principal features discussed in connection with the Morse oscillator calculations in Fig. 4.3 are also present for the quartically perturbed harmonic oscillator. The OMT results reproduce the 2Q peaks of the quantum mechanical response. Only this region of the frequency domain is shown in Fig. 4.4. Outside of this range the OMT calculation qualitatively reproduces minor frequency contributions present in the quantum results due to deviations from harmonic selection rules, as in Fig. 4.3. Despite only qualitative agreement, these peak intensities

are several orders of magnitude lower than the dominant 2Q peaks and so have minimal impact on the time-domain results in column (i). Unlike the Morse oscillator results, the frequencies of 2Q peaks in Fig. 4.3(bii) are shifted relative to the exact quantum results in panel (aii), with the quantum frequencies and relative contributions shown as dashed gray lines in each panel for comparison. For these parameters, this shift is small with less than a 1% error in the dominant $\omega_{2,0}$ peak frequency. The relative areas of the overtone 2Q peaks are well reproduced by the OMT approximation. In the quantum mechanical results $\omega_{3,1}$ and $\omega_{4,2}$ contribute at 35% and 5% of the $\omega_{2,0}$ peak area, respectively. In the OMT result these relative contributions are 33% and 4%. The accuracy of the OMT results for the quartically perturbed harmonic potential in Fig. 4.4 demonstrates that the method can well approximate the quantum mechanical response function for more general anharmonic systems.

As demonstrated in Figs. 4.1-4.3 for a Morse potential and in Fig. 4.4 for a quartically perturbed harmonic potential, the OMT approximation is able to quantitatively reproduce dynamics during each of the three time periods for several phase-matched contributions to the third order response function. Specifically, it accurately reproduces waiting time dynamics for the $\mathbf{k}_{\mathrm{III}}$ signal which primarily results from the evolution of two-quantum coherences, overcoming the shortcomings of the MT approximation[63–66] as discussed in Appendix B.

4.1.2 Comparison of OMT Implementations

OMT results in Sec. 4.1.1 are computed using the numerically exact fixed-trajectory implementation (NEFT). For systems with a larger number of degrees of freedom, the NEFT method becomes intractable and the more approximate

fixed-trajectory (FT) and forward-backward (FB) implementations must be applied. Here we will compare results for a single degree of freedom computed with these three implementations.

Figure 4.5 shows results for a thermal ensemble of Morse oscillators with $\beta\hbar\omega = 2$ and $\beta D = 40$. $\left|\tilde{R}_{\mathrm{I}}^{(3)}(\omega', 0, \omega')\right|^2$, $\left|\tilde{R}_{\mathrm{III}}^{(3)}(\omega', 0, \omega')\right|^2$, and $\left|\tilde{R}_{\mathrm{III}}^{(3)}(5, \omega', 0)\right|^2$ are shown in columns (i), (ii), and (iii), respectively. Quantum mechanical results and results computed with the NEFT are shown in rows (a) and (b). The frequency spectra in (ai), (aii), (bi), and (bii) correspond to the time-domain results in the same panels of Fig. 4.1. These results show that there is quantitative agreement between OMT and quantum mechanical results for the parameters and time dependences in Fig. 4.1. The waiting time results in (aiii) and (biii) reproduce the dominant frequency contributions of Fig. 4.3 on a linear scale. FT results are shown in row (c). For these results the maximum initial energy was taken to be $J_1 = 5\hbar$ and the angle average was approximated using 25 states in the angle sampling portion of the initial action trajectory. This portion of the discrete trajectories was of length $8\omega^{-1}$ with step size $0.05\omega^{-1}$, sufficiently long to include a period of oscillation for each action value sampled. Third order perturbation theory in anharmonicity was used to compute initial conditions as described in Appendix A. FB results are shown in row (d). These results were computed with 500 initial conditions, using third order perturbation theory both to select initial conditions and to perform action jumps. Dashed vertical lines running through all spectra indicate the dominant frequencies present in the quantum mechanical results. Gray shadings indicate regions integrated to obtain peak areas, shown as dots. All spectra were normalized so that the dominant peak has unit area.

As previously discussed, the NEFT implementation shows excellent agreement

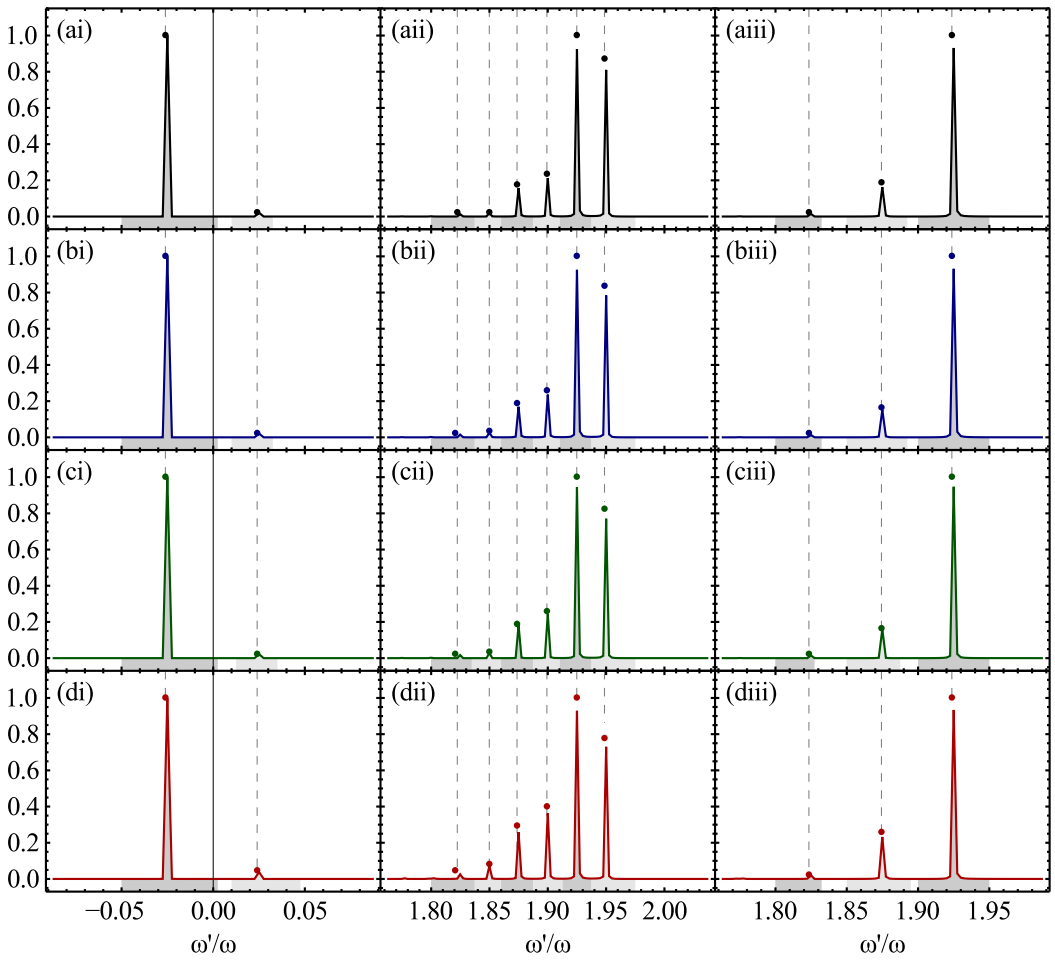

Figure 4.5: $\left|\tilde{R}^{(3)}_{\mathrm{I}}(\omega', 0, \omega')\right|^2$, $\left|\tilde{R}^{(3)}_{\mathrm{III}}(\omega', 0, \omega')\right|^2$ and $\left|\tilde{R}^{(3)}_{\mathrm{III}}(5, \omega', 0)\right|^2$ are shown in columns (i), (ii), and (iii), respectively, for a thermal ensemble of Morse oscillators with $\beta\hbar\omega = 2$ and $\beta D = 40$. Dots indicate the area of each peak relative to the dominant peak in each spectrum, with the integrated areas shown in gray. Quantum mechanical results are shown in row (a). OMT results computed with the NEFT, FT, and FB implementations are shown in rows (b), (c), and (d), respectively.

with the quantum mechanical results. The FT results shown in (c) also well reproduce the frequencies present in the quantum mechanical results and their relative contributions. As in the NEFT calculation, the FT implementation uses a single set of numerical trajectories. As a reminder, the main differences between the methods are: (1) using approximate, instead of exact, actions which are computed using perturbation theory; (2) approximating constant angle jumps by determin-

ing the state on the final trajectory closest to the harmonically scaled initial phase space point; and (3) treating the angle average as an average over a few initial times, rather than performing a numerical integration over the angle variable. For this system and the order of perturbation theory applied, these approximations do not affect the ability of the OMT to accurately reproduce the dominant features of the spectra.

Results computed using the FB method are given in row (d) of Fig. 4.5. Overall, these results also show good agreement with the quantum spectra. The dominant frequencies are accurately reproduced but some overtone contributions in (dii) and (diii) are overestimated. Some aspects of this implementation are more accurate than in the FT method. For example, instead of using harmonic scaling to approximate constant angle jumps, position and momentum values are numerically inverted using perturbation theory to determine the angle prior to the jump at time t_2, and the angle is known exactly at time t_1. These angles are used to determine initial conditions for the appropriate segments of each OMT diagram using perturbation theory. Also, the initial angle average is performed explicitly, not as a time average of a single, perturbatively determined, trajectory as the in FT implementation. This increased accuracy of averaging is apparent if the spectra are viewed on a semilogarithmic plot as in Fig. 4.3 (not shown). Due to noise, the FT calculation has difficulty reproducing low-intensity contributions. Despite this, there are advantages of using a single fixed set of trajectories in addition to making the phase space average more efficient. If perturbation theory results in less accurate approximations of the desired quantized trajectories, averaging diagrams computed with different actions will result in an overall decay in the time-domain, manifesting as peak broadening in the FB frequency spectra. In contrast, this diminished accuracy will result in small frequency shifts in the FT spectra.

These results demonstrate that both the FT and FB implementations are capable of reproducing the quantum mechanical response function to a high level of accuracy, similar to the accuracy of the NEFT implementation. The FT method is especially applicable to systems consisting of a small number of strongly coupled oscillators, particularly when the system cannot access many states at thermal equilibrium. The angle average in the FT implementation can generally be performed using a few initial states. For this set of parameters, 25 initial states was sufficient to converge the system response; however, this number will increase with the number of degrees of freedom. The FB method requires averaging trajectories that are computed using perturbation theory. For high anharmonicity oscillators this can cause artificial dephasing in the response function if the perturbation theory results do not sufficiently approximate the good action-angle variables. Here, third order perturbation theory was sufficient to well reproduce the system response. The development of this implementation was motivated in Chapter 3 by the need to treat systems with disparate frequency scales. For these systems there are dephasing mechanisms which may dominate the spurious dephasing caused by the angle average when the action-angle description is less accurate.

4.2 Two Degrees of Freedom

We present calculations of the third order vibrational response function components associated with wavevectors $\mathbf{k}_{\mathrm{I}}$ and $\mathbf{k}_{\mathrm{III}}$ for two coupled oscillators described by the quantum Hamiltonian,

$$\hat{H} = \frac{\hat{p}_a^2}{2m_a} + \frac{\hat{p}_b^2}{2m_b} + V_a(\hat{q}_a) + V_b(\hat{q}_b) + c_{ab}\sqrt{m_a m_b}\omega_a\omega_b\hat{q}_a\hat{q}_b \tag{4.3}$$

We take, $\hat{\mu_c} \propto \hat{q}_a$ in Eq. (1.10), so that local mode a directly interacts with the electric field and local mode b is dark. This model can be characterized by the mass ratio $\gamma_m \equiv m_b/m_a$, the frequency ratio $\gamma_\omega \equiv \omega_b/\omega_a$, $\beta\hbar\omega_a$, and the intermode bilinear coupling c_{ab}. The chromophore a is taken to be a Morse oscillator with dimensionless well depth βD_a and harmonic frequency ω_a and mode b is taken to be either a harmonic oscillator or a second Morse oscillator with anharmonicity defined by βD_b.

OMT results are compared to quantum mechanical calculations computed in the basis of harmonic product states using 15 eigenfunctions per mode. OMT results were computed using the fixed-trajectory implementation presented in Sec. 3.2. Initial coordinates and momenta were approximated using action-angle perturbation theory,[56] reviewed in Appendix A. Corrections to the harmonic action-angle solutions of the normal mode coordinates and momenta were treated to second order in cubic anharmonicity and to first order in quartic anharmonicity. Initial actions for each oscillator were varied between $\hbar/2$ and $5\hbar/2$ in steps of $\hbar$, requiring 58 classical trajectories in which the normal mode actions vary between $\hbar/2$ and $4\hbar$ in steps of $\hbar/2$. The angle sampling portion of the trajectory is of length $t_{\text{ang}} = 4000\omega_a^{-1}$ with step size of $1.5\omega_a^{-1}$ between discrete states and the propagation portion of the trajectory is of length $t_{\text{prop}} = 6000\omega_a^{-1}$. Initial angle values were chosen from a uniform probability distribution. The statistical weight of each diagram, ΔF, in Eq. (2.23) was not renormalized to account for quantization in computing spectra in this section. This results in discrepancies in the absolute intensities of the quantum mechanical and OMT spectra, which are not compared. Because the action and angle variable solutions are approximate, varying the angles used to initialize the fixed trajectories causes small amplitude changes and frequency shifts in the calculated spectra. Increasing anharmonicity

and allowing γ_ω to approach one increases the size of these variations, due to the decreasing accuracy of the perturbation theory results.

We calculate the response functions for the two phase-matched directions associated with the wavevectors, $\mathbf{k}_{\mathrm{I}} = -\mathbf{k}_1 + \mathbf{k}_2 + \mathbf{k}_3$ and $\mathbf{k}_{\mathrm{III}} = \mathbf{k}_1 + \mathbf{k}_2 - \mathbf{k}_3$. The dependence of each of these response functions on the propagation times t_1, t_2, and t_3 may be qualitatively interpreted by expressing each response function as a sum of 2FDs as in Fig. 2.1 and considering each 2FD in the harmonic limit. For both signals, during t_1 and t_3 one oscillator evolves in a one-quantum coherence and the other oscillator evolves in a population. In the $\mathbf{k}_{\mathrm{I}}$ signal, each oscillator evolves in a population during the t_2 waiting time, while the $\mathbf{k}_{\mathrm{III}}$ signal has contributions from two distinct processes during the waiting time. If both normal modes interact with the electric field, as in the OMT diagrams in panels (b)-(d) of Fig. 2.6, then both modes will evolve as populations. If the radiation only interacts directly with one normal mode as in Fig. 2.6(aii), then that mode will evolve in a two-quantum coherence during the waiting time and the other mode will evolve as a population. The contribution from the latter diagrams is expected to dominate the $\mathbf{k}_{\mathrm{III}}$ t_2-dependence for the present model since these diagrams display appreciable dynamics, even in the harmonic limit.

Results are displayed as the absolute square of the one-sided Fourier transform of the response function with respect to $t_1 = t_3 = t$ in Fig. 4.6 and with respect to t_2 in Fig. 4.7. The model defined in Eq. (4.3) has neither dissipation nor static disorder so apparent linewidths are an artifact of computing the Fourier transform over a finite time interval. Therefore, peak areas were computed to better compare relative frequency contributions. In all figures, each spectrum is scaled so that the dominant peak has unit area. Quantum mechanical peak areas are shown as gray

circles and OMT peak areas are shown as green dots. The frequency range in each plot was chosen to show the dominant contributions to the signal. The response function for a particular phase-matching condition, $R^{(3)}_{\gamma\beta\alpha}(t_3, t_2, t_1)$ in Eq. (1.10), is complex-valued and the absolute square of its Fourier transform with respect to time arguments need not be even in frequency. Both positive and negative frequencies are shown for the $\mathbf{k}_{\mathrm{I}}$ signal in Fig. 4.6. In all other figures, only positive frequencies are shown either because the signal is nearly symmetric in frequency, as for the $\mathbf{k}_{\mathrm{I}}$ signal in Fig. 4.7, or because there is no significant contribution at negative frequencies, as for the $\mathbf{k}_{\mathrm{III}}$ signal in Figs. 4.6 and 4.7.

Column (i) of Fig. 4.6 shows the absolute square of the Fourier transform of $R^{(3)}_{\mathrm{I}}(t, 0, t)$, the vibrational echo signal, and column (ii) shows the absolute square of the Fourier transform of $R^{(3)}_{\mathrm{III}}(t, 0, t)$. Numerically exact quantum spectra are shown as gray dashed lines and OMT results are given with solid green lines. In rows (a)-(c), the bright Morse oscillator is coupled to a harmonic oscillator with $\beta D_a = 40$, $\beta\hbar\omega_a = 2$, $\gamma_m = 1$, with different coupling constants, c_{ij} as defined in Eq. (4.3). In row (a) $c_{ab} = 0$, reproducing the signal for a thermal ensemble of noninteracting Morse oscillators in Fig. 4.5(a) and (c). The dominant peak in the $\mathbf{k}_{\mathrm{I}}$ signal in panel (ai) is at $-\Delta_{\mathrm{anh}}$, with $\Delta_{\mathrm{anh}} = \hbar\omega_a^2/2D_a$ the anharmonic frequency of a Morse oscillator. Row (b) shows calculations for coupled oscillators, with $c_{ab} = 0.05$ and $\gamma_\omega = 0.9$. For the $\mathbf{k}_{\mathrm{I}}$ signal in panel (bi), coupling shifts the dominant peak to lower absolute frequency and introduces smaller amplitude peaks. The second largest frequency contribution, for example, is the first overtone of the anharmonic frequency. Both the frequency shift and appearance of this secondary frequency are reproduced by the OMT calculation. For the $\mathbf{k}_{\mathrm{III}}$ signal in panel (bii), the primary effect of the coupling on the quantum response is to introduce frequency shifts, which are also present in the OMT result. In row

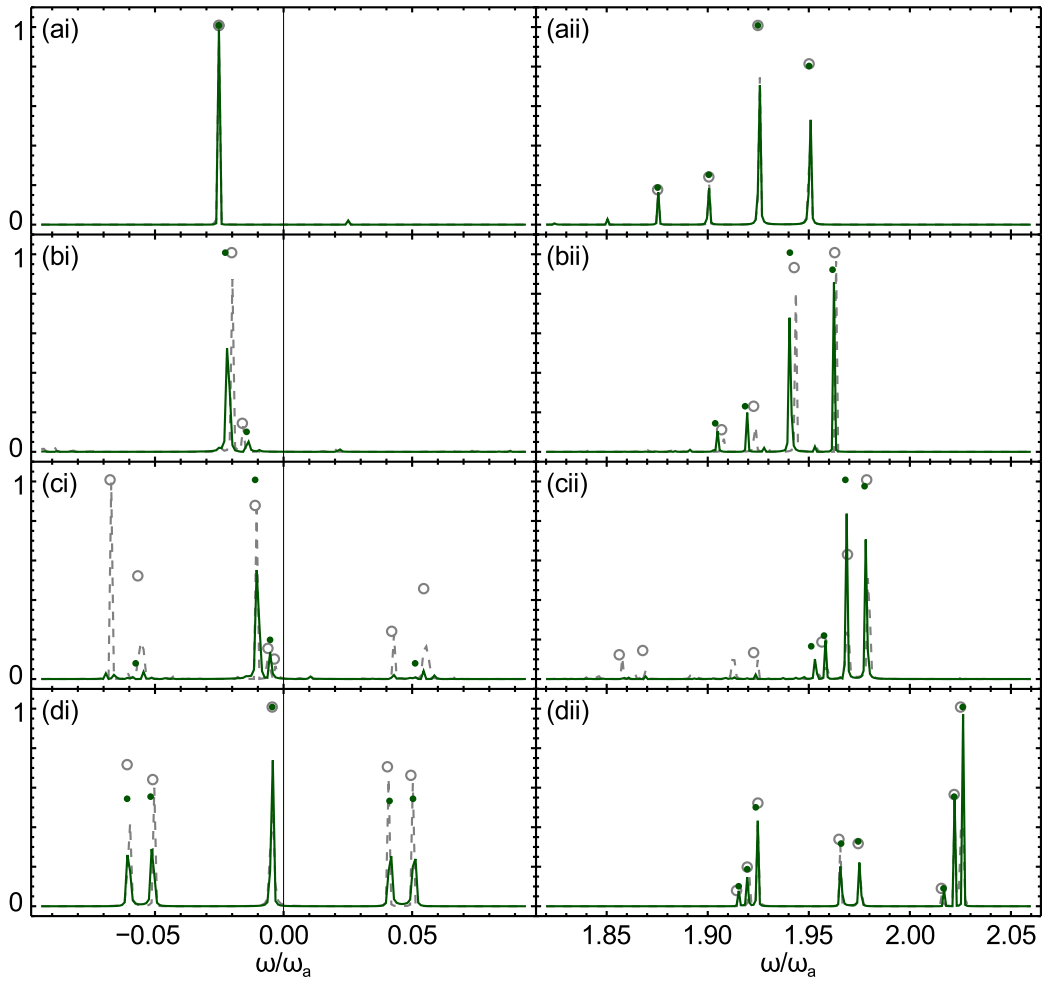

Figure 4.6: $\left|\tilde{R}^{(3)}_{\mathrm{I}}(t,0,t)\right|^2$ and $\left|\tilde{R}^{(3)}_{\mathrm{III}}(t,0,t)\right|^2$ are shown in columns (i) and (ii), respectively. Row (a) shows results for a thermal ensemble of Morse oscillators with $\beta D_a = 40$ and $\beta\hbar\omega_a = 2$. Rows (b) and (c) show results for a thermal ensemble of Morse oscillators, described by the same parameters as in (a), each coupled to a dark harmonic oscillator with $\gamma_m = 1$ and $c_{ab} = 0.05$. In row (b) $\gamma_\omega = 0.9$ and in row (c) $\gamma_\omega = 0.95$. Row (d) shows spectra for a thermal ensemble of two bilinearly coupled Morse oscillators with $\beta D_a = \beta D_b = 410$, $\beta\hbar\omega_a = 8$, $\gamma_m = 1$, $\gamma_\omega = 0.994$, and $c_{ab} = 0.05$. Quantum calculations are shown as gray dashed lines, with peak areas indicated by gray circles and OMT results are in green, with peak areas indicated by green dots.

(c), the coupling $c_{ab} = 0.05$ is maintained, but the interaction is increased by bringing the oscillators closer to resonance with $\gamma_\omega = 0.95$. Comparing to the uncoupled results in row (a), the effects of the coupling are more pronounced in row (c) than in row (b). The OMT does not reproduce all peak amplitudes, but does show many features characteristic of the oscillators' interaction present in the quantum results. For example, the frequency shifts in Fig. 4.6(ci) and (cii), relative to panel (a), are well reproduced. However, the appearance of two pairs of peaks near $-0.05\omega_a$ and $0.05\omega_a$, generated predominantly by diagrams corresponding to two interactions with each normal mode, is not well reproduced by the OMT results. The parameters used in rows (a)-(c) of Fig. 4.6 correspond at room temperature to oscillators of relatively low frequency and high anharmonicity. Row (d) shows calculations more appropriate to high frequency modes at room temperature. Signals are shown for two interacting Morse oscillators, with $\beta D_a = \beta D_b = 410$, $\beta\hbar\omega_a = 8$, $\gamma_m = 1$, $\gamma_\omega = 0.994$, and $c_{ab} = 0.05$. At room temperature, these parameters correspond to a local mode frequency of approximately 1650 cm^{-1} and an anharmonicity, $\Delta_{\text{anh}} \approx 16$ cm^{-1}, roughly the frequency and anharmonicity characterizing a peptide unit in an amide I mode.[14] The OMT well reproduces the effects of interactions in Fig. 4.6(di) and (dii). Signal contributions near $-0.05\omega_a$ and $0.05\omega_a$, are reproduced in the OMT result in Fig. 4.6(di) and the relative frequency contributions in the quantum results are well reproduced by the OMT, particularly in Fig. 4.6(dii).

The waiting time dependence of the response function is examined in Fig. 4.7, which shows the absolute square of the Fourier transforms of $R_{\text{I}}^{(3)}(5,t,0)$ in column (i) and of $R_{\text{III}}^{(3)}(5,t,0)$ in column (ii). The parameters are the same as in each corresponding panel of Fig. 4.6. For uncoupled oscillators in panel (ai), the $\mathbf{k}_{\text{I}}$ signal is not well reproduced by the OMT approximation. All contributions to this

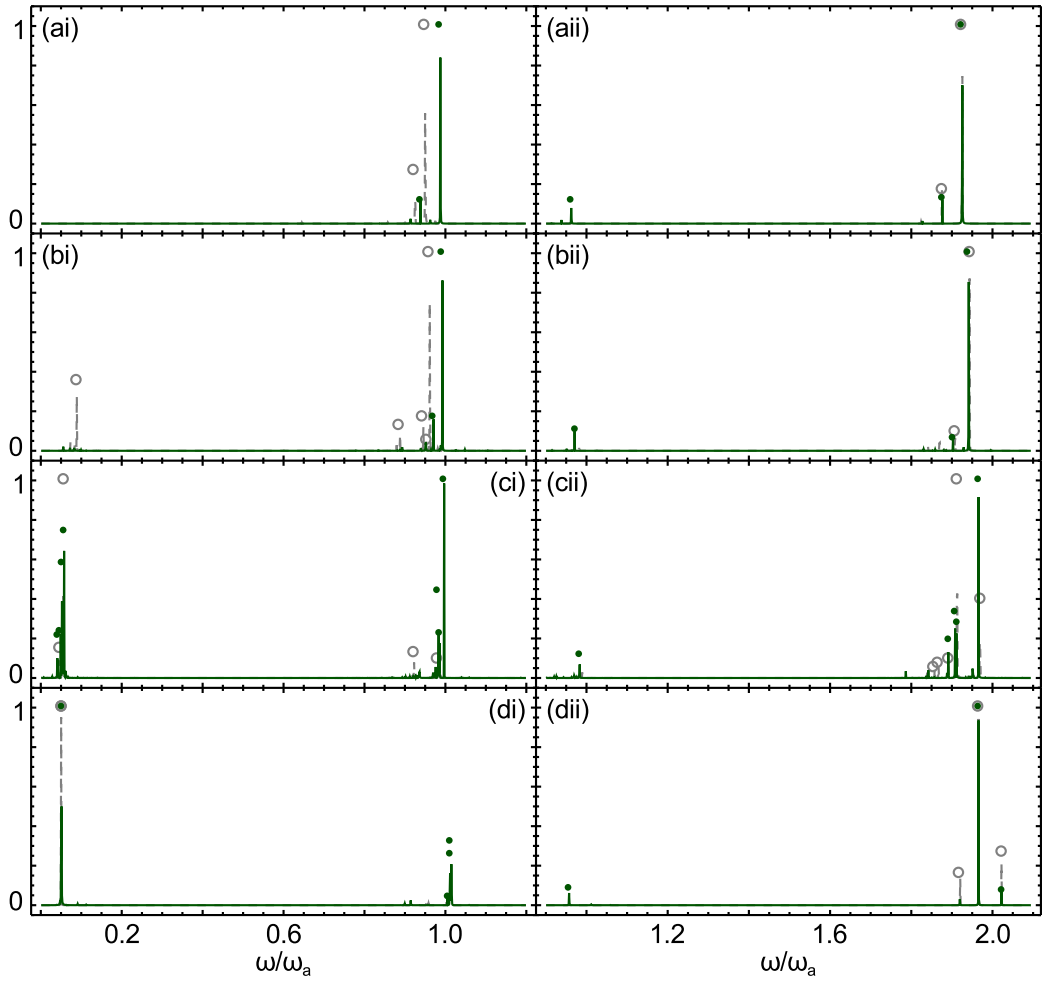

Figure 4.7: $\left|\tilde{R}_{\mathrm{I}}^{(3)}(5,\omega,0)\right|^2$ and $\left|\tilde{R}_{\mathrm{III}}^{(3)}(5,\omega,0)\right|^2$ are shown in columns (i) and (ii), respectively, for the same parameters as in the corresponding panels of Fig. 4.6.

signal result from transitions forbidden under harmonic selection rules and hence occur at relatively low amplitude, which is not apparent in the figure because of normalization. When coupling is introduced in panel (bi), low frequency peaks appear in the quantum response corresponding to coherence oscillation between the modes. For a harmonic system this frequency corresponds to the difference in the one-quantum coherence frequencies of the normal modes, or approximately 0.11 for these parameters. The quantum response shows a peak shifted to lower frequency, indicating the effects of anharmonicity. The OMT does not reproduce the amplitude of these peaks in panel (bi), but does show small contributions to

the system response near this frequency. In panel (ci), the frequency corresponding to coherence oscillation during the waiting time is dominant in the quantum calculation and there are larger amplitude contributions to the response near this frequency in the OMT result. Near the dominant peak in the quantum result at approximately $0.055\omega_a$ the OMT spectra shows two nearly resonant features. For the lower anharmonicity system in panel (di), the OMT well reproduces the $\mathbf{k}_{\mathrm{I}}$ signal.

The OMT and quantum calculations in panel (aii) in Fig. 4.7 are in good agreement, showing that for a single anharmonic oscillator, the OMT can well describe the time-evolution of two-quantum coherences. When the interaction between the oscillators is introduced in panel (bii) and increased in panel (cii), the OMT well reproduces the frequency shifts relative to the uncoupled case, although the dominant quantum peak in panel (cii) is again split into two near resonant peaks in the OMT response.

In this section, the FT implementation of the OMT was tested on thermal ensembles of pairs of interacting oscillators, with a bright anharmonic local mode coupled to a dark mode that was either harmonic or anharmonic. The responses associated with four-wave-mixing signals in phase-matched directions $-\mathbf{k}_1+\mathbf{k}_2+\mathbf{k}_3$ and $\mathbf{k}_1+\mathbf{k}_2-\mathbf{k}_3$ were determined, and dynamics of all time arguments of $R^{(3)}_{\gamma\beta\alpha}(t_3,t_2,t_1)$ were considered. The OMT approximation well reproduced both the dynamics of one-quantum and two-quantum coherences and the dynamics of coherence oscillation during the waiting time. The OMT approximation did particularly well at reproducing the quantum spectra for low anharmonicity vibrations with parameters similar to those that would be found in an amide I vibration. As the interaction between the modes was increased, either by increasing the coupling

term in the potential energy or by making the local mode frequencies more similar, the OMT calculation became less accurate. These trends are expected as the derivation of the OMT and its approximate implementation rely on the evolution of perturbative corrections to the harmonic normal modes well approximating the evolution of quantum mechanical eigenstates.

Chapter 5

Results for System-Bath Models

We present results for a single oscillator coupled to a bath in Sec. 5.1 and for two near-resonant oscillators coupled to a bath in Sec. 5.2. The purely absorptive spectrum,[5,43] $R_{\rm abs}(\omega_3, \omega_1; t_2)$, obtained by combining the rephasing and nonrephasing responses, defined in Eq. (1.11) and discussed in Chapter 1, is the primary result computed.

In both sections, the bath coupling coefficients and frequencies are defined to be consistent with a specified spectral density, $J(\omega) \equiv \sum_j c_j^2/(2m_j\omega_j)\delta(\omega - \omega_j)$. We take $J(\omega)$ in the continuum limit to be Ohmic with a Lorentzian cutoff[43]

$$J(\omega) = \frac{\eta}{\pi}\frac{\gamma^2\omega}{\gamma^2 + \omega^2} \tag{5.1}$$

where γ controls the width of $J(\omega)$ and η is the classical friction coefficient. This continuous distribution is approximated by a discrete bath of $N_{\rm B}$ oscillators with linearly spaced frequencies, $\omega_j = (j-1)\Omega/(N_{\rm B}-1)$, and maximum frequency Ω by taking the coupling constants c_j to be[76]

$$\frac{c_j^2}{m_j\omega_j^2} = \frac{2\eta\Omega}{\pi(N_{\rm B}-1)}\frac{\gamma^2}{\gamma^2+\omega_j^2} \quad j = 2, 3, \cdots, N_{\rm B}-1 \tag{5.2}$$

To better approximate a continuous bath, ω_1 is taken to be a zero frequency mode[76] which contributes a frequency shift to the chromophore. The coupling coefficients of this zero frequency mode and of mode $N_{\rm B}$ with frequency Ω are given by half the right side of Eq. (5.2).

5.1 One Oscillator with a Bath

In this section, we treat a single chromophore mode a coupled to a bath of harmonic oscillators[77–79] as defined by the quantum Hamiltonian,

$$\hat{H} = \hat{H}_a + \sum_{j=1}^{N_\mathrm{B}} \frac{\hat{p}_j^2}{2m_j} + \frac{m_j\omega_j^2}{2}\left(\hat{q}_j - \frac{c_j V(\hat{q}_a)}{m_j\omega_j^2}\right)^2. \tag{5.3}$$

Here $\hat{H}_a$ is the chromophore Hamiltonian, m_j and ω_j are the mass and frequency of bath mode j, and c_j quantifies the coupling between mode j and the chromophore. The dependence of the coupling on the chromophore coordinate is determined by $V(\hat{q}_a)$, which has dimensions of length. We will consider this function up to second order in chromophore coordinate[43]

$$V(\hat{q}_a) = v_\mathrm{LL}\hat{q}_a + \frac{v_\mathrm{SL}}{2}\hat{q}_a^2, \tag{5.4}$$

with v_LL and v_SL quantifying linear-linear (LL) and square-linear (SL) coupling, respectively. We describe the chromophore-bath coupling in terms of the dimensionless parameters $\nu_\mathrm{LL} = v_\mathrm{LL}\left(\eta/m_a\omega_a\right)^{1/2}$ and $\nu_\mathrm{SL} = v_\mathrm{SL}\left(\eta\hbar/m_a^2\omega_a^2\right)^{1/2}$.

Defining the overlap of normal mode i with the chromophore mode a by κ_{ai} in the expansion, $q_a = \sum_{i=1}^{N_{\mathrm{B}+1}} \kappa_{ai}x_i$, only one normal mode will have significant overlap with the chromophore for the couplings investigated here. We will refer to this mode as the 'system' normal mode labeled 1 and to the other N_B modes as 'bath' normal modes. Because $\kappa_{a1}^2 \gg \kappa_{ar}^2$ for $r \neq 1$ the OMT calculation in Eq. (2.21) can be greatly simplified,

$$R^{(3)}_{\gamma\beta\alpha}(t_3,t_2,t_1) \approx \kappa_{a1}^4 \rho^1_{\gamma\beta\alpha}(t_3,t_2,t_1). \tag{5.5}$$

Within this approximation only action jumps in the system normal mode are allowed. This approximation corresponds to computing contributions to the two-dimensional spectrum from the diagonal peak near the fundamental frequency of

the system normal mode and the peaks associated with overtone transitions in this mode.

OMT results are computed using the FB implementation described in Sec. 3.3. The required canonical transformation between normal modes and action-angle variables is approximated using perturbation theory, as described in Appendix A, to zeroth order in the anharmonic couplings involving bath normal modes and to first order in cubic anharmonicity for the system normal mode. Following the third interaction with the field, values of $\mathbf{z}_3$ are computed by numerically inverting the perturbative coordinate and momentum expressions to determine $\boldsymbol{\phi}_2(t_2) = \boldsymbol{\phi}_3$, assuming the actions are unchanged during the trajectories. The statistical weight in Eq. (3.3) is approximated by $\Delta F(\mathbf{z}_1(t_1)) \approx F(\mathbf{z}_1(t_1))|_{J_1^1 \to J_1^1 - \hbar/2}$, which is valid for $\beta\hbar\omega_1 \gtrapprox 1$. In sampling initial actions, the dependence of the full Hamiltonian on action variables is approximated as a sum of uncoupled contributions with the system mode treated perturbatively to second order in cubic anharmonicity and the bath modes treated harmonically. All trajectories used to compute diagrams with a given set of initial actions, $\mathbf{J}_1$, are initiated with the same set of initial angle values.

Quantum calculations of purely absorptive spectra for the continuum limit of this model were performed by Ishizaki and Tanimura[43] using a quantum Fokker-Planck equation approach.[80,81] Our semiclassical results are compared qualitatively to these quantum calculations. OMT results are also compared to the widely applied fluctuating-frequency approximation,[82,83] where the effect of the bath interaction is approximated by Gaussian fluctuations in the chromophore frequency. This approximation is expected to be valid for weak coupling to an off-resonance bath.[43] The rephasing response associated with wavevector $\mathbf{k}_\mathrm{I} = -\mathbf{k}_1 + \mathbf{k}_2 + \mathbf{k}_3$

and the nonrephasing response associated with wavevector $\mathbf{k}_{\rm II} = \mathbf{k}_1 - \mathbf{k}_2 + \mathbf{k}_3$ for this approximation are,[5,11,43,72]

$$R_{\rm I}^{(3)}(t_3,t_2,t_1) \approx \left(\frac{i}{\hbar}\right)^3 \left(2\mu_{10}^4 - \mu_{10}^2\mu_{21}^2 e^{i\Delta_{\rm anh}t_3}\right) e^{-i\omega_{10}(t_3-t_1)} e^{-g(t_3)-g(t_1)+f(t_3,t_2,t_1)} \tag{5.6}$$

$$R_{\rm II}^{(3)}(t_3,t_2,t_1) \approx \left(\frac{i}{\hbar}\right)^3 \left(2\mu_{10}^4 - \mu_{10}^2\mu_{21}^2 e^{i\Delta_{\rm anh}t_3}\right) e^{-i\omega_{10}(t_3+t_1)} e^{-g(t_3)-g(t_1)-f(t_3,t_2,t_1)} \tag{5.7}$$

with,

$$g(t) = \int_0^t d\tau \int_0^\tau d\tau' C_{\omega\omega}(\tau'), \tag{5.8}$$

$$f(t_3,t_2,t_1) = g(t_2) - g(t_2+t_1) - g(t_3+t_2) + g(t_3+t_2+t_1). \tag{5.9}$$

We treat the dipole matrix elements, μ_{10} and μ_{21}, in Eqs. (5.6) and (5.7) in the harmonic limit so that $\mu_{10} = \sqrt{\hbar/(2m_a\omega_a)}$ and $\mu_{21} = \sqrt{2}\mu_{12}$. Within the approximations of Eqs. (5.6)-(5.9) the rephasing and nonrephasing response functions are determined by the frequency autocorrelation function $C_{\omega\omega}(t) \equiv \langle \delta\omega_{10}(t)\delta\omega_{10}(0)\rangle$. In the present model this autocorrelation function is given in terms of the classical friction kernel $\eta(t)$ for $v_{\rm LL} = 1$ as

$$C_{\omega\omega}(t) = \frac{k_{\rm B}T}{4\eta\hbar}\left(\nu_{\rm SL} + 3\sqrt{\frac{\hbar\omega_a}{2D}}\nu_{\rm LL}\right)^2 \eta(t)\left(\sum_j \frac{c_j^2}{m_j\omega_j^2}\cos\omega_j t\right) \tag{5.10}$$

This is the discrete bath analog of the results in Eqs. (2.15) and (3.18b) of Ref. 43 for a continuum bath, with coordinate matrix elements evaluated to lowest order in anharmonicity. In Sec. 5.1.1 we treat a low frequency bath within these approximations and in Sec. 5.1.2 we treat a weakly coupled near-resonant bath.

5.1.1 Low Frequency Bath using FB Implementation

In this section purely absorptive spectra are shown for bath parameters in the pure dephasing regime in which the fluctuating-frequency approximation is expected to accurately reproduce the response.[43] We treat the Hamiltonian in Eq. (5.3), with the chromophore mode a taken to be a Morse oscillator defined by dimensionless parameters, $\beta D = 391$ and $\beta\hbar\omega_a = 7.75$. Here D is the Morse oscillator well depth and ω_a is the harmonic frequency of local mode a. For the fundamental frequency $\omega_{10} = \omega_a - \Delta_{\text{anh}} = 1600\ \text{cm}^{-1}$ at 300 K this corresponds to anharmonicity $\Delta_{\text{anh}} = \hbar\omega_a^2/2D = 16\ \text{cm}^{-1}$. These parameters are appropriate to describe the amide I band[14,84] and are used in Ref. 43. The width of the spectral density in Eq. (5.1) is taken to be $\gamma = 4.95 \times 10^{-3}\omega_a$, with $N_{\text{B}} = 21$ and maximum bath frequency $\Omega = 0.02\omega_a$.

In Fig. 5.1 we treat the system with bilinear coupling with $\nu_{\text{LL}} = 1.41$ and $\nu_{\text{SL}} = 0$. These parameters correspond to a finite bath version of the quantum calculation in Fig. 5(a-i) of Ref. 43. Purely absorptive spectra for the fluctuating-frequency approximation are shown in row (a) and for the OMT approximation using 5000 initial conditions in row (b). Columns (i)-(iii) show spectra for $\omega_a t_2 = 0$, 150, and 1200, respectively. For typical amide I vibrational frequencies[14,84] the waiting times in columns (ii) and (iii) correspond to approximately 0.5 and 4 ps, respectively. The fluctuating-frequency approximation spectrum at $t_2 = 0$ in Fig. 5.1(ai) shows diagonal elongation, indicating inhomogeneous broadening that is characteristic of waiting times short relative to relaxation time scales. The bath-induced broadening present in the OMT spectrum at $t_2 = 0$ in panel (bi) qualitatively agrees with the fluctuating-frequency result in (ai). In addition to broadening, the OMT result shows a bath-induced shift in the center of both peaks

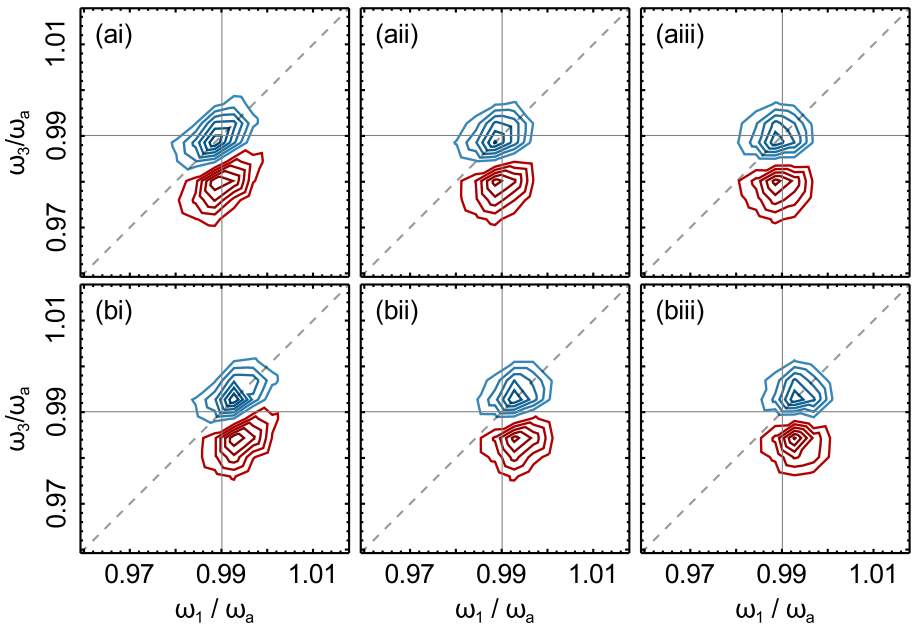

Figure 5.1: $R_{\mathrm{abs}}(\omega_3, \omega_1; t_2)$ is shown for an anharmonic oscillator interacting bilinearly with a medium. Row (a) shows results of the fluctuating-frequency approximation and OMT results are shown in row (b). Spectra are shown for $\omega_a t_2 = 0$ in column (i), $\omega_a t_2 = 150$ in column (ii), and for $\omega_a t_2 = 1200$ in column (iii). Results for each approximation are normalized to the maximum absolute value at $t_2 = 0$. Six contours equally spaced between -1 and 0 and between 0 and 1 are shown, with negative contours in blue and positive in red.

to higher frequency. This shift is also present in the quantum results of Ref. 43, but absent in the fluctuating-frequency result in Fig. 5.1(ai). The frequency shift in the $t_2 = 0$ spectra is also present at later t_2 times in column (ii) and (iii). As the waiting time is increased, changes in the relative contributions of the rephasing and nonrephasing responses cause the peaks to become more symmetric, indicating homogeneous broadening. Both the degree of broadening and the crossover between diagonally broadened and symmetric peaks are accurately reproduced by the OMT results as seen from comparison of the two rows in Fig. 5.1. The t_2-dependence was not considered in Ref. 43, so no comparison to quantum mechanical results is made. In the pure dephasing limit, all broadening from LL coupling is a result of the system anharmonicity, as is evident in Eq. (5.10) where the LL term

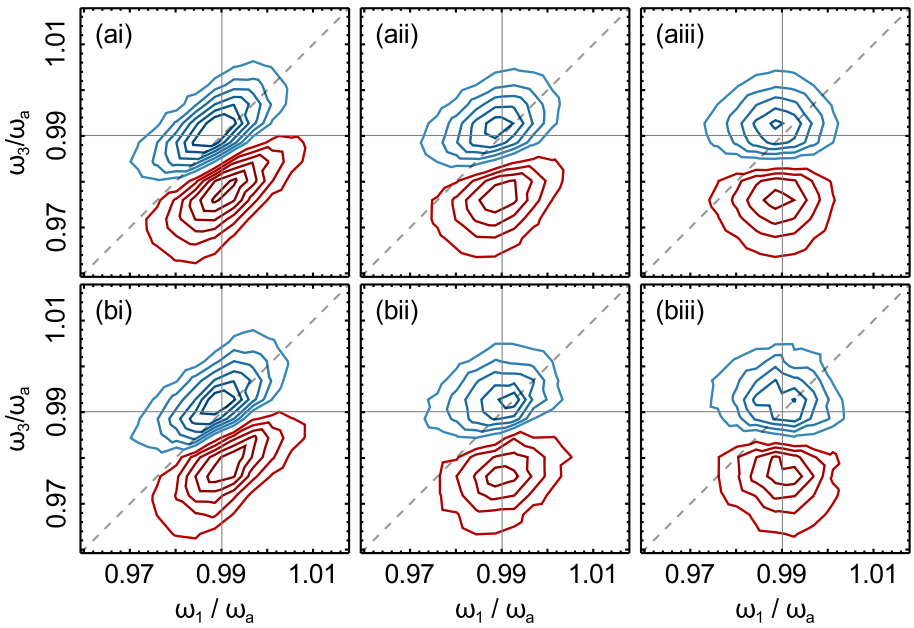

Figure 5.2: Purely absorptive spectra are shown for the same parameters as in Fig. 5.1 but with quadratic coupling, $\nu_{\mathrm{LL}} = 0$, $\nu_{\mathrm{SL}} = 0.704$. Fluctuating-frequency approximation results are shown in row (a) and OMT results in row (b). The t_2 values are the same as in Fig. 5.1.

is proportional to $D^{-1/2}$. Accurately reproducing the broadening present in the fluctuating-frequency approximation demonstrates that important anharmonic effects are incorporated into the OMT description by propagating trajectories with the full Hamiltonian.

In Fig. 5.2, the calculations in Fig. 5.1 are repeated for chromophore-bath coupling that is quadratic in the chromophore coordinate, $\nu_{\mathrm{LL}} = 0$, $\nu_{\mathrm{SL}} = 0.704$. These correspond to the coupling parameters used in Fig. 5(a-ii) of Ref. 43. The OMT results in Fig. 5.2(b) were computed using 35,000 initial conditions, although qualitative features were apparent with a few thousand initial conditions. The waiting time dynamics of the spectra in Fig. 5.2 are qualitatively similar to the dynamics in the LL coupling case. At $t_2 = 0$ peaks show inhomogeneous broadening, and become homogeneously broadened as the waiting time increases. There is greater line broadening for the SL coupling in Fig. 5.2 than for the LL coupling shown

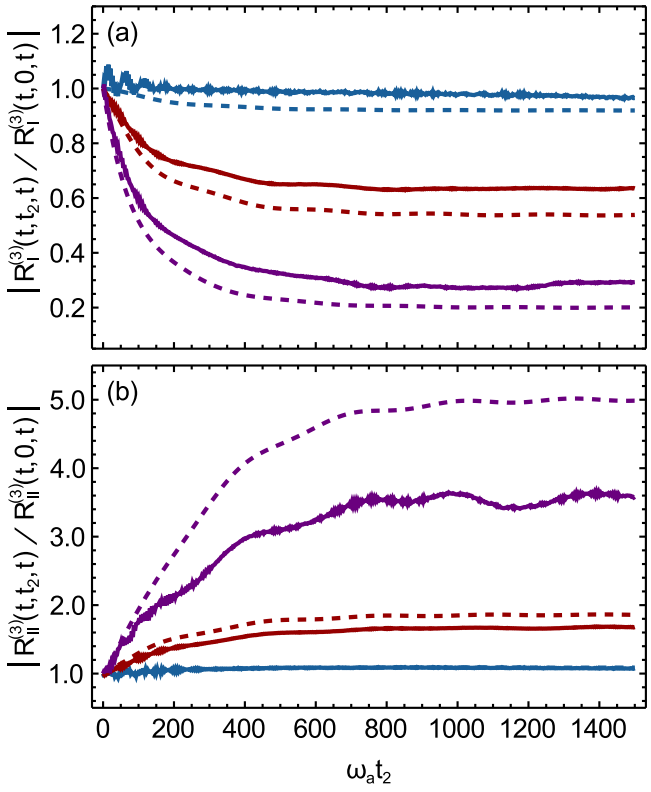

Figure 5.3: $\left|R^{(3)}_{\mathrm{I/II}}(t,t_2,t)/R^{(3)}_{\mathrm{I/II}}(t,0,t)\right|$ is shown for the same parameters as in Fig. 5.2. The rephasing response is shown in panel (a) and the nonrephasing response in panel (b). Three $t = t_1 = t_3$ values are shown in each panel: $\omega_a t =$ 30(blue), 90(red), and 180(purple). Fluctuating-frequency approximation results are shown with dashed lines and OMT results with solid lines.

in Fig. 5.1, in agreement with the $t_2 = 0$ calculations in Ref. 43. The OMT approximation reproduces the line shapes of the fluctuating-frequency approximation including the decay in the peak amplitude as a function of t_2 as well as the degree of dephasing relative to the LL case. Unlike LL coupling terms, anharmonic SL coupling terms do not enter in determining normal modes. The SL coupling terms are only incorporated in the OMT approximation through their presence in the full Hamiltonian used to propagate trajectories. The results in Fig. 5.2 again demonstrate the capacity of the OMT to reproduce anharmonic effects, even when action-angle variables are crudely approximated.

We further investigate the waiting time dynamics predicted by the OMT approximation in Fig. 5.3 which shows the waiting time dynamics of the absolute value of the rephasing response in panel (a) and of the nonrephasing response in panel (b) for the same parameters as Fig. 5.2. All signals in Fig. 5.2 are normalized to the maximum absolute value in their corresponding $t_2 = 0$ spectra. Fluctuating-frequency results are shown as dashed lines and OMT results are shown as solid lines. Three values of $t = t_1 = t_3$ are shown for each signal, $\omega_a t = 30$(blue), 90(red), and 180(purple). For a fundamental transition frequency of 1600 cm^{-1} these values correspond to approximately 100, 300, and 600 fs, respectively. This is a rigorous test of the OMT since all t_2-dynamics of the response functions in Fig. 5.3 are the result of chromophore-bath couplings. The fluctuating-frequency approximation rephasing responses in panel (a) show an overall decay with waiting time, with greater relative decay for larger $\omega_a t$ values. The rephasing and nonrephasing signals in panels (a) and (b) are reciprocals in the fluctuating-frequency approximation, so that the nonrephasing results show corresponding increases with waiting time. The OMT results share these features. Relative to the fluctuating-frequency approximation, the OMT results consistently show less decay in the rephasing signal and smaller increases in the nonrephasing signal, so that the OMT results in panels (a) and (b) are also approximately reciprocals. In panel (b) qualitatively similar small amplitude oscillations, caused by the finite bath, are apparent in both results, especially for $\omega_a t = 180$ shown in purple. Results in Ref. 43 were computed at $t_2 = 0$ so no comparison to quantum calculations is made.

In the pure dephasing limit of a weakly-coupled off-resonance bath, our results agree both with the fluctuating-frequency approximation, established to work well in this limit, and with the quantum calculations of Ishizaki and Tanimura[43] for both forms of chromophore-bath interactions. While this weak-coupling limit is theoret-

ically simple, it poses a significant numerical challenge for the OMT. First, there is a large disparity in frequency scales, one of the challenges that motivated the development of the FB implementation. Second, achieving correct time-dependences of the response function requires extensive averaging over initial conditions and adequate treatment of transitions in system action at constant angle variables.

5.1.2 High Frequency Bath using FB Implementation

In Sec. 5.1.1 OMT results were compared to results computed within the fluctuating-frequency approximation in the pure dephasing regime, in which the fluctuating-frequency approximation is expected to accurately reproduce the response function. This approximation is not expected to well describe broadening in the motional narrowing regime.[43] Figure 5.4 shows purely absorptive spectra for such a model, where the width of the bath spectral density has been increased relative to that of Figures 5.1-5.3 and the chromophore-bath coupling is bilinear, facilitating single quantum excitation transfer between the system and bath. The bath parameters are given by $\gamma = 9.90\times10^{-2}\omega_a$, $N_{\rm B} = 126$ and $\Omega = 1.4654\omega_a$, with the maximum bath frequency chosen to avoid resonances with the chromophore mode. The coupling parameters are $\nu_{\rm LL} = 0.222$ and $\nu_{\rm SL} = 0$. These are the same coupling strengths used in Fig. 3(i) of Ref. 43 but here the width of the spectral distribution is a factor of 5 smaller to reduce the number of oscillators in the finite bath. Fluctuating-frequency results are shown in panel (a) and OMT results computed from 5000 initial conditions are shown in panel (b). Spectra are shown at $\omega_a t_2 = 0$, 150, and 1200 in columns (i)-(iii), respectively. Time-domain results were not fully decayed so, to reduce artifacts[85] caused by taking the discrete Fourier transform of aperiodic data, the response functions used to compute Figs. 5.4 and

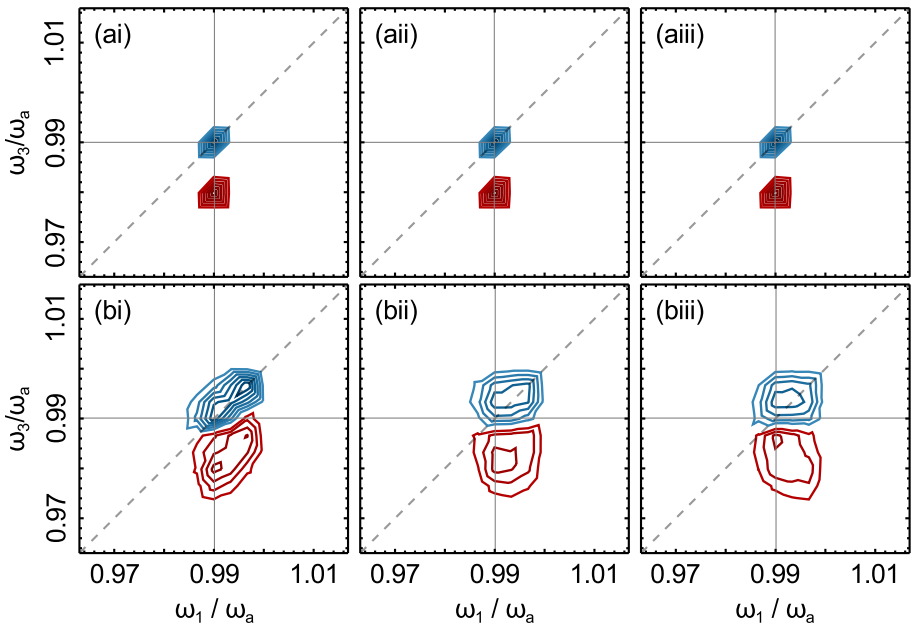

Figure 5.4: $R_{\mathrm{abs}}(\omega_3, \omega_1; t_2)$ for a thermal ensemble of Morse oscillators with bilinear coupling to a harmonic bath is shown as a function of $\omega_a t_2$. Fluctuating-frequency approximation results are shown in panel (a) and OMT results are shown in panel (b). Spectra at $\omega_a t_2 = 0$ are shown in row (i), at $\omega_a t_2 = 150$ in column (ii), and at $\omega_a t_2 = 1200$ in column (iii). All spectra are normalized to the maximum absolute value at $t_2 = 0$. Six contours equally spaced between -1 and 0 and between 0 and 1 are shown, with negative contours in blue and positive in red.

5.5 were multiplied by the product of one-sided cosine-squared window functions for the t_1 and t_3 time variables, $\sin\left(\frac{n_\tau+1+n}{2(n_\tau+1)}\pi\right)^2$ with $n = 1, 2, \ldots n_\tau$, with n_τ the number of times sampled during the τ trajectory. Applying this window function to the time-domain results used to compute Figures 5.1 and 5.2 did not result in significant additional broadening.

In row (a) of Fig. 5.4 the fluctuating-frequency approximation results show no significant broadening or waiting time dynamics at the figure resolution. This indicates minimal pure dephasing for this set of parameters. In contrast, the OMT results in column (b) show significant line broadening. At $t_2 = 0$ the OMT result in Fig. 5.4(bi) shows inhomogeneous broadening, while both peaks at finite t_2 are homogeneously broadened. Figure 5.5 shows fluctuating-frequency and OMT

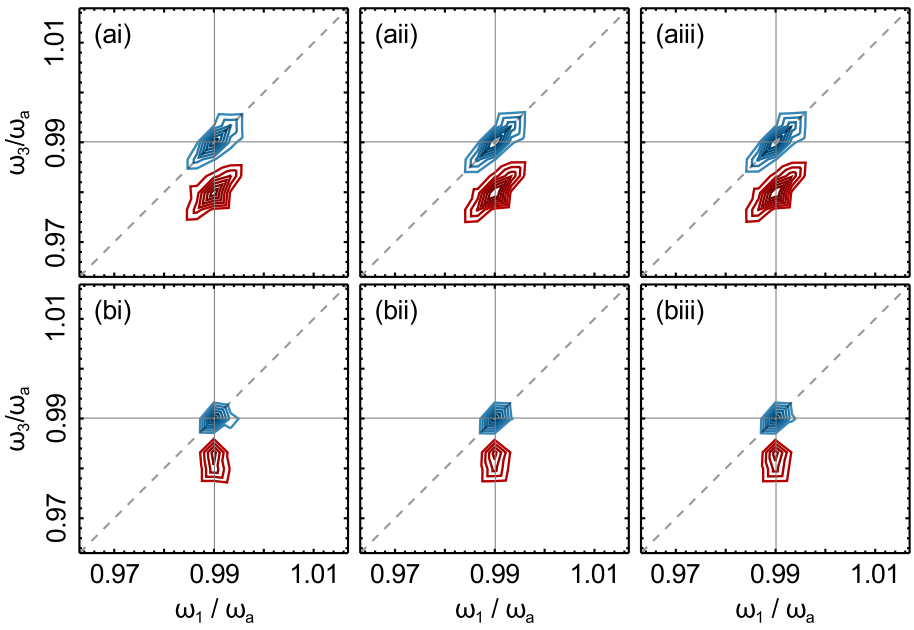

Figure 5.5: $R_{\mathrm{abs}}(\omega_3, \omega_1; t_2)$ for a thermal ensemble of Morse oscillators with square-linear coupling to a harmonic bath is shown as a function of $\omega_a t_2$. Fluctuating-frequency approximation results are shown in panel (a) and OMT results computed from 500 initial conditions are shown in panel (b). Spectra at $\omega_a t_2 = 0$ are shown in row (i), at $\omega_a t_2 = 150$ in column (ii), and at $\omega_a t_2 = 1200$ in column (iii). All spectra are normalized to the maximum absolute value at $t_2 = 0$. Six contours equally spaced between -1 and 0 and between 0 and 1 are shown, with negative contours in blue and positive in red.

spectra calculated with the same parameters as in Fig. 5.4 but with quadratic coupling $\nu_{\mathrm{LL}} = 0$ and $\nu_{\mathrm{SL}} = 0.222$, in rows (a) and (b), respectively. These results show minimal broadening for all waiting times, in qualitative agreement with the results in Fig. 3(ii) in Ref. 43. Quadratic coupling facilitates exchange of two system quanta and one bath quantum and so is unlikely to produce line broadening for this spectral density. We do not make a direct comparison to Fig. 3 of Ref. 43 because the results here are for a smaller γ and, with relatively high Ω/N_{B}, the finite bath does not well represent the continuum. However, the spectra in the motional narrowing regime shown in Fig. 3 of Ref. 43 display some of the same features as the results in Figs. 5.4 and 5.5. First, the fluctuating-frequency result for LL coupling in the continuum case shows no significant broadening in

Fig. 3(b-i) of Ref. 43, as do the results in column (a) of Fig. 5.4. Second, the quantum LL result shows no apparent inhomogeneous broadening at $t_2 = 0$, while our results show diminished inhomogeneous broadening at finite t_2 compared to the pure dephasing results in Figures 5.1 and 5.2. Finally, the OMT results in Fig. 5.5 show minimal broadening with SL coupling which is consistent with the results in row (ii) of Fig. 3 in Ref. 43. This qualitative agreement indicates that the OMT can reproduce broadening mechanisms outside the pure dephasing regime. While the interpretation of these spectra is more complex than in the pure dephasing limit, these OMT calculations are less numerically demanding, because the bath modes sample a smaller range of action values.

5.2 Two Oscillators with a Bath and Energy Transfer

In this section, we calculate purely absorptive spectra for two oscillators coupled to a bath described by quantum Hamiltonian,

$$\hat{H} = \hat{H}_a + \hat{H}_b + c_{ab}\sqrt{m_a m_b}\omega_a\omega_b\hat{q}_a\hat{q}_b + \sum_{j=1}^{N_\mathrm{B}} \frac{\hat{p}_j^2}{2m_j} + \frac{m_j\omega_j^2}{2}\left(\hat{q}_j - \frac{c_j V(\hat{q}_a,\hat{q}_b)}{m_j\omega_j^2}\right)^2 . \quad (5.11)$$

The local modes a and b are taken to be Morse oscillators. The well depths of modes a and b are specified by $\beta D_a = 391$ and $\beta D_b = 291$. We take $\omega_b = 0.96\omega_a$, the coupling between mode a and b to be $c_{ab} = 0.01$ and $\beta\hbar\omega_a = 7.75$. The bath defined in Eq. (5.2) is specified by $N_\mathrm{B} = 60$, $\Omega = 0.06\omega_a$, $\eta = 100 m_a\omega_a$ and $\gamma = 0.004\omega_a$. All masses are taken to be equal.

Results are computed using the FB implementation including energy transfer, as described in Sec. 3.4. The coupled chromophore normal modes were treated with first order perturbation theory[56] in cubic anharmonicity and the bath modes were treated to zeroth order as harmonic oscillators in carrying out the required

canonical transformations between Cartesian coordinates and momenta and action-angle variables. Initial conditions were generated from 2500 Metropolis sampled initial actions, $\mathbf{J}_0$, and random angles with $\mathbf{J}_1(t_1) = \mathbf{J}_0\big|_{J_0^{r'_0} \to J_0^{r'_0} + \hbar/2}$. One set of initial conditions was used to compute all results. To reduce the number of initial conditions required to converge the response function at long times a one-sided cosine-squared window function in t_1 and t_3 was applied to the response function prior to taking the Fourier transforms,[85] as for the high frequency bath results in Sec 5.1.2. For simplicity, the bath is neglected in solving for the chromophore actions to determine r_0, as described in Sec. 3.4, although propagated trajectories include the bath.

Figure 5.6 shows $R^{(3)}_{\text{abs}}(\omega_3, \omega_1; t_2)$ for various values of t_2. Row (i) shows the full response function computed from Eq. (2.29). Row (ii) shows the contribution to (i) generated by trace-satisfying parent diagrams defined in Eq. (2.21) and row (iii) shows the remaining contribution to (i) resulting from non-trace-satisfying parent diagrams. Spectra are shown at $\omega_a t_2 = 0$, 420, and 1250 in columns (a)-(c), respectively. The spectra show bath-induced dephasing. At $t_2 = 0$, shown in column (a), all peaks are diagonally elongated, indicating inhomogeneous broadening.[5,11,86] The peaks in each row become more rounded as the waiting time becomes long compared to dephasing times as seen in columns (b) and (c).

The spectrum at zero waiting time in Fig. 5.6(ai) shows four pairs of peaks. In the absence of energy transfer the primary contributions to the diagonal pairs are generated by OMT diagrams with all interactions occurring either with chromophore mode 1, with higher frequency, or with chromophore mode 2, with lower frequency. The off-diagonal pairs of peaks are generated from OMT diagrams with two interactions occurring with each mode. The negative (blue) fundamental peak

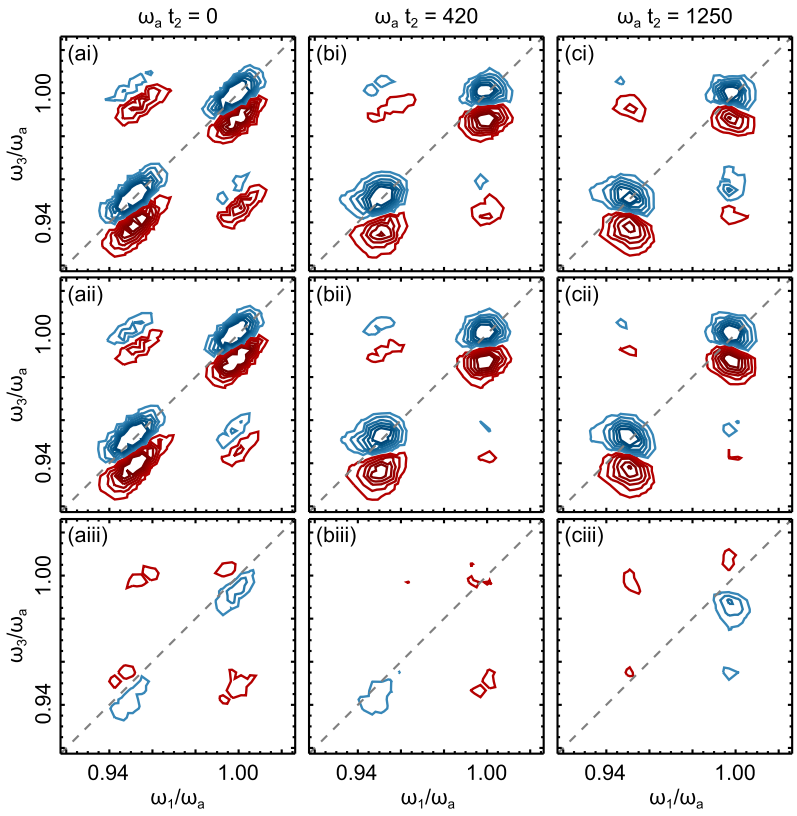

Figure 5.6: $R^{(3)}_{\text{abs}}(\omega_3, \omega_1; t_2)$ for a thermal ensemble of coupled Morse oscillators. OMT results from Eq. (2.29) are shown in row (i), contributions from trace-satisfying parent diagrams are shown in row (ii), and contributions from non-trace-satisfying parent diagrams are given in row (iii). Spectra are shown for $\omega_a t_2 = 0$, 420, and 1250 in columns (a)-(c), respectively. Six equally spaced positive and negative contours up to 50% of the maximum absolute value in panel (ai) are drawn in each plot, with positive contours in red and negative in blue.

in each pair corresponds to one mode being in a coherence during the t_3 time period and the other being in the ground state. In the absence of thermally excited chromophore states these peaks are generated by OMT diagrams with one of the middle interactions increasing and the other decreasing the action. The positive (red) anharmonic peak corresponds to one mode being in a coherence and the other in the first excited state during the t_3 time period and are generated under these conditions from diagrams with both middle interactions increasing the system action. For example, Fig. 5.7 shows diagrams contributing in the $\mathbf{k}_{\text{I}}$ phase-matched

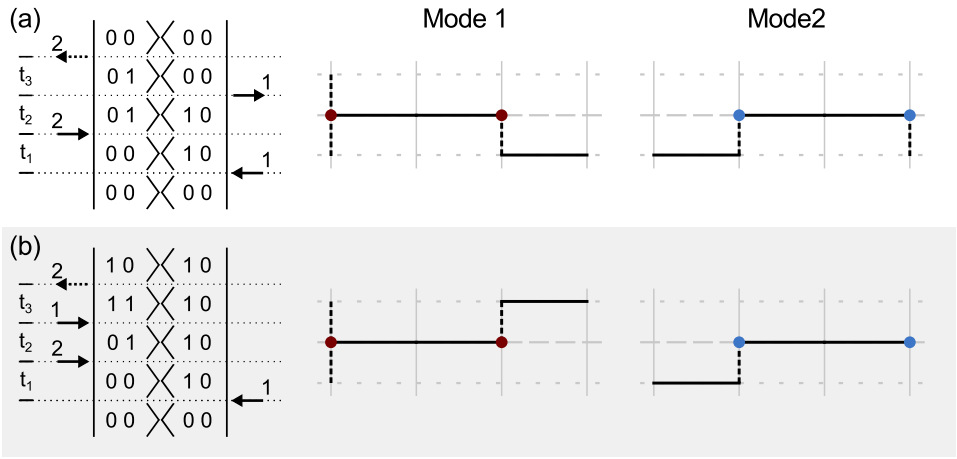

Figure 5.7: 2FDs starting in the ground state are shown with their corresponding OMT diagrams. These diagrams contribute to the lower right pair of off-diagonal peaks in the $\mathbf{k}_{\mathrm{I}}$ phase-matched direction. Panel (a) shows a contribution to the negative (blue) peak and panel (b) a contribution to the positive (red) anharmonic peak.

direction to the lower right pair of off-diagonal peaks. The OMT diagram in panel (a) contributes to the negative fundamental peak and the OMT diagram in (b) contributes to the positive anharmonic peak. The association of OMT diagrams with specific peaks in the 2D spectra aids in the interpretation of the spectra, as demonstrated in the discussion of Figs. 5.9 and 5.10.

Contributions from both trace-satisfying parent diagrams in row (ii) and non-trace-satisfying parent diagrams in row (iii) can include energy transfer events. In particular, contributions from OMT diagrams with one energy transfer event during the t_1 time period will contribute to row (ii), as t_1 coherence transfer does not alter the trace-satisfying nature of a diagram in the FB implementation, as discussed in Sec. 3.4. The dominant contribution to this row, however, is from trace-satisfying parent diagrams that do not include energy transfer events. The non-trace-satisfying parent diagrams used to compute the results in row (iii) will not contribute in the absence of anharmonic processes such as energy transfer.

Comparison of row (i) of Fig. 5.6 with rows (ii) and (iii) shows that the non-trace-satisfying diagrams have a small but non-negligible contribution to the 2D spectra. At $t_2 = 0$ all contributions from non-trace-satisfying parent diagrams in (aiii) are expected to result from child diagrams that have energy transfer during the t_3 or during both the t_1 and t_3 time periods. The effect of these diagrams on the complete spectrum in (ai) is to increase the relative contribution of the positive anharmonic off-diagonal peaks while decreasing the magnitude of the diagonal peaks, particularly the diagonal anharmonic peak. The ω_3 frequencies associated with anharmonic peaks occur during t_3 if both middle interactions increase the action. The larger relative amplitudes of the off-diagonal anharmonic peaks in column (a) of Fig. 5.6 therefore indicate that energy transfer is more likely to occur when higher energy states are accessed during t_3 than when lower energy states are propagated during t_1 or t_3.

Figure 5.8 shows purely absorptive spectra for the same parameters as in Fig. 5.6. Column (a) reproduces the results from Fig. 5.6(a) and columns (b) and (c) show results at $\omega_a t_2 = 70$ and $\omega_a t_2 = 140$, respectively. For two coupled chromophores, the primary waiting time dependence of the off-diagonal peaks is an oscillation at frequency $\omega_{10,01} \equiv (E_{10} - E_{01})/\hbar \approx \left(\left(E_1^{(1)} - E_0^{(1)}\right) - \left(E_0^{(2)} - E_1^{(2)}\right)\right)/\hbar$. This can be seen, for example, in the waiting time dependence of the 2FDs in Fig. 5.7. The spectra at $\omega_a t_2 = 70$ in column (b) of Fig. 5.8 are computed at roughly half the period of this oscillation, and in column (c) are calculated at roughly one period. The trace-satisfying contribution in row (ii) shows the expected oscillation of the off-diagonal peaks. The non-trace-satisfying contribution to the off-diagonal peaks in row (iii) also shows an oscillation on this time scale. This results in an oscillation in the off-diagonal peaks in the full spectrum in Figs. 5.8(ai)-(ci), although there is a non-negligible

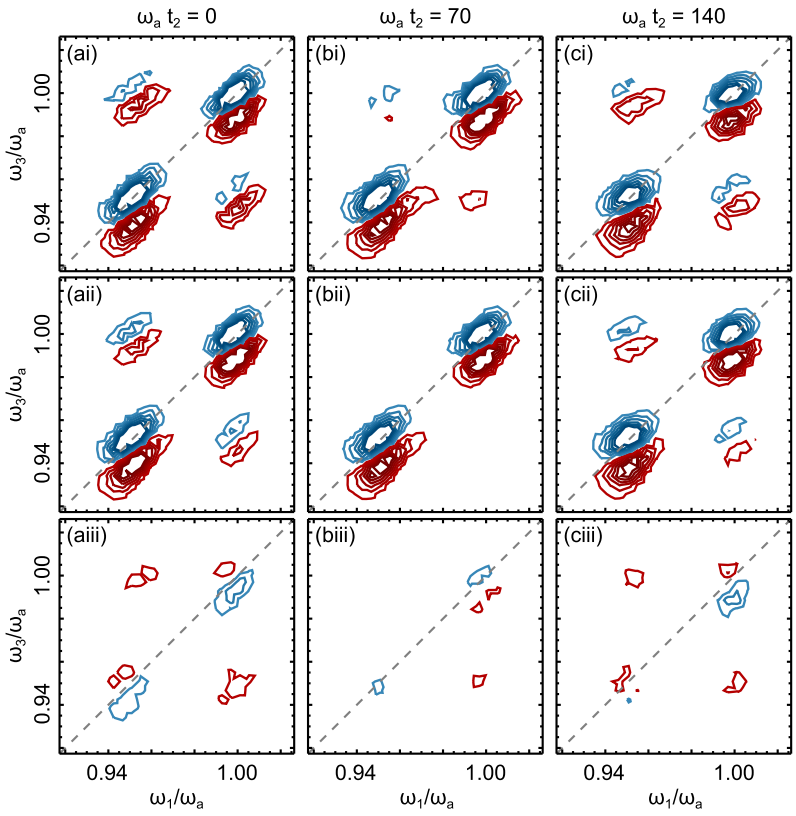

Figure 5.8: $R^{(3)}_{\text{abs}}(\omega_3, \omega_1; t_2)$ for the same parameters as Fig. 5.6 for $\omega_a t_2 = 0$, 70, and 140 in columns (a)-(c), respectively. Six equally spaced positive and negative contours up to 50% of the maximum absolute value in panel (ai) are drawn in each plot, with positive contours in red and negative in blue.

contribution to the off-diagonal peaks at $\omega_a t_2 = 70$. The diagonal peaks in row (iii) also exhibit an oscillation on this time scale. This phase oscillation is absent in row (ii) since trace-satisfying parent diagrams contributing to the diagonal peaks primarily evolve in populations during t_2.

The contributions from specific non-trace-satisfying parent diagrams are analyzed in Figs. 5.9 and 5.10. Figure 5.9(b) shows a contribution to $\left|\tilde{R}^{(3)}_{\text{I}}(\omega_3, -\omega_1; t_2)\right|$ at $t_2 = 0$ from the non-trace-satisfying parent diagram with sequence of chromophore interactions 1211 and the second and third interactions increasing the action. The pair of 2FDs and OMT diagram corresponding to this contribution

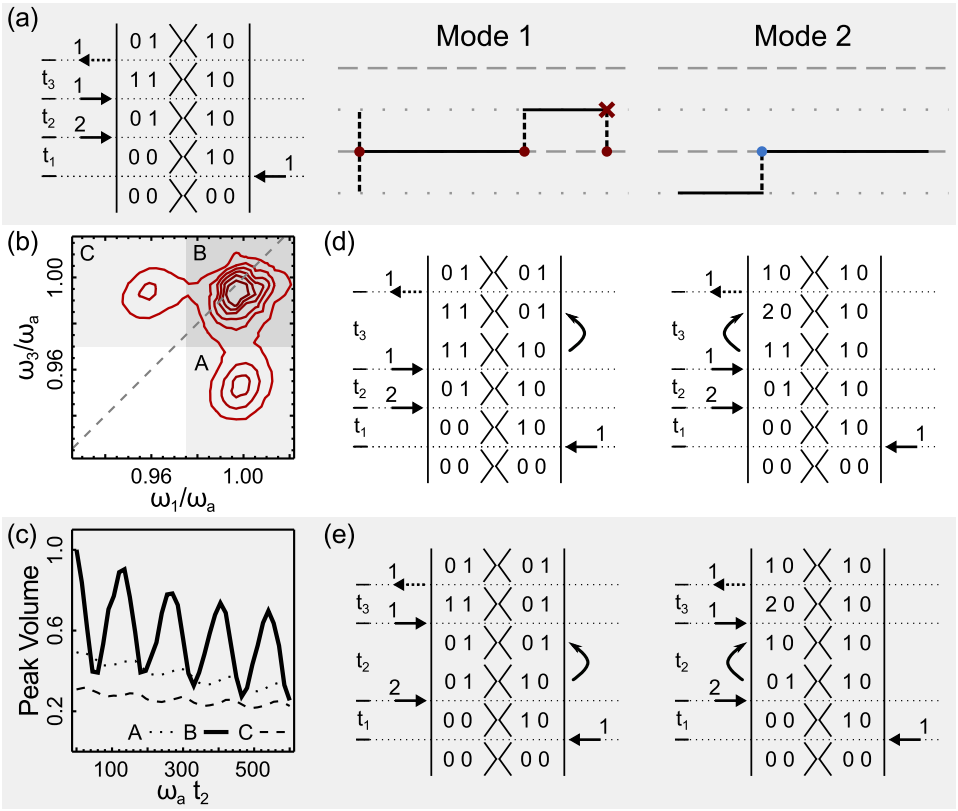

Figure 5.9: Contribution to the rephasing response, $\left|\tilde{R}_{\mathrm{I}}^{(3)}(\omega_3, -\omega_1; t_2)\right|$ from the non-trace-satisfying parent diagram in panel (a) is shown in (b) for $t_2 = 0$. Six equally spaced contours between 0 and 75% of the maximum height in peak B are shown. Relative integrated volumes of the peaks labeled A, B, and C in (b) are shown as a function of t_2 in panel (c). Volumes are normalized to the volume of peak B at $t_2 = 0$. The two trace-satisfying child 2FDs with one energy transfer event during t_3 are shown in (d) and the two trace-satisfying child diagrams with one energy transfer event during t_2 are shown in (e).

are shown in panel (a). The three visible peaks in the spectrum in Fig. 5.9(b) are labeled A, B, and C. In the absence of anharmonicity the non-trace-satisfying diagram in panel (a) would not contribute, indicating this signal is a result of anharmonic processes, such as energy transfer. The distinct peaks at $t_2 = 0$ can be attributed to energy transfer processes during the t_3 time period or during both the t_3 and t_1 time periods. Figure 5.9(d) shows the two trace-satisfying child 2FDs of the parent diagram in panel (a) with one energy transfer event during the t_3 time period. The positions of the peaks in Fig. 5.9(b) can be directly related to

the 2FDs in (d). Specifically applied frequency ω_1 for peaks A and B is associated with material frequency $\omega_{00,10}$, from the evolution of a single quantum coherence for the higher frequency normal mode 1. This is the expected t_1 frequency without energy transfer. Peak A is an off-diagonal peak with frequency ω_3 corresponding to $\omega_{11,10}$, that is, the evolution of a single quantum coherence for the lower frequency mode 2 and a population in mode 1. This is the frequency expected without energy transfer during the t_3 time period and is the first frequency accessed during t_3 in the 2FDs in Fig. 5.9(d). The ω_3 frequency of peak B is expected to include contributions from both $\omega_{11,01}$ and $\omega_{20,10}$, which are similar in magnitude. These frequencies are not reached in the parent diagram in Fig. 5.9(a) but are accessed in the child diagrams shown in (d) due to energy transfer during the t_3 time period. In contrast to peaks A and B, peak C reflects the frequency $\omega_{00,01}$ during t_1, a coherence in the lower frequency mode 2. This frequency may be reached if energy transfer occurs during back propagation of $|00\rangle\langle 10|$ during the t_1 time period. This transfer alone would not make the diagram in Fig. 5.9(a) trace-satisfying, consistent with no visible peak in the unlabeled quadrant of Fig. 5.9(b). To satisfy the trace, energy transfer must additionally occur during t_3, as reflected by the ω_3 frequency associated with peak C being $\omega_{11,01}$ or $\omega_{20,10}$.

Dynamics of the integrated volumes of the peaks labeled A, B, and C in Fig. 5.9(b) are shown in Fig. 5.9(c) relative to the volume of peak B at $t_2 = 0$. We define each peak as being located in the gray shaded regions in panel (b). Energy transfer events may occur during t_2 for nonzero propagation times. Therefore, the 2FDs in panel (e) may contribute to Fig. 5.9(c) both without and with t_1 energy transfer. In Fig. 5.9(c) all three peak volumes show an oscillation in t_2 that corresponds to the difference in the oscillator's one-quantum coherence frequencies, $\omega_{01,10}$. This is the expected frequency during this time period as indicated in the

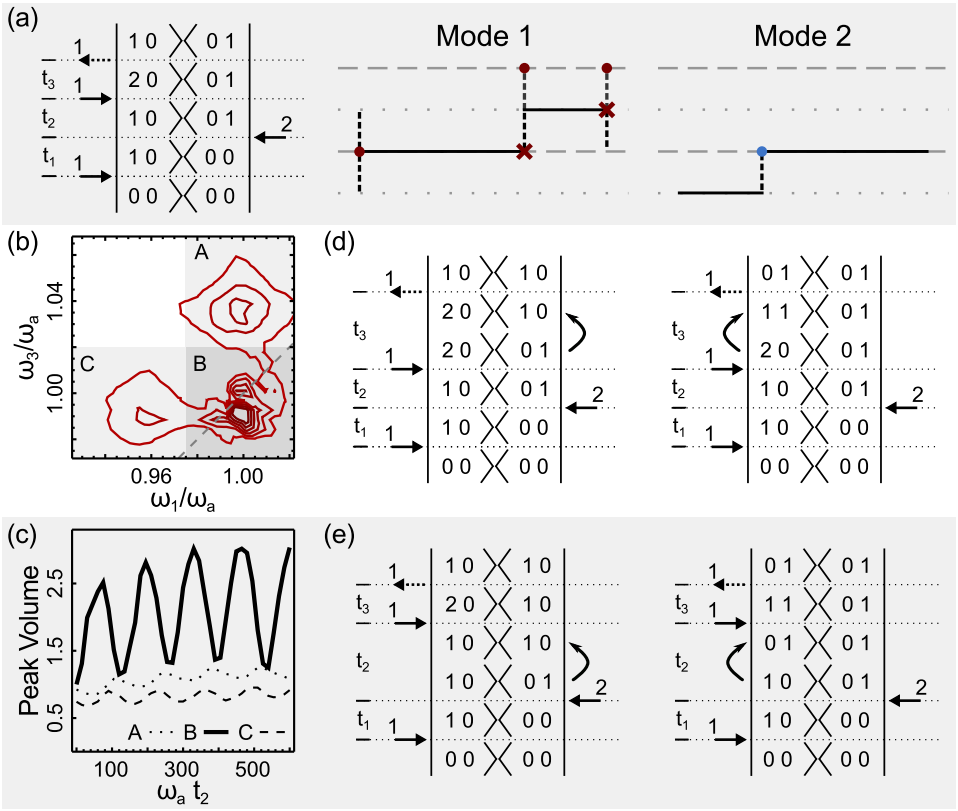

Figure 5.10: Contribution to the nonrephasing response, $\left|\tilde{R}^{(3)}_{\mathrm{II}}(\omega_3, \omega_1; t_2)\right|$ from the non-trace-satisfying parent diagram in (a) is shown in (b) for $t_2 = 0$. Six equally spaced contours between 0 and 75% of the maximum height of peak B are shown. Relative volumes of the peaks labeled A, B, and C in (b) are shown in (c) as a function of t_2, normalized to the volume of peak B at $t_2 = 0$. The two trace-satisfying child diagrams with one energy transfer event during t_3 and one energy transfer event during t_2 are shown in (d) and (e), respectively.

2FDs in (d) and (e). In addition to this oscillation there is an overall bath-induced decay in the rephasing signal.

Figure 5.10(a) shows the non-trace-satisfying 2FD and the OMT parent diagram contributing in the $\mathbf{k}_{\mathrm{II}}$ phase-matched direction with the same sequence of interactions as in Fig. 5.9. This diagram's contribution to the nonrephasing response, $\left|\tilde{R}^{(3)}_{\mathrm{II}}(\omega_3, \omega_1; t_2)\right|$ at $t_2 = 0$ is shown in Figure 5.10(b). The three peaks labeled A, B, and C can be related to the trace-satisfying child diagrams in Fig. 5.10(d). The ω_1 and ω_3 frequencies of peak A are approximately $\omega_{10,00}$ and $\omega_{20,01}$, which

correspond to the frequencies present during t_1 and t_3 in the absence of energy transfer. The relatively high ω_3 frequency of this peak was not present in the diagrams contributing to the rephasing signal in Fig. 5.9(d) and had negligible peak volume in 5.9(b), consistent with the 2FDs shown in both figures. The ω_1 frequency of peak B of Fig. 5.10, $\omega_1 = \omega_{10,00}$, corresponds to no energy transfer occurring during t_1, while its ω_3 frequency corresponds to energy transfer during t_3. It is expected that both $\omega_{20,10}$ and $\omega_{11,01}$ can be reached during t_3 via energy transfer as shown in the 2FDs in Fig. 5.10(d), so that both ω_3 frequencies may contribute to peak B. Peak C corresponds to energy transfer during both the t_1 and the t_3 time periods. Integrated peak volumes normalized to the volumes of peak B at $t_2 = 0$ are shown in panel (c). With nonzero t_2 the trace-satisfying child diagrams with one energy transfer event during t_2 shown in panel (e) may also contribute to the signal in (c). The volume of peaks A, B, and C oscillate in Fig. 5.10(c) at a single dominant frequency, $\omega_{10,01}$, as predicted by the 2FDs in (d) and (e). The oscillation in Fig. 5.10(c) is out of phase with the oscillation in Fig. 5.9(c). The peak volumes in Fig. 5.10(c) increase as a function of time, as did the rephasing response in Fig. 5.3(b) for a single oscillator coupled to a bath. This is the expected trend for the nonrephasing signal.[87] Additionally, this signal begins at a lower absolute amplitude than the rephasing signal in Fig. 5.9(c). An increase in the nonrephasing signal, as in Fig. 5.10(c), together with a decay in the rephasing signal, as in Fig. 5.9(c), results in the rounding of peaks in the 2D spectrum as a function of t_2, as shown in Fig. 5.6.

The purely absorptive 2D spectra presented in this section demonstrate that the generalization of FB implementation in Sec. 3.4 can be applied to systems in which approximate classical action variables show significant time dependence over the simulation time scale and that this generalization gives results consistent with

2FDs with coherence transfer events.

Chapter 6
Conclusion

The optimized mean-trajectory (OMT) approximation was derived for a single degree of freedom in Sec 4.1.2 within a harmonic approximation to pairs of double-sided Feynman diagrams (2FDs). In this semiclassical approximation, the evolution of the density operator is approximated by an action-quantized classical trajectory with action corresponding to the average quantum number associated with the bra and ket aspects of the density operator. Each interaction with the electric field causes a jump in action at constant angle value, with the response function evaluated as a four-point correlation function of factors evaluated along these paths. All time dependences of the quantum mechanical response function were shown to be well reproduced by the OMT for a single degree of freedom in Sec. 4.1.1. While the OMT is derived within a harmonic approximation, it is implemented using classical trajectories propagated with the full anharmonic Hamiltonian in the good, or approximations to the good, action-angle variables. This allows for the incorporation of several anharmonic effects into the OMT results. For a single degree of freedom, this includes reproducing anharmonic frequencies and qualitatively including spectral features corresponding to harmonically forbidden quantum transitions.

The OMT approximation for multiple degrees of freedom, described in Sec. 2.2, is challenging to implement exactly. This motivated the development of several approximate implementation schemes, described in Chapter 3. The accuracy of these implementations was validated in Sec. 4.1.2 for a single degree of freedom. The fixed-trajectory (FT) implementation, described in Sec. 3.2, was applied to systems of coupled oscillators in Sec. 4.2. These results demonstrated that the

OMT can reproduce coupling effects in all time dependences. The OMT reproduced quantum mechanical results especially well for a system with parameters selected to be similar to an experimental system of interest.

In Chapter 5 purely absorptive spectra were computed for system-bath models calculated with the forward-backward (FB) implementation of the OMT presented in Secs. 3.3 and 3.4. For a single chromophore mode coupled to a bath, the OMT again showed its capacity to reproduce anharmonic effects, such as broadening caused by both bilinear and square-linear coupling to a harmonic bath. The OMT also captured broadening mechanisms in a system-bath model outside of the pure dephasing regime. Finally, the OMT was generalized to include energy transfer with theoretical extension and implementation details described in Sec. 2.2.1 and Sec. 3.4, respectively. This generalization was tested for a pair of near-resonant oscillators coupled to an off-resonant bath in Sec. 5.2. In this application, signals generated from non-trace-satisfying parent diagrams were directly related to 2FDs including coherence transfer events. These results justify the extension of the OMT to models in which approximate action variables show significant time dependence.

Together these results show the promise of computing 2D IR spectra directly from classical trajectories with the OMT approximation. Moving forward, the application of the OMT to larger systems would ideally include using molecular dynamics simulations as the source of these classical trajectories. To achieve this, the three numerical challenges associated with implementing the OMT approximation, discussed in Chapter 3, would have to be considered. (1) Approximate action-angle variables would need to be determined to generate trajectory initial conditions. As demonstrated in Chapter 5, for systems with relatively low anharmonicity first or second order corrections to normal mode action and angle

variables are likely to be sufficient. (2) Action jumps at constant angle will need to be determined. Again, relatively simple approximations, such as harmonic scaling, were of sufficient accuracy for the systems studied here. (3) An average over initial conditions needs to be carried out. For most experimental systems studied it is a reasonable approximation that all chromophore modes begin in the ground state, which will greatly reduce the number of diagrams that need to be computed. Nevertheless, the angle average and action average for low frequency modes could pose a challenge as sufficient sampling is needed to reproduce dephasing processes. One of the main challenges in coupling the OMT approximation to a molecular dynamics package not faced in the applications to exact molecular models here, is that trajectories must accurately represent the vibrational anharmonicities and anharmonic couplings between vibrations in order to well reproduce 2D IR spectra. Overall, the success of relatively simple approximate OMT implementations in this thesis leave us optimistic about the future applications of this method.

Appendix A

Action Angle Perturbation Theory

The good action-angle variables are generalized momenta and coordinate variables defined so that the transformed Hamiltonian has no angle dependence.[55] The properties of these variables are briefly reviewed in Sec. 3.1. If they exist, the action-angle variables for an f-dimensional systems can be determined perturbatively from the zeroth order harmonic action-angle variables following the derivation by Schatz and Mulloney in Ref. 56. Let $\mathbf{I}$ and $\boldsymbol{\theta}$ be the harmonic action-angle variables for which the position and momentum solutions are given by,

$$x_n = \sqrt{\frac{2I_n}{\omega_n}} \cos\theta_n \tag{A.1}$$

$$p_n = -\sqrt{2I_n\omega_n} \sin\theta_n \tag{A.2}$$

The full Hamiltonian can be written in the form,

$$H = \boldsymbol{\omega} \cdot \mathbf{I} + V_{\text{anh}}(\mathbf{x}) \tag{A.3}$$

where V_{anh} is the anharmonic contribution to the Hamiltonian. In the results in Chapters 4 and 5 this contribution is taken to, at most, second order in anharmonicity, $V_{\text{anh}} = \lambda V_{\text{C}} + \lambda^2 V_{\text{Q}}$. By transforming to normal modes prior to determining action-angle variables all bilinear coupling terms are removed from the Hamiltonian so that the term V_{C} consists of all third order polynomial terms and V_{Q} consists of all fourth order polynomial terms.

Corrections to Eqs. (A.1) and (A.2) can be determined perturbatively by following the approach in Ref. 56. The central object in this approach is the type 2 generating function,[55] $F_2(\boldsymbol{\theta}, \mathbf{J})$, which defines a canonical transformation from the harmonic action-angle variables $(\boldsymbol{\theta}, \mathbf{I})$ to the good action-angle variables $(\boldsymbol{\phi}, \mathbf{J})$

with,[55]

$$I_n \equiv \left(\frac{\partial F_2}{\partial \theta_n}\right), \quad \phi_n \equiv \left(\frac{\partial F_2}{\partial J_n}\right). \tag{A.4}$$

This generating function can be written in the form,

$$F_2(\boldsymbol{\theta}, \mathbf{J}) = \boldsymbol{\theta} \cdot \mathbf{J} + G_2(\boldsymbol{\theta}, \mathbf{J}), \tag{A.5}$$

with $G_2(\boldsymbol{\theta}, \mathbf{J})$ a periodic function of $\boldsymbol{\theta}$.[56] This allows for G_2 to be expanded as a Fourier series in $\boldsymbol{\theta}$,

$$G_2(\boldsymbol{\theta}, \mathbf{J}) = -i \sum_{\mathbf{k}}{}' A_{\mathbf{k}}(\mathbf{J}) e^{i\mathbf{k}\cdot\boldsymbol{\theta}}. \tag{A.6}$$

The vector $\mathbf{k}$ is an f-dimensional vector of integers and the prime on the summation indicates that $\mathbf{k} = \mathbf{0}$ is omitted. Substituting into Eq. (A.4) with the form of the generating function in Eqs. (A.5) and (A.6) gives,

$$I_n = J_n + \sum_{\mathbf{k}}{}' k_n A_{\mathbf{k}}(\mathbf{J}) e^{i\mathbf{k}\cdot\boldsymbol{\theta}}, \tag{A.7}$$

$$\phi_n = \theta_n - i \sum_{\mathbf{k}}{}' \left(\frac{\partial A_{\mathbf{k}}(\mathbf{J})}{\partial J_n}\right) e^{i\mathbf{k}\cdot\boldsymbol{\theta}}. \tag{A.8}$$

The $\mathbf{k}^{\text{th}}$ Fourier series coefficient can then be obtained by substituting Eq. (A.7) into Eq. (A.3),

$$A_{\mathbf{k}} = -\frac{1}{\boldsymbol{\omega}\cdot\mathbf{k}} \int \frac{\mathrm{d}\boldsymbol{\theta}}{(2\pi)^f} V_{\text{anh}}\left(\mathbf{x}\left(\boldsymbol{\theta}, \mathbf{J}\right)\right) e^{-i\mathbf{k}\cdot\boldsymbol{\theta}}. \tag{A.9}$$

To obtain Eq. (A.9) we have used that $H = H(\mathbf{J})$ and have assumed that frequencies are incommensurate so that $\boldsymbol{\omega}\cdot\mathbf{k} \neq 0$ for any nonzero $\mathbf{k}$. In Ref. 56, the primary quantity of interest is the system energy, given by the zeroth Fourier component of Eq. (A.3),

$$E(\mathbf{J}) = \boldsymbol{\omega}\cdot\mathbf{J} + \int \frac{\mathrm{d}\boldsymbol{\theta}}{(2\pi)^f} V_{\text{anh}}\left(\mathbf{x}\left(\boldsymbol{\theta}, \mathbf{J}\right)\right). \tag{A.10}$$

Because the Hamiltonian has no angle dependence, $\boldsymbol{\phi}$ defined in Eq. (A.8) is not needed to obtain the energy as a function of $\mathbf{J}$. To obtain initial conditions for

trajectory propagations, we require expressions for the position and momentum which depend on both the good action and angle variables,

$$x_n(\boldsymbol{\phi}, \mathbf{J}) = \sqrt{\frac{2}{\omega_i}} \left(J_n + \sum_{\mathbf{k}}{}' k_n A_{\mathbf{k}}(\mathbf{J}) e^{i\mathbf{k}\cdot\boldsymbol{\theta}(\boldsymbol{\phi},\mathbf{J})} \right)^{1/2} \cos\left(\boldsymbol{\theta}\left(\boldsymbol{\phi}, \mathbf{J}\right)\right), \tag{A.11}$$

$$p_n(\boldsymbol{\phi}, \mathbf{J}) = -\sqrt{2\omega_i} \left(J_n + \sum_{\mathbf{k}}{}' k_n A_{\mathbf{k}}(\mathbf{J}) e^{i\mathbf{k}\cdot\boldsymbol{\theta}(\boldsymbol{\phi},\mathbf{J})} \right)^{1/2} \sin\left(\boldsymbol{\theta}\left(\boldsymbol{\phi}, \mathbf{J}\right)\right). \tag{A.12}$$

$\boldsymbol{\theta}\left(\boldsymbol{\phi}, \mathbf{J}\right)$ is obtained by inverting Eq. (A.8). To perform sampling in action-angle variables and define initial coordinates and momenta in Chapters 4 and 5, Eqs. (A.10)- (A.12) are solved perturbatively by expanding the Fourier coefficients in anharmonicity, $A_{\mathbf{k}} \approx \lambda A_{\mathbf{k}}^{(1)} + \lambda^2 A_{\mathbf{k}}^{(2)}$, since it is clear that $A_{\mathbf{k}}^{(0)} = 0$ from Eq. (A.9) and the definition of V_{anh}.

Appendix B

The Mean-Trajectory Approximation

The mean-trajectory (MT) approximation was previously developed by Gruenbaum and Loring as a semiclassical method for computing vibrational response functions.[63–66] In the MT approximation the amplitude of the coherent optical signal propagating with wavevector $\alpha\mathbf{k}_1 + \beta\mathbf{k}_2 + \gamma\mathbf{k}_3$ in Eq. (1.10) is derived by approximating the quantum time propagator, $\hat{K}_0(t)$, as the Herman-Kluk time propagator,[52,67–70,88–91] a frozen Gaussian approximation in the coherent state basis.[92] For a single degree of freedom this semiclassical time propagator is,

$$K_{\mathrm{HK}}(t) = (2\pi\hbar)^{-1} \int \mathrm{d}\mathbf{z}\, |\mathbf{z}(t)\rangle\, G(\mathbf{z},t)\, \langle \mathbf{z}| \,. \tag{B.1}$$

Here, $G(\mathbf{z},t) \equiv C(\mathbf{z},t)e^{iS(\mathbf{z},t)/\hbar}$ for coherent state $\mathbf{z}$ and,

$$C(\mathbf{z},t) \equiv \frac{1}{4}\left(M_{qq}(\mathbf{z},t) + M_{pp}(\mathbf{z},t) - i\hbar\gamma M_{qp}(\mathbf{z},t) + \frac{i}{\hbar\gamma} M_{pq}(\mathbf{z},t) \right)^{1/2} \tag{B.2}$$

$$S(\mathbf{z},t) \equiv \int_0^t d\tau \left(p(\tau)\dot{q}(\tau) - H(p(\tau), q(\tau)) \right), \tag{B.3}$$

$$|\langle \mathbf{z}_1 | \mathbf{z}_2 \rangle| = \exp\left[-\frac{1}{4}\left(\frac{m\omega}{\hbar}(q_1 - q_2)^2 + \frac{1}{m\omega\hbar}(p_1 - p_2)^2 \right) \right]. \tag{B.4}$$

As seen from Eq. (B.1) each operation of $\hat{K}_0$ in the response function in Eq. (1.10) produces one integration over classical phase space, turning the quantum mechanical trace into a 12-dimensional integral for a single degree of freedom. The MT approximation follows from changing phase space integration variables to mean and difference variables and approximately performing the integration[63,64] over difference variables. For the quantum mechanical phase-matched response function in

Eq. (1.10) this procedure gives the MT approximation,

$$R^{(3)}_{\gamma\beta\alpha}(t_3,t_2,t_1) = \frac{i\beta\omega}{2^4\hbar^4}\int \mathrm{d}\mathbf{z}_1 \int \mathrm{d}\mathbf{z}_2 \int \mathrm{d}\mathbf{z}_3 f_{\mathrm{cl}}(\mathbf{z}_1)\Gamma(\mathbf{z}_1)\delta\left(\phi_2-\phi_1(t_1)\right)\delta\left(\phi_3-\phi_2(t_2)\right)$$
$$\times Q_\alpha(\mathbf{z}_1)\left(Q_\beta(\mathbf{z}_2)\Delta_{1+}-Q_\beta(z_1(t_1))\Delta_{1-}\right)$$
$$\times \left(Q_\gamma(\mathbf{z}_3)\Delta_{2+}-Q_\gamma(\mathbf{z}_2(t_2)\Delta_{2-}\right)Q_\delta(\mathbf{z}_3(t_3)). \tag{B.5}$$

Here $\mathbf{z}_j$ is a point in classical phase space, represented either by coordinate and momentum (q_j, p_j) or by action and angle variables (J_j, ϕ_j) and $\mathbf{z}_j(t)$ is the phase space point resulting from classical propagation of $\mathbf{z}_j$ for time t. The terms, $\Gamma(\mathbf{z})$, $\Delta_{\tau\pm}$, and $Q_\pm(\mathbf{z}(t))$ are defined in Eqs. (2.7)-(2.9) and $f_{\mathrm{cl}}(\mathbf{z})$ is the classical distributions function. The MT approximation in Eq. (B.5), like the OMT approximation, is expressed in terms of action and angle variables, which presumes that such variables can be defined. This limits the applicability of the method for multidimensional systems to regimes in which the motion is exactly or approximately quasiperiodic.[56,57] The application of the MT approximation to multiple degrees of freedom is discussed in Ref. 65.

There are many commonalities between the OMT and MT approximations to the quantum vibrational response. Expanding the terms containing $\Delta_{\tau\pm}$ in Eq. (B.5) permits the expression to be written as the sum of four correlation functions, which can be represented as semiclassical diagrams, shown in Fig. B.1. As in OMT diagrams, each horizontal segment represents classical propagation and each dashed vertical line indicates a transition in action of $\pm\hbar/2$ at fixed angle. The factor $\Gamma(\mathbf{z}_1)$ in Eq. (B.5) restricts each MT diagram to begin with action quantized to an integer multiple of $\hbar$. According to Eq. (B.5) a four-point correlation function involving factors of $Q_\pm$ is evaluated at times 0, t_1, t_1+t_2 and $t_1+t_2+t_3$ to compute the response function. The points at which the correlation function is evaluated follow from the approximations made in Ref. 64 and are indicated in Fig. B.1 with

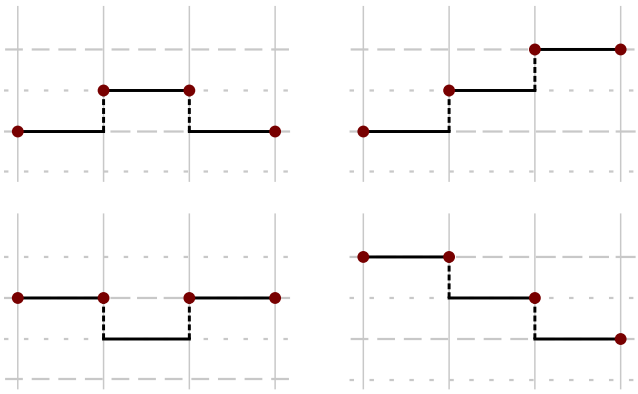

Figure B.1: The four diagrams associated with the MT approximation for the third order vibrational response function. At the start of the trajectory the action is quantized to integer multiples of $\hbar$, indicated by dashed horizontal lines. Half-odd-integer multiples of $\hbar$ are indicated by dotted horizontal lines. Interactions with the electric field are represented by jumps of $\pm\hbar/2$ in the action at constant angle. Points used in the evaluation of the correlation function are shown as red dots.

red dots.

As shown in Chapter 2 the OMT approximation can be derived independently from the MT approximation by developing a correspondence between semiclassical OMT diagrams and pairs of quantum mechanical double-sided Feynman diagrams. While these approximations are similar they different in two key respects. The first difference between the OMT and MT calculations is the identity of the classical states used in the evaluation of the correlation function as indicated by the different placements of the red dots in Fig. B.1 and Fig. 2.4. In the OMT approximation, this placement is chosen to optimally replicate the quantum mechanical system response by corresponding to the larger of the two actions transitioned between in a given interaction with the field. This results in distinct OMT diagrams representing the response function contribution from 2FDs involving coherences and populations during the waiting time, as shown in Figs. 2.4(a) and (b). In contrast, in the MT approximation the correlation function is evaluated at the larger of the two average actions being transitioned between so that in Fig. B.1 the place-

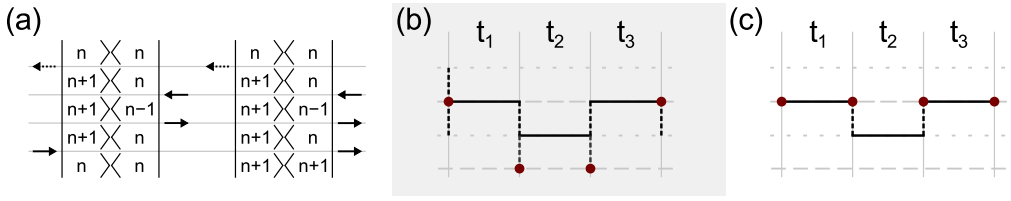

Figure B.2: A pair of 2FDs contributing to the $R_{\mathrm{III}}^{(3)}(t_3, t_2, t_1)$ system response is shown in (a). The corresponding OMT diagram is shown in (b) and MT diagram in (c).

ment of the red dot for a given transition is always on the higher action trajectory involved in that jump. This results in one set of MT diagrams that represent all phase-matched component contributions. In the harmonic limit, the different placements cause the semiclassical diagrams to have different relative contributions to the response function, as seen in the action dependences of $Q_\sigma^\pm$ in Eq. (2.10). The discrepancy between the OMT and MT results is greatest when the larger action and the larger average action transitioned between become more dissimilar, as in diagrams that represent the evolution of two-quantum coherences. For example, Fig. B.2(a) shows a pair of 2FDs contributing to $R_{\mathrm{III}}^{(3)}(t_3, t_2, t_1)$ that each evolve in a two-quantum coherence during the waiting time. The corresponding semiclassical diagrams for the OMT approximation and the MT approximation are shown in (b) and (c), respectively. In the harmonic limit of Eq. (2.10) the evaluation of the MT diagram in Fig. B.2(c) will result in an overall action dependence, $J_1 J_3$ corresponding to the quantum factor $(n+1)^2$, which differs from the factor $n(n+1)$ generated by harmonic evaluation of the 2FDs in Fig. B.2(a) and the OMT diagram in (b). These two factors approach the common limit n^2 for large quantum numbers, but their discrepancy is significant at $n = 0$. For a mode beginning in the ground state the quantum result vanishes since the 2FDs would involve deexcitation of the ground state. The MT result is nonzero, contributing a spurious frequency associated with deexcitation of the ground state. The ori-

gin of this artifact was correctly identified in the discussion of Fig. 6 of Ref. 64, but no systematic method for correcting this deficiency of the MT approximation was presented. This inconsistency between the MT approximation and quantum mechanics is remedied in the OMT approximation by altering the choice of phase space points used to evaluate the response function.

The second difference between the MT and OMT calculations is the thermal weight assigned to each diagram. In the MT approach, each diagram's statistical weight is given by the classical phase space distribution evaluated at $\mathbf{z}_1$, while in the OMT approximation each diagram's statistical weight is given by a difference of renormalized classical distributions, ΔF, defined in Eq. (2.6). This factor is evaluated at the two points prior to the first interaction with the field $\mathbf{z}_1|_{J_1 \to J_1 \pm \hbar/2}$. Neglecting the renormalization of the classical distribution in Eq. (2.6), the statistical weight of each MT diagram can be obtained as a first order expansion of the OMT statistical weight ΔF, $f_{\rm cl}\left(\mathbf{z}_1|_{J\to J_1-\hbar/2}\right) - f_{\rm cl}\left(\mathbf{z}_1|_{J\to J_1+\hbar/2}\right) \approx (\beta\hbar\omega) f_{\rm cl}(\mathbf{z}_1)$.

The effect of the differences in the OMT and MT approximations is illustrated in Fig. B.3. Column (i) shows $R^{(3)}_{\rm III}(5,t,0)$ for a thermal ensemble of non-interacting Morse oscillators described by the Hamiltonian in Eq. (4.1) with $\beta\hbar\omega = 2$ and $\beta D = 40$. The quantum mechanical and OMT results in (ai) and (bi), respectively, are reproduced from Fig. 4.1 and the MT result is shown in (ci). Qualitatively there is disagreement between the MT result and the quantum and OMT results. In column (ii) the corresponding frequency domain results are shown, with each spectrum normalized so that the $\omega_{2,0}$ peak has unit area. The quantum mechanical and OMT spectra in (aii) and (bii) are reproduced from (aiii) and (biii) of Fig. 4.5. Gray dashed vertical lines indicate the relative contributions of peaks in the quantum result in (aii). The MT spectrum in panel (cii) qualitatively repro-

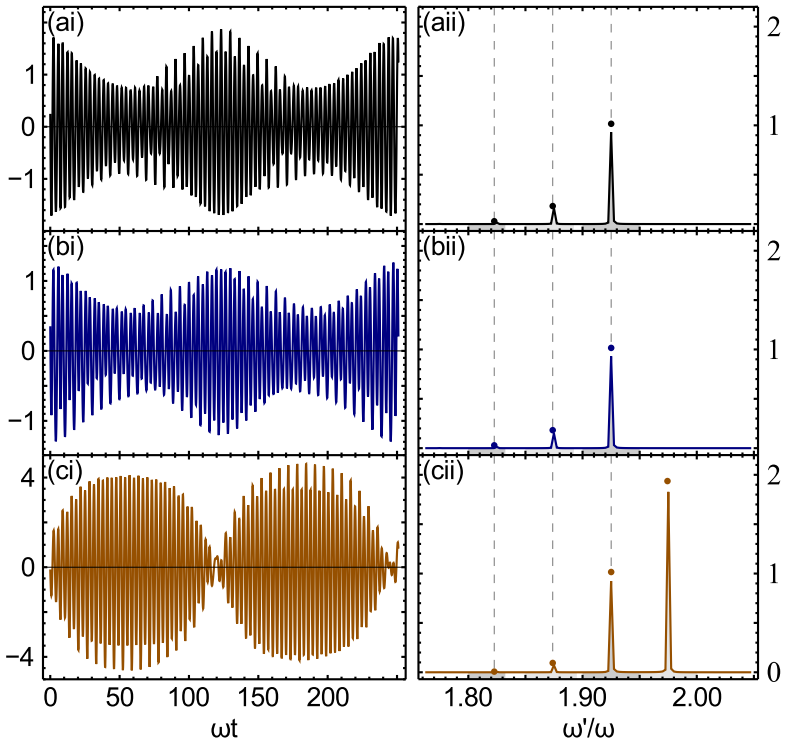

Figure B.3: The real part of $R^{(3)}_{\mathrm{III}}(5,t,0)$ for a thermal ensemble of Morse oscillators with $\beta\hbar\omega = 2$ and $\beta D = 40$ is shown in column (i) and the Fourier transform of this signal with respect to $t_3 = t$ in column (ii). Quantum mechanical results are shown in row (a), OMT results are shown in row (b) and MT approximation results in row (c).

duces the two-quantum coherence peaks from panel (aii) but contains an additional dominant peak corresponding to the spurious 2Q coherence $\omega_{1,-1}$. This frequency is largely responsible for the discrepancies between the time-domain plots in panels (aii) and (cii) in Fig. B.3. This spurious frequency is not present in the OMT approximation in panel (bii), due to the choice of evaluation points for the four-point correlation function as discussed above. The OMT also better reproduces the relative overtone contributions in the quantum mechanical results. In the MT calculation of Fig. B.3(cii), the contribution of the overtone peaks is underestimated, with peaks at frequencies $\omega_{3,1}$ and $\omega_{4,2}$ having 8% and 0.5% the relative peak areas of the $\omega_{2,0}$ peak, respectively. In the OMT calculation of Fig. B.3(cii),

these peaks have relative areas of 17% and 1.5%, closer to the relative quantum contributions of 18% and 1.7%. Therefore, in addition to removing the artifacts associated with the MT calculation, the OMT approach provides more accurate predictions for the relative contributions from different frequencies through both the choice of arguments for the correlation function and the statistical weight.

Appendix C

Wigner Transforms and the OMT

Kryvohuz and Cao[60,61] have developed a semiclassical approximation to vibrational response functions using the Weyl-Wigner-Moyal symbol-calculus[62,93] approach. The resulting semiclassical approximation is a function of the action and angle variables with action quantization conditions similar to those in the OMT approximation. In Refs. 60 and 61 this approximation was used to investigate higher order corrections to the classical limit. Here we begin with the same semiclassical approximation to the Wigner transform of the vibrational response function but apply additional harmonic approximations, similar to those used in the derivation of the OMT from pairs of 2FDs in Chapter 2. This is not the approach taken by Kryvohuz and Cao but allows for a connection between the OMT approximation and this type of approximation to be made. The resulting expression for $R^{(3)}$ has features similar to the OMT approximation but does not compute time dependences other than the vibration echo as accurately as the OMT. For simplicity, the derivations below are for a one dimensional system.

Following Kryvohuz and Cao[60] we take the semiclassical wavefunction corresponding to eigenvalue $E_n = H(J = (n + 1/2)\hbar)$ for a harmonic system to be,[94,95]

$$\langle \phi \, | n \rangle = \frac{1}{\sqrt{2\pi}} e^{in\phi}. \tag{C.1}$$

The Wigner transform for a general operator $\hat{A}$ in terms of the quantum number n and the angle variable ϕ is then given by,[93,95]

$$A_{\mathrm{W}}(n, \phi) = \int_{-\pi}^{\pi} \mathrm{d}\xi e^{in\xi} \left\langle \phi - \xi/2 \left| \hat{A} \right| \phi + \xi/2 \right\rangle \tag{C.2}$$

$$= \sum_{\Delta n=-\infty}^{\infty} A_{n+\Delta n/2, n-\Delta n/2} e^{i\Delta n\phi}, n \in \left\{ n' + \frac{|\Delta n|}{2} \right\}_{n'=0}^{\infty}, \tag{C.3}$$

with $A_{n,m} \equiv \left\langle n \left| \hat{A} \right| m \right\rangle$. From Eq. (C.2), the Wigner transform of the product of two operators $\hat{A}$ and $\hat{B}$ can be derived to be the Moyal product of the Wigner transforms of $\hat{A}$ and $\hat{B}$,

$$\begin{aligned} \left(\hat{A}\hat{B}\right)_{\mathrm{W}} &= A_{\mathrm{W}} * B_{\mathrm{W}} \\ &= A_{\mathrm{W}} \exp\left[\frac{i\hbar}{2}\left(\frac{\overleftarrow{\partial}}{\partial\phi}\frac{\overrightarrow{\partial}}{\partial J} - \frac{\overleftarrow{\partial}}{\partial J}\frac{\overrightarrow{\partial}}{\partial\phi}\right)\right] B_{\mathrm{W}} \end{aligned} \tag{C.4}$$

with $\frac{\overleftarrow{\partial}}{\partial x}$ and $\frac{\overrightarrow{\partial}}{\partial x}$ denoting that the partial derivatives act on all functions to the left and right, respectively.

We want to derive a harmonic approximation to the Wigner transformation of contributions to the third order vibrational response function in Eq. (1.10), which can be written with the time dependence on the operators as,

$$R^{(3)}_{\alpha\beta\gamma} = -\left(\frac{i}{\hbar}\right)^3 \mathrm{Tr}\left(\left[\left[\hat{q}^{\delta}(\tau_3), \hat{q}^{\gamma}(\tau_2)\right], \hat{q}^{\beta}(\tau_1)\right]\left[\hat{q}^{\alpha}(0), \hat{\rho}\right]\right). \tag{C.5}$$

In Eq. (C.5), $\tau_n = \sum_{k=1}^{n} t_k$ and $\hat{q}^{\pm}$ are defined in terms of the boson creation and annihilation operators as $\hat{q}^{+} = \sqrt{\hbar/(2m\omega)}b^{\dagger}$ and $\hat{q}^{-} = (\hat{q}^{+})^{\dagger}$. Expanding the two outer commutators of Eq. (C.5) the contributions to the response function represented by pairs of 2FDs and OMT diagrams are,

$$\frac{i}{\hbar^3}\mathrm{Tr}\left(\hat{q}^{\gamma}(\tau_2)\hat{q}^{\delta}(\tau_3)\hat{q}^{\beta}(\tau_1)\left[\hat{q}^{\alpha}(0), \hat{\rho}\right]\right), \tag{C.6a}$$

$$\frac{i}{\hbar^3}\mathrm{Tr}\left(\hat{q}^{\beta}(\tau_1)\hat{q}^{\delta}(\tau_3)\hat{q}^{\gamma}(\tau_2)\left[\hat{q}^{\alpha}(0), \hat{\rho}\right]\right), \tag{C.6b}$$

$$-\frac{i}{\hbar^3}\mathrm{Tr}\left(\hat{q}^{\delta}(\tau_3)\hat{q}^{\gamma}(\tau_2)\hat{q}^{\beta}(\tau_1)\left[\hat{q}^{\alpha}(0), \hat{\rho}\right]\right), \tag{C.6c}$$

$$-\frac{i}{\hbar^3}\mathrm{Tr}\left(\hat{q}^{\beta}(\tau_1)\hat{q}^{\gamma}(\tau_2)\hat{q}^{\delta}(\tau_3)\left[\hat{q}^{\alpha}(0), \hat{\rho}\right]\right). \tag{C.6d}$$

To aid in evaluating the Wigner transforms of the diagram contributions in Eq. (C.6) we will first derive expressions for the Wigner transform of $\hat{q}^{\pm}(t)$, $\hat{\rho}$, and the commutator of these operators.

From Eq. (C.3), the Wigner transform of $\hat{q}^{\pm}$ is

$$\left(\hat{q}^{\pm}\right)_{\mathrm{W}} = \sum_{\Delta n=-\infty}^{\infty} q^{\pm}_{n+\Delta n/2,n-\Delta n/2} e^{i\Delta n\phi}, n \in \left\{ n' + \frac{|\Delta n|}{2} \right\}_{n'=0}^{\infty}. \tag{C.7}$$

As in the derivation of the OMT approximation, we can simplify this expression using harmonic selection rules,

$$\left(\hat{q}^{\pm}\right)_{\mathrm{W}} = q^{\pm}_{n\pm 1/2,n\mp 1/2} e^{\pm i\phi}, n \in \left\{ n' + \frac{1}{2} \right\}_{n'=0}^{\infty}. \tag{C.8}$$

Using that the quantum number n and the action J are related by $J = (n+1/2)\hbar$, $\langle n \pm 1/2 \,|\hat{q}^{\pm}|\, n \mp 1/2\rangle = \sqrt{J/(2m\omega)}$ and

$$\left(\hat{q}^{\pm}\right)_{\mathrm{W}} = q^{\pm}_{\mathrm{W}}(J,\phi) = \sqrt{\frac{J}{2m\omega}} e^{\pm i\phi}, J \in \{n'\hbar\}_{n'=1}^{\infty}. \tag{C.9}$$

Furthermore, the time dependence of the coordinate can be approximated as,

$$\begin{aligned}
\left(\hat{q}^{\pm}(\tau)\right)_{\mathrm{W}} &= \left(e^{i\hat{H}\tau/\hbar} \hat{q}^{\pm} e^{-i\hat{H}\tau/\hbar} \right)_{\mathrm{W}} \\
&= \sum_{\Delta n=-\infty}^{\infty} e^{i\left(E_{n+\Delta n/2} - E_{n-\Delta n/2}\right)\tau/\hbar} q^{\pm}_{n+\Delta n/2,n-\Delta n/2} e^{i\Delta\phi} \\
&= e^{\pm i\left(E_{n+1/2} - E_{n-1/2}\right)\tau/\hbar} \sqrt{\frac{(n+1/2)\hbar}{2m\omega}} e^{\pm i\phi}
\end{aligned} \tag{C.10}$$

The last step follows from a harmonic simplification of the coordinate matrix elements. We make the additional harmonic approximations, $J = (n+1/2)\hbar$ and, following from the discussion of Eq. (2.14), $(E_{n+1/2} - E_{n-1/2})/\hbar \approx \omega(J) = \frac{\partial H}{\partial J}$,

$$\begin{aligned}
\left(\hat{q}^{\pm}(t)\right)_{\mathrm{W}}(J,\phi) &= \sqrt{\frac{J}{2m\omega}} e^{\pm i(\omega(J)t+\phi)}, J \in \{n'\hbar\}_{n'=1}^{\infty} \\
&= \hat{q}^{\pm}_{\mathrm{W}}(J,\phi;t)
\end{aligned} \tag{C.11}$$

With $\hat{q}^{\pm}_{\mathrm{W}}(J,\phi;t)$ denoting classical evolution of the state $\hat{q}^{\pm}_{\mathrm{W}}(J,\phi)$ for time t. We note that for a harmonic oscillator we have recovered the classical result in Eq. (2.10) with quantization of the action variable since $Q_{\pm} = 2q^{\pm}$.

We can similarly use Eq. (C.3) to determine the Wigner transform of the density operator,

$$\rho_{\rm W}(n,\phi) = \sum_{\Delta n=-\infty}^{\infty} \rho_{n+\Delta n/2,n-\Delta n/2} e^{i\Delta n\phi} = \rho_{n,n}, n \in \{n'\}_{n'=0}^{\infty} \tag{C.12}$$

Within the harmonic limit Eq. (C.12) for the density operator is

$$\rho_{\rm W}(J,\phi) = \frac{e^{-\beta\omega J}}{Z_{\rm Q}} = f_{\rm cl}(J)\frac{Z_{\rm cl}}{Z_{\rm Q}}, J \in \{(n'+1/2)\hbar\}_{n'=0}^{\infty}, \tag{C.13}$$

with $f_{\rm cl}$ the classical distribution function, and $Z_{\rm Q}$ and $Z_{\rm cl}$ the quantum and classical partition functions, respectively.

Finally, using Eq. (C.4) the Wigner transformation of the product of $q^{\pm}(0)$ and the density operator is

$$\left(\hat{q}^{\pm}(0)\hat{\rho}\right)_{\rm W} = q^{\pm}_{\rm W}(J,\phi;0)\rho_{\rm W}(J\mp\hbar/2), J \in \{n'\hbar\}_{n'=1}^{\infty}, \tag{C.14}$$

where in the derivation of Eq. (C.14) we used that $\exp\left[\epsilon\frac{\partial}{\partial J}\right] f(J) = f(J+\epsilon)$. Similarly, $\left(\hat{\rho}\hat{q}^{\pm}(0)\right)_{\rm W} = q^{\pm}_{\rm W}(J,\phi;0)\rho_{\rm W}(J\pm\hbar/2)$ so that,

$$\left[\hat{q}^{\pm}(0),\hat{\rho}\right]_{\rm W} = \pm q^{\pm}_{\rm W}(J,\phi;0)\left(\rho_{\rm W}(J-\hbar/2) - \rho_{\rm W}(J+\hbar/2)\right), J \in \{n'\hbar\}_{n'=1}^{\infty}. \tag{C.15}$$

Using Eqs. (C.4), (C.13), and (C.15) the response function contributions in Eq. (C.6) can be derived within this harmonic approximation to the Wigner transformation. For example, the contribution to the $\mathbf{k}_{\rm I}$ phase-matched signal from Eq. (C.6a) is,

$$\frac{i}{\hbar}{\rm Tr}\left(\left(\left(q^{+}_{\rm W}(J,\phi;\tau_2) * q^{-}_{\rm W}(J,\phi;\tau_3)\right) * q^{+}_{\rm W}(J,\phi;\tau_1)\right) * \left[\hat{q}^{-}(0),\hat{\rho}\right]_{\rm W}\right), \tag{C.16}$$

so that evaluating the Moyal products gives,

$$-\frac{i}{\hbar^3}\frac{1}{2\pi}\int {\rm d}\phi \int {\rm d}J \left(\rho_{\rm W}(J-\hbar/2) - \rho_{\rm W}(J+\hbar/2)\right)\left(\hbar\sum_{n=1}^{\infty}\delta\left(J-n\hbar\right)\right)$$
$$\times\, q^{-}_{\rm W}(J,\phi;0)q^{+}_{\rm W}(J,\phi;\tau_1)q^{+}_{\rm W}(J,\phi;\tau_2)q^{-}_{\rm W}(J,\phi;\tau_3). \tag{C.17}$$

We have shifted the action sum in Eq. (C.17) for comparison to the OMT contribution to this signal in Eq. (2.4) which can be written in the form,

$$\frac{-i}{\hbar^5}\int \mathrm{d}\mathbf{z}_1 \int \mathrm{d}\mathbf{z}_2 \int \mathrm{d}\mathbf{z}_3 \Delta F(\mathbf{z}_1)\Gamma(\mathbf{z}_1)\Delta_{1+}\Delta_{2-}\delta\left(\phi_2-\phi_1(t_1)\right)\delta\left(\phi_3-\phi_2(t_2)\right) \\ \times\left(\frac{1}{2}Q_-(\mathbf{z}_1)\right)\left(\frac{1}{2}Q_+(\mathbf{z}_1(t_1))\right)\left(\frac{1}{2}Q_+(\mathbf{z}_3)\right)\left(\frac{1}{2}Q_-(\mathbf{z}_3(t_3))\right). \quad \text{(C.18)}$$

Equation (C.18) is written to emphasize that $2q_{\mathrm{W}}^{\pm}=Q_{\pm}$ in the harmonic limit. In this limit, the harmonic Wigner approximation in Eq. (C.17) and the OMT approximation in Eq. (C.18) each reproduce the quantum mechanical result in Eq. (2.3). For the harmonic Wigner approximation this happens though cancellation of the time dependences of the q_{W} factors in Eq. (C.17) since all trajectories evolve at the same frequency, $\omega(J)=\omega$ in this limit. For an anharmonic oscillator, interpreting $q_{\mathrm{W}}^{\pm}$ as $\frac{1}{2}Q_{\pm}$ will not result in the same evaluation for Eqs. (C.17) and (C.18).

Unlike the OMT approximation, the harmonic Wigner approximation in Eq. (C.17) does not contain any action jumps. Instead the response function contribution in Eq. (C.17) involves a single classical trajectory propagated at action J evaluated at times 0, $\tau_1=t_1$, $\tau_2=t_1+t_2$, and $\tau_3=t_1+t_2+t_3$. Harmonic Wigner approximations can be obtained for all phase-matched directions and response function contributions in Eq. (C.6). In each case, continuous classical trajectories are propagated with the same initial angle, and action values corresponding to the arguments of the Q_σ factors in the corresponding OMT diagrams. For example, in Eq. (C.17) all functions q_{W} are evaluated at the same action J, corresponding to the dot placements in panel (ai) of Fig. 2.3. While the contribution to the $\mathbf{k}_{\mathrm{III}}$ phase-matched direction from Eq. (C.6a) gives,

$$-\frac{i}{\hbar^3}\frac{1}{2\pi}\int \mathrm{d}\phi \int \mathrm{d}J\left(\rho_{\mathrm{W}}(J-\hbar/2)-\rho_{\mathrm{W}}(J+\hbar/2)\right)\left(\hbar\sum_{n=1}^{\infty}\delta\left(J-n\hbar\right)\right) \\ \times q_{\mathrm{W}}^{-}(J,\phi;0)q_{\mathrm{W}}^{+}(J+\hbar,\phi;\tau_1)q_{\mathrm{W}}^{+}(J,\phi;\tau_2)q_{\mathrm{W}}^{-}(J+\hbar,\phi;\tau_3), \quad \text{(C.19)}$$

In Eq. (C.19), two distinct classical trajectories are propagated at actions corresponding to J_1 and $J_3 = J_1 + \hbar$ in the OMT diagram, and the time evaluations of these arguments corresponds to the dot placements in panel (bii) of Fig. 2.3. Therefore, we have demonstrated that by starting with the semiclassical Wigner function of contributions to the response function and applying harmonic approximations, similar to those used to derive OMT diagrams, we have attained an alternative method of computing the vibrational response function which involves the evolution of classical trajectories at the same actions that are used to evaluate the correlation function in the OMT approximation. This result further supports the use of the Q_σ arguments in the OMT approximation over those in the MT approximation, described in Appendix B. Additionally, taking ρ_{W} to be defined by its harmonic form in Eq. (C.13), the statistical weight of each contribution in this newly derived approximation, $\rho_{\mathrm{W}}(J-\hbar/2)-\rho_{\mathrm{W}}(J+\hbar/2)$, is the same renormalized difference of classical distribution functions used in the OMT, up to a factor of $\hbar$.

Figure C.1 shows the quantum mechanical and OMT results for a thermal ensemble of Morse oscillators reproduced from Fig. 4.1 in rows (a) and (b), respectively. Results calculated within the harmonic Wigner approximation, such as in Eqs. (C.17) and (C.19), interpreting $q_{\mathrm{W}}^{\pm}$ as $\frac{1}{2}Q_{\pm}$ are shown in row (c). In columns (i) and (ii) results are shown for the signal corresponding to wavevectors $\mathbf{k}_{\mathrm{I}}$ and $\mathbf{k}_{\mathrm{II}}$, respectively, for $t_1 = t_3 = t$ and $t_2 = 0$. In this case the harmonic Wigner approximation well reproduces the quantum mechanical results. The success of this approximation is specific to the echo condition since this set of conditions allow for the cancellation of frequency contributions in the t_1 and t_3 time periods.

Column (i) of Fig. C.2 shows $R_{\mathrm{III}}^{(3)}(5,t,0)$ calculated using quantum mechanics, the OMT approximation, and the harmonic Wigner approximation in rows (a)-(c),

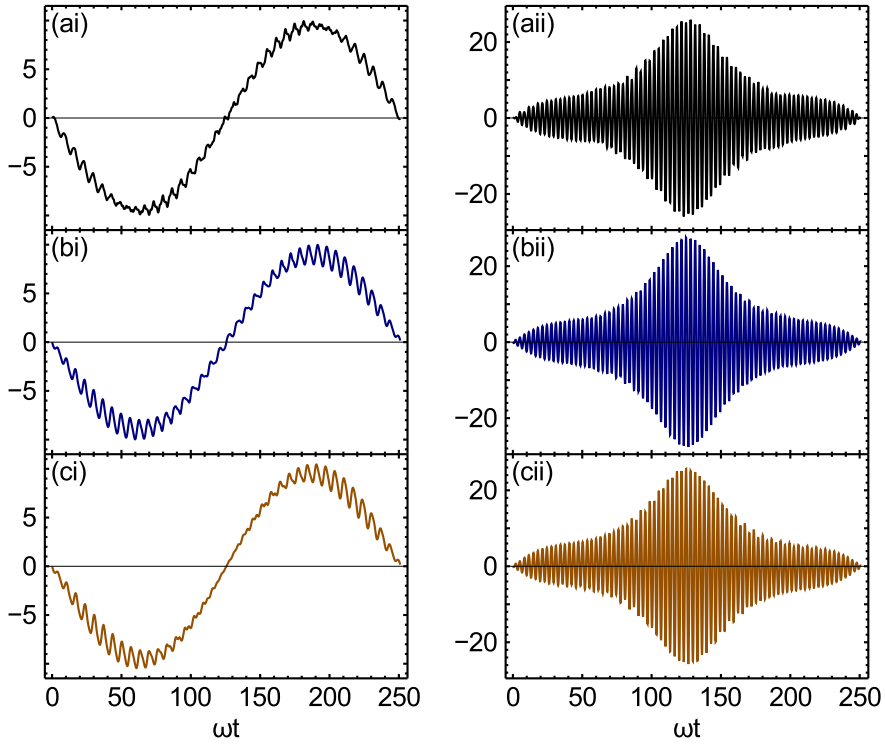

Figure C.1: Re $\left[R_{\mathrm{I}}^{(3)}(t,0,t)\right]$ for a thermal ensemble of Morse oscillators with $\beta\hbar\omega = 2$ and $\beta D = 40$ is shown in column (i) and Re $\left[R_{\mathrm{III}}^{(3)}(t,0,t)\right]$ in column (ii). Quantum mechanical results are shown in row (a), OMT results are shown in row (b) and harmonic Wigner approximation results in row (c).

respectively. The harmonic Wigner result in panel (ci) does not well reproduce the quantum result in (ai) for this set of parameters. In column (ii) the corresponding frequency domain results, $\tilde{R}_{\mathrm{III}}^{(3)}(5,\omega',0)$, are shown. The discrepancy between the harmonic Wigner approximation and the quantum mechanical result is visible in panel (cii) as a series of peaks occurring at approximately $1.75\omega_a, 1.85\omega_a, 1.90\omega_a$ and $1.95\omega_a$. These peaks are incorrectly present in the harmonic Wigner approximation because of incomplete cancellation during the t_2 time period. For example, the dominant spurious frequency at approximately $1.95\omega_a$ is generated in part by the propagation of the $q_{\mathrm{W}}^{-}(J+\hbar,\phi;\tau_3)$ term in Eq. (C.19) for $J=\hbar$.

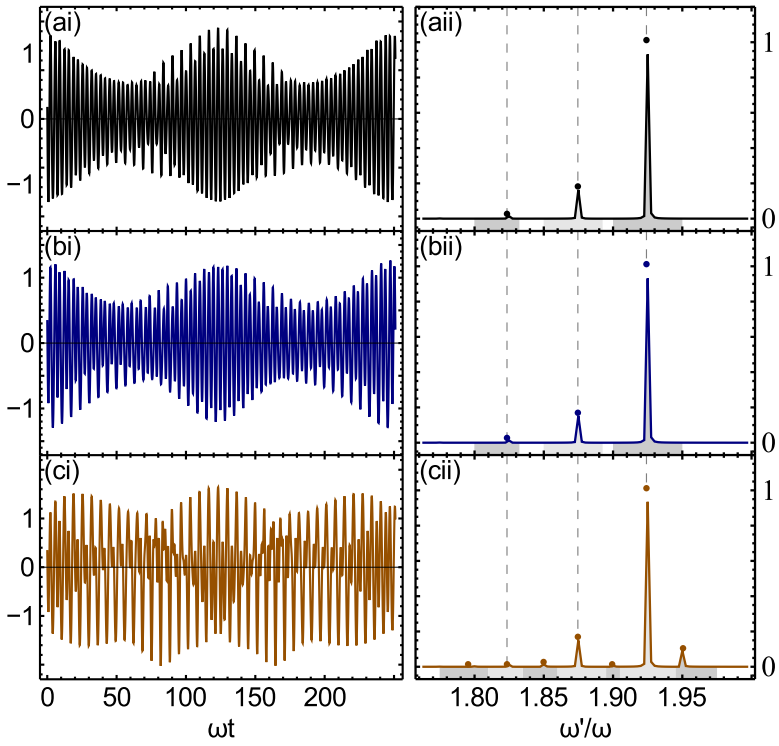

Figure C.2: The real part of $R^{(3)}_{\mathrm{III}}(5,t,0)$ for a thermal ensemble of Morse oscillators with $\beta\hbar\omega = 2$ and $\beta D = 40$ is shown in column (i) and the Fourier transform of this signal with respect to $t_2 = t$ is shown in column (ii). Quantum mechanical results are shown in row (a), OMT results are shown in row (b) and harmonic Wigner approximation results in row (c).

These results therefore show that the OMT approximation better reproduces the quantum mechanical response function than the harmonic Wigner approximation derived here. It achieves this higher accuracy by connecting the classical trajectories through action jumps so that the time course of the spectroscopic experiment is treated as an OMT path. In the harmonic Wigner approximation, each interaction with the field is essentially treated through a distinct classical trajectory, corresponding to the factors of q_{W} in Eqs. (C.17) and (C.19). The frequency dependence in the spectra for the t_1 and t_2 time intervals therefore relies on the cancellation of the frequency dependences in multiple factors of q_{W}, since trajectories are propagated for times $\tau_1 = t_1$, $\tau_2 = t_1 + t_2$ and $\tau_3 = t_1 + t_2 + t_3$. In the

harmonic limit the OMT and harmonic Wigner approximation result in identical contributions because all trajectories are propagated at the harmonic frequency, ω. However, for an anharmonic oscillator the harmonic Wigner approximation will not generally give the correct frequency dependences, as shown in Fig. C.2.

Bibliography

[1] M. Gerace and R. F. Loring. An Optimized Semiclassical Approximation for Vibrational Response Functions. *J. Chem. Phys.*, 138:124104, 2013.

[2] M. Gerace and R. F. Loring. Two-Dimensional Spectroscopy of Coupled Vibrations with the Optimized Mean-Trajectory Approximation. *J. Phys. Chem. B*, 117:15452–15461, 2013.

[3] M. Alemi and R. F. Loring. Two-Dimensional Vibrational Spectroscopy of a Dissipative System with the Optimized Mean-Trajectory Approximation. *J. Phys. Chem. B*, Published online 2014.

[4] M. Alemi and R. F. Loring. Vibrational Coherence and Energy Transfer in Two-Dimensional Spectra with the Optimized Mean-Trajectory Approximation. *J. Chem. Phys.*, 142:212417, 2015.

[5] P. Hamm and M. Zanni. *Concepts and Methods of 2D Infrared Spectroscopy.* Cambridge University Press, New York, 2011.

[6] M. Cho. *Two-Dimensional Optical Spectroscopy.* CRC Press, Boca Raton, 2009.

[7] S. Mukamel, Y. Tanimura, and P. Hamm. Coherent Multidimensional Optical Spectroscopy. *Accts. Chem. Res.*, 42:1207–1209, 2009.

[8] Y. S. Kim and R. M. Hochstrasser. Applications of 2D IR Spectroscopy to Peptides, Proteins, and Hydrogen-Bond Dynamics. *J. Phys. Chem. B*, 113:8231–8251, 2009.

[9] J. R. Zheng and M. D. Fayer. Hydrogen Bond Lifetimes and Energetics for Solute-Solvent Complexes Studied with 2D-IR Vibrational Echo Spectroscopy. *J. Am. Chem. Soc.*, 129:4328–4335, 2007.

[10] C. R. Baiz, M. Reppert, and A. Tokmakoff. *An Introduction to Protein 2D IR Spectroscopy*, pages 361–404. Taylor & Francis, New York, 2013.

[11] S. Mukamel. *Principles of Nonlinear Optical Spectroscopy.* Oxford University Press, New York, 1995.

[12] K. Wüthrich, editor. *NMR of Proteins and Nucleic Acids.* Wiley-Interscience, New York, 1986.

[13] R. S. Macomber. *A Complete Introduction to Modern NMR Spectroscopy.* Wiley-Interscience, New York, 1997.

[14] P. Hamm, M. Lim, and R. M. Hochstrasser. Structure of the Amide I Band of Peptides Measured by Femtosecond Nonlinear Infrared Spectroscopy. *J. Phys. Chem. B*, 102:6123–6138, 1998.

[15] O. Kel, A. Tamimi, M. C. Thielges, and M. D. Fayer. Ultrafast Structural Dynamics Inside Planar Phospholipid Multibilayer Model Cell Membranes Measured with 2D IR Spectroscopy. *J. Am. Chem. Soc.*, 135:11063–11074, 2013.

[16] C. Fang, A. Senes, L. Cristian, W. F. DeGrado, and R. M. Hochstrasser. Amide Vibrations Are Delocalized Across the Hydrophobic Interface of a Transmembrane Helix Dimer. *Proc. Natl. Acad. Sci. U.S.A.*, 103:16740–16745, 2006.

[17] P. Mukherjee, I. Kass, I. T. Arkin, and M. T. Zanni. Picosecond Dynamics of a Membrane Protein Revealed by 2D IR. *Proc. Natl. Acad. Sci.*, 103:3528–3533, 2006.

[18] S. Roy, T. L. C. Jansen, and J. Knoester. Structural Classification of the Amide I Sites of a β-Hairpin with Isotope Label 2DIR Spectroscopy. *Phys. Chem. Chem. Phys.*, 12:9347–9357, 2010.

[19] J. K. Chung, M. C. Thielges, and M. D. Fayer. Conformational Dynamics and Stability of HP35 Studied with 2D IR Vibrational Echoes. *J. Am. Chem. Soc.*, 134:12118–12124, 2012.

[20] M. D. Fayer, D. E. Moilanen, D. Wong, D. E. Rosenfeld, E. E. Fenn, and S. Park. Water Dynamics in Salt Solutions Studied with Ultrafast Two-Dimensional Infrared (2D IR) Vibrational Echo Spectroscopy. *Acc. Chem. Res.*, 42:1210–1219, 2009.

[21] R. A. Nicodemus, K. Ramasesha, S. T. Roberts, and A. Tokmakoff. Hydrogen Bond Rearrangements in Water Probed with Temperature-Dependent 2D IR. *J. Phys. Chem. Lett.*, 1:1068–1072, 2010.

[22] H. J. Bakker and J. L. Skinner. Vibrational Spectroscopy as a Probe of Structure and Dynamics in Liquid Water. *Chem. Rev.*, 110:1498–1517, 2010.

[23] M. Khalil, N. Demirdoven, and A. Tokmakoff. Coherent 2D IR Spectroscopy:

Molecular Structure and Dynamics in Solution. *J. Chem. Phys.*, 121:362–372, 2004.

[24] A. Amadei, I. Daidone, A. Di Nola, and M. Ashci. Theoretical-Computational Modelling of Infrared Spectra in Peptides and Proteins: A New Frontier for Combined Theoretical-Experimental Investigations. *Curr. Opin. Struct. Bio.*, 20:155–161, 2010.

[25] N. H. Ge, M. T. Zanni, and R. M. Hochstrasser. Effects of Vibrational Frequency Correlations on Two-Dimensional Infrared Spectra. *J. Phys. Chem. A*, 106:962–972, 2002.

[26] Y. J. Yan and S. Mukamel. Femtosecond Pump-Probe Spectroscopy of Polyatomic Molecules in Condensed Phases. *Phys. Rev. A*, 41:6485–6504, 1990.

[27] T. Hasegawa and Y. Tanimura. Nonequilibrium Molecular Dynamics Simulations with a Backward-Forward Trajectories Sampling for Multidimensional Infrared Spectroscopy of Molecular Vibrational Modes. *J. Chem. Phys.*, 128:064511, 2008.

[28] M. F. Gelin, D. Egorova, and W. Domcke. Efficient Calculation of Time- and Frequency-Resolved Four-Wave-Mixing Signals. *Acc. Chem. Res.*, 42:1290–1298, 2009.

[29] C. R. Baiz, K. J. Kubarych, and E. Geva. Molecular Theory and Simulation of Coherence Transfer in Metal Carbonyls and Its Signature on Multidimensional Infrared Spectra. *J. Phys. Chem. B*, 115:5322–5339, 2011.

[30] A. G. Dijkstra, T. L. C. Jansen, R. Bloem, and J. Knoester. Vibrational Relaxation in Simulated Two-Dimensional Infrared Spectra of Two Amide Modes in Solution. *J. Chem. Phys.*, 127:194505, 2007.

[31] A. Piryatinski, V. Chernyak, and S. Mukamel. Vibrational-Exciton Relaxation Probed by Three-Pulse Echoes in Polypeptides. *Chem. Phys.*, 266:285–294, 2001.

[32] J. Jeon, S. Yang, J.-H. Choi, and M. Cho. Computational Vibrational Spectroscopy of Peptides and Proteins in One and Two Dimensions. *Acc. Chem. Res.*, 42:1280–1289, 2009.

[33] K. A. Merchant, W. G. Noid, R. Akiyama, I. J. Finkelstein, A. Goun, B. L. McClain, R. F. Loring, and M. D. Fayer. Myoglobin-CO Substate Structures

and Dynamics: Multidimensional Vibrational Echoes and Molecular Dynamics Simulations. *J. Am. Chem. Soc.*, 125:13804–13818, 2003.

[34] W. Zhuang, D. Abramavicius, D. V. Voronine, and S. Mukamel. Simulation of Two-Dimensional Infrared Spectroscopy of Amyloid Fibrils. *Proc. Nat. Acad. Sci.*, 104:14233–14236, 2007.

[35] M. Cho. Correlation between Electronic and Molecular Structure Distortions and Vibrational Properties. I. Adiabatic Approximations. *J. Chem. Phys.*, 118:3480–3490, 2003.

[36] S. Ham, J.-H. Kim, H. Lee, and M. Cho. Correlation between Electronic and Molecular Structure Distortions and Vibrational Properties. II. Amide I Modes of NMA-$n$$D_2O$ Complexes. *J. Chem. Phys.*, 118:3491–3498, 2003.

[37] T. Hayashi, T. L. C. Jansen, W. Zhuang, and S. Mukamel. Collective Solvent Coordinates for the Infrared Spectrum of HOD in D_2O Based on an Ab Initio Electrostatic Map. *J. Phys. Chem. A*, 109:64–82, 2005.

[38] L. Wang, C. T. Middleton, M. T. Zanni, and J. L. Skinner. Development and Validation of Transferable Amide I Vibrational Frequency Maps for Peptides. *J. Phys. Chem. B*, 115:3713–3724, 2011.

[39] W. Zhuang, D. Abramavicius, T. Hayashi, and S. Mukamel. Simulation Protocols for Coherent Femtosecond Vibrational Spectra of Peptides. *J. Phys. Chem. B*, 110:3362–3374, 2006.

[40] R. Bloem, A. G. Dijkstra, T. L. C. Jansen, and J. Knoester. Simulation of Vibrational Energy Transfer in Two-Dimensional Infrared Spectroscopy of Amide I and Amide II Modes in Solution. *J. Chem. Phys.*, 129:055101, 2008.

[41] Z. Lai, N. K. Preketes, S. Mukamel, and J. Wang. Monitoring the Folding of Trp-Cage Peptide by Two-Dimensional Infrared (2DIR) Spectroscopy. *J. Phys. Chem. B*, 117:4661–4669, 2013.

[42] T. L. C. Jansen and J. Knoester. Waiting Time Dynamics in Two-Dimensional Infrared Spectroscopy. *Acc. Chem. Res.*, 42:1405–1411, 2009.

[43] A. Ishizaki and Y. Tanimura. Modeling Vibrational Dephasing and Energy Relaxation of Intramolecular Anharmonic Modes for Multidimensional Infrared Spectroscopies. *J. Chem. Phys.*, 125:084501, 2006.

[44] A. Ishizaki and Y. Tanimura. Dynamics of a Multimode System Coupled to Multiple Heat Baths Probed by Two Dimensional Infrared Spectroscopy. *J. Phys. Chem. A*, 111:9269–9276, 2007.

[45] A. Sakurai and Y. Tanimura. Does $\hbar$ Play a Role in Multidimensioanl Spectroscopy? Reduced Hierarchy Equations of Motion Approach to Molecular Vibrations. *J. Phys. Chem. A.*, 115:4009–4022, 2011.

[46] Y. H. Wu and V. S. Batista. Quantum Tunneling Dynamics in Multidimensional Systems: A Matching-Pursuit Description. *J. Chem. Phys.*, 121:1676–1680, 2004.

[47] M. Thoss and W. H. Miller. Generalized Forward-Backward Initial Value Representation for the Calculation of Correlation Functions in Complex Systems. *J. Chem. Phys.*, 114:9220–9235, 2001.

[48] N. Makri. Forward-Backward Semiclassical and Quantum Trajectory Methods for Time Correlation Functions. *Phys. Chem. Chem. Phys.*, 13:14442–14452, 2011.

[49] E. J. Heller. Frozen Gaussians: A Very Simple Semiclassical Approximation. *J. Chem. Phys.*, 75:2923–2931, 1981.

[50] E. J. Heller. Cellular Dynamics: A New Semiclassical Approach to Time-Dependent Semiclassical Dynamics. *J. Chem. Phys.*, 94:2723–2729, 1991.

[51] X. Sun and W. H. Miller. Forward-Backward Initial Value Representation for Semiclassical Time Correlation Functions. *J. Chem. Phys.*, 110:6635–6644, 1999.

[52] M. F. Herman. Dynamics by Semiclassical Methods. *Annu. Rev. Phys. Chem.*, 45:83–111, 1994.

[53] K. G. Kay. Semiclassical Initial Value Treatments of Atoms and Molecules. *Annu. Rev. Phys. Chem.*, 56:255–280, 2005.

[54] S. Mukamel. Nonimpact Unified Theory of Four-Wave Mixing and Two-Photon Processes. *Phys. Rev. A*, 28:3480–3492, 1983.

[55] H. Goldstein. *Classical Mechanics*. Addison-Wesley, Reading, Mass., 1950.

[56] G. C. Schatz and T. Mulloney. Classical Perturbation Theory of Good Action Angle Variables. Application to Semiclassical Eigenvalues and to Collisional Energy Transfer in Polyatomic Molecules. *J. Phys. Chem.*, 83:989–999, 1979.

[57] C. C. Martens and G. S. Ezra. Classical, Quantum Mechanical, and Semiclassical Representations of Resonant Dynamics: A Unified Treatment. *J. Chem. Phys.*, 87:284–302, 1987.

[58] J. Wu and J. Cao. Linear and Nonlinear Response Functions of the Morse Oscillator: Classical Divergence and the Uncertainty Principle. *J. Chem. Phys.*, 115:5381–5391, 2001.

[59] M. Kryvohuz and J. Cao. Non-Divergent Classical Response Functions from Uncertainty Principle: Quasi Periodic Systems. *J. Chem. Phys.*, 122:024109, 2005.

[60] M. Kryvohuz and J. Cao. Quantum-Classical Correspondence in Response Theory. *Phys. Rev. Lett.*, 95:180405, 2005.

[61] M. Kryvohuz and J. Cao. Quantum Recurrence from a Semiclassical Summation. *Chem. Phys.*, 322:41–45, 2006.

[62] M. Hillery, R. F. O'Connell, M. O. Scully, and E. P. Wigner. Distribution Functions in Physics - Fundamentals. *Phys. Rep.*, 106:121–167, 1984.

[63] S. M. Gruenbaum and R. F. Loring. Interference and Quantization in Semiclassical Response Functions. *J. Chem. Phys.*, 128:124106, 2008.

[64] S. M. Gruenbaum and R. F. Loring. Semiclassical Mean-Trajectory Approximation for Nonlinear Spectroscopic Response Functions. *J. Chem. Phys.*, 129:124510, 2008.

[65] S. M. Gruenbaum and R. F. Loring. Semiclassical Nonlinear Response Functions for Coupled Anharmonic Vibrations. *J. Chem. Phys.*, 131:204504, 2009.

[66] S. M. Gruenbaum and R. F. Loring. Semiclassical Quantization in Liouville Space for Vibrational Dynamics. *J. Phys. Chem. B*, 115:5148–5156, 2011.

[67] M. F. Herman and E. Kluk. A Semiclassical Justification for the use of Non-Spreading Wavepackets in Dynamics Calculations. *Chem. Phys.*, 91:27–34, 1984.

[68] M. F. Herman and D. F. Coker. Classical Mechanics and the Spreading of Localized Wave Packets in Condensed Phase Molecular Systems. *J. Chem. Phys.*, 111:1801–1808, 1999.

[69] W. H. Miller. An Alternative Derivation of the Herman-Kluk (Coherent State) Semiclassical Initial Value Representation of the Time-Evolution Operator. *Mol. Phys.*, 100:397–400, 2002.

[70] S. A. Deshpande and G. S. Ezra. On the Derivation of the Herman-Kluk Propagator. *J. Phys. A*, 39:5067–5078, 2006.

[71] T. K. Yee and T. K. Gustafson. Diagrammatic Analysis of the Density Operator for Nonlinear Optical Calculations: Pulsed and CW Responses. *Phys. Rev. A*, 18:1597–1617, 1978.

[72] P. Hamm, M. Lim, and R. M. Hochstrasser. Non-Markovian Dynamics of the Vibrations of Ions in Water from Femtosecond Infrared Three-Pulse Photon Echoes. *Phys. Rev. Lett.*, 81:5326–5329, 1998.

[73] M. Khalil, N. Demirdoven, and A. Tokmakoff. Coherent 2D IR Spectroscopy: Molecular Structure and Dynamics in Solution. *J. Phys. Chem. A*, 107:5258–5279, 2003.

[74] Y. Tanimura and S. Mukamel. Description of Nonlinear Optical Response using Phase-Space Wave Packets. *J. Phys. Chem.*, 97:12596–12601, 1993.

[75] W. G. Noid, G. S. Ezra, and R. F. Loring. Vibrational Echoes: Dephasing, Rephasing, and the Stability of Classical Trajectories. *J. Phys. Chem. B*, 108:6536–6543, 2004.

[76] R. B. Williams and R. F. Loring. Vibrational Dephasing of an Anharmonic Solute Strongly Coupled to Solvent. *J. Chem. Phys.*, 110:10899–10906, 1999.

[77] R. Zwanzig. Nonlinear Generalized Langevin Equations. *J. Stat. Phys.*, 9:215–220, 1973.

[78] D. W. Oxtoby. Vibrational Relaxation in Liquids. *Annu. Rev. Phys. Chem.*, 32:77–101, 1981.

[79] A. O. Caldeira and A. J. Leggett. Quantum Tunneling in a Dissipative System. *Ann. Phys.*, 149:374–456, 1983.

[80] Y. Tanimura and P. G. Wolynes. Quantum and Classical Fokker-Planck Equations for a Gaussian-Markovian Noise Bath. *Phys. Rev. A*, 43:4131–4142, 1991.

[81] A. Ishizaki and Y. Tanimura. Quantum Dynamics of System Strongly Coupled to Low-Temperature Colored Noise Bath: Reduced Hierarchy Equations Approach. *J. Phys. Soc. Jpn.*, 74:3131–3134, 2005.

[82] D. W. Oxtoby. Dephasing of Molecular Vibrations in Liquids. *Adv. Chem. Phys.*, 40:1–48, 1979.

[83] K. S. Schweizer and D. Chandler. Vibrational Dephasing and Frequency Shifts of Polyatomic Molecules in Solution. *J. Chem. Phys.*, 76:2296–2314, 1982.

[84] W. Zhuang, T. Hayashi, and S. Mukamel. Coherent Multidimensional Vibrational Spectroscopy of Biomolecules: Concepts, Simulations, and Challenges. *Chem. Rev.*, 48:3750–3781, 2009.

[85] J. Jeon and M. Cho. Direct Quantum Mechanical/Molecular Mechanical Simulations of Two-Dimensional Vibrational Responses: N-Methylacetamide in Water. *New. J. Phys.*, 12:065001, 2010.

[86] M. D. Fayer, editor. *Ultrafast Infrared Vibrational Spectroscopy*. CRC Press, Boca Raton, 2013.

[87] J. J. Loparo S. T. Roberts and A. Tokmakoff. Characterization of Spectral Diffusion from Two-Dimensional Line Shapes. *J. Chem. Phys.*, 125:084502, 2006.

[88] F. Grossmann. Semiclassical Coherent-State Path Integrals for Scattering. *Phys. Rev. A*, 57:3256–3261, 1998.

[89] W. H. Miller. On the Relation Between the Semiclassical Initial Value Representation and an Exact Quantum Expansion in Time-Dependent Coherent States. *J. Phys. Chem. B*, 106:8132–8135, 2002.

[90] R. Saha and M. Ovchinnikov. Herman-Kluk Semiclassical Dynamics in Action-Angle Representation: New Approaches to Mapping Quantum Degrees of Freedom. *J. Chem. Phys.*, 124:204112, 2006.

[91] K. G. Kay. The Herman-Kluk Approximation: Derivation and Semiclassical Corrections. *Chem. Phys.*, 322:3–12, 2006.

[92] R. G. Littlejohn. The Semiclassical Evolution of Wave Packets. *Phys. Rep.*, 138:193–291, 1986.

[93] M. V. Berry. Semi-Classical Mechanics in Phase Space: A Study of Wigner's Function. *Phil. Trans. Roy. Soc. Lond.*, 287:237–271, 1977.

[94] P. A. M. Dirac. On the Theory of Quantum Mechanics. *Proc. R. Soc. Lond. A*, 110:661–677, 1926.

[95] C. Jaffe and P. Brumer. Classical-Quantum Correspondence in the Distribution Dynamics of Integrable Systems. *J. Chem. Phys.*, 82:2330–2340, 1985.